DUCTILE FRACTURE OF METALLIC MATERIALS THROUGH MICROMECHANICS BASED COHESIVE ZONE ELEMENTS

A THESIS SUBMITTED TO
THE GRADUATE SCHOOL OF NATURAL AND APPLIED SCIENCES
OF
MIDDLE EAST TECHNICAL UNIVERSITY

BY

İZZET TARIK TANDOĞAN

IN PARTIAL FULFILLMENT OF THE REQUIREMENTS
FOR
THE DEGREE OF MASTER OF SCIENCE
IN
AEROSPACE ENGINEERING

SEPTEMBER 2020

Approval of the thesis:

DUCTILE FRACTURE OF METALLIC MATERIALS THROUGH MICROMECHANICS BASED COHESIVE ZONE ELEMENTS

submitted by **İZZET TARIK TANDOĞAN** in partial fulfillment of the requirements for the degree of **Master of Science in Aerospace Engineering Department, Middle East Technical University** by,

Prof. Dr. Halil Kalıpçılar
Dean, Graduate School of **Natural and Applied Sciences** ____________

Prof. Dr. İsmail H. Tuncer
Head of Department, **Aerospace Engineering** ____________

Assoc. Prof. Dr. Tuncay Yalçınkaya
Supervisor, **Aerospace Engineering, METU** ____________

Examining Committee Members:

Prof. Dr. Demirkan Çöker
Aerospace Engineering, METU ____________

Assoc. Prof. Dr. Tuncay Yalçınkaya
Aerospace Engineering, METU ____________

Assoc. Prof. Dr. Ercan Gürses
Aerospace Engineering, METU ____________

Assoc. Prof. Dr. Cihan Tekoğlu
Mechanical Engineering, TOBB UET ____________

Assist. Prof. Dr. Ali Javili
Mechanical Engineering, Bilkent University ____________

Date: 16.09.2020:

I hereby declare that all information in this document has been obtained and presented in accordance with academic rules and ethical conduct. I also declare that, as required by these rules and conduct, I have fully cited and referenced all material and results that are not original to this work.

Name, Surname: İzzet Tarık Tandoğan

Signature :

ABSTRACT

DUCTILE FRACTURE OF METALLIC MATERIALS THROUGH MICROMECHANICS BASED COHESIVE ZONE ELEMENTS

Tandoğan, İzzet Tarık
M.S., Department of Aerospace Engineering
Supervisor: Assoc. Prof. Dr. Tuncay Yalçınkaya

September 2020, 137 pages

Gaining popularity after its coupling with the finite element method, cohesive zone modelling has been used extensively to model fracture, especially in delamination problems. Its constitutive relations, i.e. traction-separation laws, are mostly derived phenomenologically without considering the physical mechanisms of crack initiation and propagation. The approach could also be used for ductile fracture where the micromechanics of the phenomenon is explained by nucleation, growth and coalescence of pores. In this context, the objective of the current thesis is to develop and implement a cohesive zone modelling framework for ductile fracture in metallic materials. In order to accomplish this, a micromechanics based traction-separation relation which considers the growth of a physical pore is developed based on the previous works in [1–3]. Tractions are directly represented as a function of pore fraction, and its evolution is driven by separations. The model is implemented as an intrinsic cohesive zone model in a two-dimensional (2D) setting. Implementation steps and methodology including the finite element framework are presented in detail for mode-I, mode-II and mixed-mode fracture cases. The derivation of the mixed-mode case leads to a yield function representation of tractions and separations, instead of an explicit expression. Hence, an incremental implicit elasto-plastic numerical integration scheme is developed to solve mixed-mode system of equations. Implementation is validated by running tests with a single cohesive element. In addition, the framework is implemented as a user element subroutine in Abaqus (UEL) and the numerical simulations are conducted with compact tension (CT) and single edge notch (SEN) specimens to show the capability of the model and the influence of the micromechanical parameters such as pore size and shape on the ductile crack initiation and propagation. The work is concluded by presenting an outlook for the usage of the model in micron sized specimens where the developed micromechanical model presents a great potential in explaining certain deformation mechanisms in high strength aerospace alloys.

Keywords: Cohesive Zone Model, Ductile Fracture, Porous Plasticity

ÖZ

MİKROMEKANİK TEMELLİ KOHEZİF BÖLGE ELEMANLARI YOLUYLA METALİK MALZEMELERDE SÜNEK KIRILMA

Tandoğan, İzzet Tarık
Yüksek Lisans, Havacılık ve Uzay Mühendisliği Bölümü
Tez Yöneticisi: Doç. Dr. Tuncay Yalçınkaya

Eylül 2020 , 137 sayfa

Sonlu elemanlar yöntemi ile beraber popülerlik kazanan kohezif bölge modellemesi, çatlak modellemesi, özellikle katman ayrılması, için yaygın olarak kullanılmıştır. Kohezif bölge modellerinin bünye denklemi, yani çekme-yer değiştirme eğrileri, çoğunlukla görüngüsel olarak çatlakların oluşması ve ilerlemesindeki fiziksel mekanizmalar dahil edilmeden türetilmektedir. Bu yaklaşım, mikromekanik olayların çekirdeklenme, büyüme ve porların birleşmesi ile açıklandığı sünek kırılma için de kullanılabilir. Bunun için fiziksel bir porun büyümesini hesaba katan mikromekanik temelli bir çekme-yer değiştirme eğrisi önceki çalışmalara dayanılarak geliştirildi [1–3]. Çekme direk olarak por oranı cinsinden elde edildi ve por oranının değişimi yer değiştirmeye bağlandı. Model iki boyutta içsel bir kohezif bölge modeli olarak uygulandı. Sonlu elemanlar yönteminin uygulama aşamaları ve metodolojisi, mod-I, mod-II ve karışık mod çatlakları için ayrıntılı olarak sunuldu. Karışık mod için türetme aşamaları sonucunda açık bir gösterim yerine çekme ve yer değiştirmeleri içeren bir akma fonksiyonu elde edildi. Dolayısıyla, karışık mod doğrusal olmayan denklem sistemini çözmek için örtük elastik-plastik bir numerik integrasyon düzeni kullanıldı. Uygulama, tek bir kohezif eleman ile testler yapılarak doğrulandı. Ayrıca model Abaqus içinde kullanıcı eleman altprogramı (UEL) olarak uygulandı ve sünek çatlak başlaması ve ilerlemesi üzerinde modelin kapasitesini ve por boyutu ve şekli gibi mikromekanik parametrelerin etkisini göstermek için nümerik CT ve SEN modelleri ile simülasyonlar yapıldı. Çalışma, geliştirilen mikromekanik modelin yüksek mukavemetli havacılık alaşımlarında belirli deformasyon mekanizmalarını açıklamada büyük bir potansiyel sunduğu gösterilerek ve modelin mikron boyutlu numunelerde kullanımına ilişkin bir bakış açısı sunularak sonuçlandırılmıştır.

Anahtar Kelimeler: Kohezif Bölge Modeli, Sünek Çatlama, Porlu Plastisite

To my elementary school teacher Mr. Kadri Baki Has who inspired me to love science.

ACKNOWLEDGMENTS

First of all, I would like to thank my supervisor, Assoc. Prof. Dr. Tuncay Yalçınkaya. Undoubtedly, I would not be the person I am now if it not for his support, guidance, advice, and faith in me over the last three years. Moreover, I thank Assoc. Prof. Dr. İzzet Özdemir for making his work available to me.

Also, I am grateful to Prof. Dr. Alan Cocks from University of Oxford for his mentorship and help, which made this work possible.

I want to send regards to friends Gökhan Genç, İbrahim Mert Yaşar, Sadık Ata Yalçınkaya, Turgay Kaya, Oğuzhan Aydın and Çiğdem Ekiz. I would like to thank Can Erdoğan for valuable discussions and input. Special thanks go to my flatmates for their support and patience.

Warmest thanks to Elif Bekoğlu for being there in my hard times. I hope I can do the same for you.

I want to give my genuine thanks and respect to my father Muammer and mother Sevim because they deserve it for being the best parents I can imagine.

I would like to acknowledge the support by the Scientific and Technological Research Council of Turkey (TÜBİTAK) under the 3501 Programme (Grant No. 117M106). The scientific advances presented in the thesis have been achieved under the regarding project investigated by Assoc. Prof. Tuncay Yalçınkaya.

TABLE OF CONTENTS

LIST OF TABLES

TABLES

LIST OF FIGURES

FIGURES

LIST OF ALGORITHMS

ALGORITHMS

LIST OF ABBREVIATIONS

ABBREVIATIONS

2D	2 Dimensional
CZM	Cohesive Zone Model
MBCZM	Micromechanics Based Cohesive Zone Model
PPR	Park-Paulinho-Rosler
TSL	Traction-separation law
CT	Compact Tension
SEN	Single Edge Notch
RVE	Representative Volume Element
X-FEM	Extended Finite Element Method
GFEM	Generalized Finite Element Method
CDM	Continuum Damage Model
GTN	Gurson-Tvergaard-Needleman
DNS	Direct Numerical Simulation
CDT	Continuous-Discontinuous Transition
PF	Phase-Field
TLS	Thick Level-Set Method
PPR	Park-Paulinho-Rosler
PFZ	Precipitate Free Zone
SGCP	Strain Gradient Crystal Plasticity

SYMBOLS

$T_{n/t}$	Normal/tangential traction
$T_{n/t,max}$	Normal/tangential maximum traction
$\delta_{n/t}$	Normal/tangential separation

$\delta_{n/t,cr}$	Normal/tangential separation at maximum traction
$\delta_{n/t,max}$	Maximum achieved normal/tangential separation
$\dot{\varepsilon}_e$	Effective strain rate
σ_y	Yield stress
h/h_0	MBCZM RVE height/initial height
a	MBCZM RVE pore radius
l	MBCZM RVE radius
f/f_0	MBCZM RVE pore area fraction/initial pore area fraction
$E_{n/t}$	Normal/tangential elastic slope
$\delta^e_{n/t}$	Normal/tangential elastic separation
$\delta^p_{n/t}$	Normal/tangential plastic separation
μ	Plastic multiplier
α	Proportionality ratio
$W_{n/t/frac}$	Normal/tangential/total fracture energy
E	Young's Modulus
ν	Poisson's ratio
Δa	Crack extension length

CHAPTER 1

INTRODUCTION

Humans discovered how to use metals 9000 years ago, and it revolutionized our civilization. From there, the goal was to make better, stronger, and tougher materials. With the idea of flying and the advent of aircraft, lighter was added to the equation. Then came computers, electronics, microchips, and with them the need for smaller. Today, humanity have come so far that the ideal material would be strong, tough, light, small, resistant to heat, corrosion, radiation, but most importantly, 'cheap'. Unfortunately, such material does not exist, but there is one material type that can have most of these properties. They are used everywhere in the modern world, in buildings, tools, vehicles including ground, sea, air and space crafts, healthcare, industry, and many more, and they are known as metallic alloys. Depending on the purpose of their use, they undergo various production and manufacturing phases. Some of them are lost in the process, damaged beyond repair or fractured. Those that survive may be used in critical places, where failure of the part would be catastrophic. Therefore, predicting the fracture of metallic materials is of high interest.

Fracture in metallic materials is mainly categorized into two: ductile and brittle fracture. Brittle fracture is more catastrophic as it does not give any warning beforehand. There is little to no plastic deformation, and crack can propagate at velocities beyond the speed of sound [5]. Whereas, in ductile fracture, there is excessive plastic deformation before failure. Our interest is on ductile fracture. Essentially, plastic deformation is used for the shaping of metals. From a manufacturer's point of view, understanding the state of ductile fracture present in the metal can greatly improve efficiency. Therefore, significant effort has been made to model ductile fracture in metals over the past several decades. It was known that the underlying physical mechanism for the initiation and propagation of ductile cracks in metallic materials is the nucleation, growth and coalescence of micro-voids [6–10]. Voids nucleate at inclusions and second phase particles due to particle-matrix interface decohesion or particle cracking. Then, voids grow due to plastic deformation and coalesce by necking of material between closely spaced voids or by localization of plasticity between separated voids, a mechanism that was reviewed rigorously [11–15]. This microscopic physical mechanism eventually can be observed as macroscopic cracks causing failure of the material. It is desired to model this phenomenon numerically. There are various computational approaches in the literature to model ductile fracture, each having merits and demerits. Some of them are covered in the following paragraphs [16].

Discontinuous approaches, where cracks are physically modelled, i.e. there is an actual jump in the displacement field across crack faces. For example, 'element erosion' is such an approach. In a finite element framework, discontinuity is introduced simply by removing elements from the formulation which have exceeded their load-carrying capacity. This removal is usually spread to several increments in order to have a better convergence performance [17, 18]. An application in dual-phase steels was made by modelling ductile fracture of ferrite [19]. Despite the ease of implementation and low computational cost, this approach has problems such as mesh size and element shape dependence, and mass loss [20]. Another example of discontinuous approaches is the 'enriched finite element' methods. Most popular ones are Extended Finite Element Method (X-FEM) [21], and Generalized Finite Element Method (GFEM) [22]. In these methods, cracks can initiate and propagate at any location independent of the mesh. Using enrichment functions, strong discontinuities such as cracks or holes [23], or weak discontinuities like matrix/inclusion interfaces can be modelled [24]. However, as evidenced by the difference in the number of works in the literature, these methods are more suitable for brittle fracture. Because the significant plastic deformation of ductile fracture may impose a requirement for the modification of mesh, which is against these methods' main point. Another approach similar to element erosion is mesh modification. Instead of removing elements, nodes can be duplicated at the locations where a fracture criterion is met. Mediavilla et. al. [20] used a nonlocal integral damage indicator, and Bouchard et. al. [25] used a stress-based criterion. Traction between the duplicated nodes can be released progressively over several increments. Also, mesh refinement or mesh adaptation can be used to improve the accuracy of simulations [26, 27]. A setback of these methods is the difficulty of implementation, especially for 3D, and if different types and orders of elements are involved. Finally, there are cohesive zone models (CZMs). Previous approaches lack an accurate means to control the energy dissipation rate. CZMs achieve this naturally by defining an initially zero thickness interface element at crack locations. These elements can open up similar to a crack obeying a constitutive relation called traction-separation law. This approach is discussed in more detail later on.

There are continuous approaches, where cracks or pores are not represented explicitly. Instead, they are included in phenomenological relations, and they influence the damage and degradation of material in macro scale. The most widely used ones for ductile fracture modeling are Continuum Damage Models (CDMs). The Lemaitre model uses an effective stress definition with a damage variable D [28] to include the effect of pores [29]. For the evolution of the damage variable, usually, empirical laws are used. Differently, the most popular Gurson-Tvergaard-Needleman (GTN) model [30, 31] and the Rousselier model [32] took a micromechanical approach to the problem. As a result, a porosity variable appears explicitly in the yield function, and the effect of the size and shape of pores can be induced. However, similar to the Lemaitre model, they rely on phenomenological corrections or empirical laws to provide accurate results in real-life applications. It was shown that as damage progresses, it localizes to a single layer of elements, causing mesh dependency [33]. Several methods in the literature address this problem. Namely, non-local integral formulations, non-local implicit gradient formulations, strain gradient plasticity formulations, and thick level-set method. Another continuous approach is multiscale methods. In theory, it is possible to model a part's whole microstructure to solve for the macroscopic response. This is called a direct numerical simulation, DNS. However, it is not possible with today's computational power. Because of that, multiscale methods aim to obtain a macro-scale solution from micro-scale calculations; in other words, homogenization. Gurson's analytical approach to a spherical pore is analytical homogenization [30]. These are limited by the complexity of the geometry and boundary conditions. There is also computational homogenization, where micro and macro-scale are solved simultaneously. Representative volume elements (RVEs) in the micro-scale are used to obtain material laws on the macro-scale.

Another approach is the continuous-discontinuous transition (CDT). In most CDMs, it is assumed that damage variable is small, a D above 0.5 is considered unrealistic [29]. Similarly, there is a correction in GTN to boost pore growth when coalescence becomes dominant [31]. Hence, CDMs should model the softening of the material up to a certain point, after which a fracture mechanism is necessary. The objective here is to relieve the damaged regions from the load. At first sight, the obvious strategy is to combine continuous approaches like CDMs or multiscale methods with discontinuous approaches like element erosion or enriched finite element methods. There are many examples of this in the literature [34–41]. A more novel and recent approach is Phase-Field (PF) methods, where a damage model, regularization technique and CDT model exist in one theory. It can be seen as a optimization problem to minimize the potential energy [42, 43]. Similar to before, there is a bulk variable from 0 to 1 describing the damage. However, instead of sharp interfaces, cracks are weakly represented by this continuous damage variable. The potential for brittle fracture includes elastic-plastic energy and fracture energy. Due to ductile fracture complexities, an extension is done by adding plastic potential energy to brittle fracture potential. This extension requires additional considerations, and it is not straightforward. Hence, most of the literature using PF is on brittle fracture. Some examples are [44–47]. Another novel approach is the thick level-set (TLS) method. Like PF, instead of a sharp interface, there is a transition zone between failed and undamaged material. This zone has a given length, l_c, and is imposed using an level-set (LS) function [48]. Unlike PF, TLS is coupled to a CDM, so there is no PF potential function defined.

That was a short review of the methods used to model ductile fracture. From now on, focus will be on cohesive zone modelling. It has been more than fifty years since the first appearance of the cohesive zone concept by [49] and [50], which was later described by [51]. After the pioneering work of [52], over the years, it has been proven to be powerful in the modelling of fragmentation of materials when coupled with the finite element method. With this approach, the fracture mechanism is represented with interface elements or cohesive elements placed in-between the bulk elements at potential separation locations. These cohesive elements initially

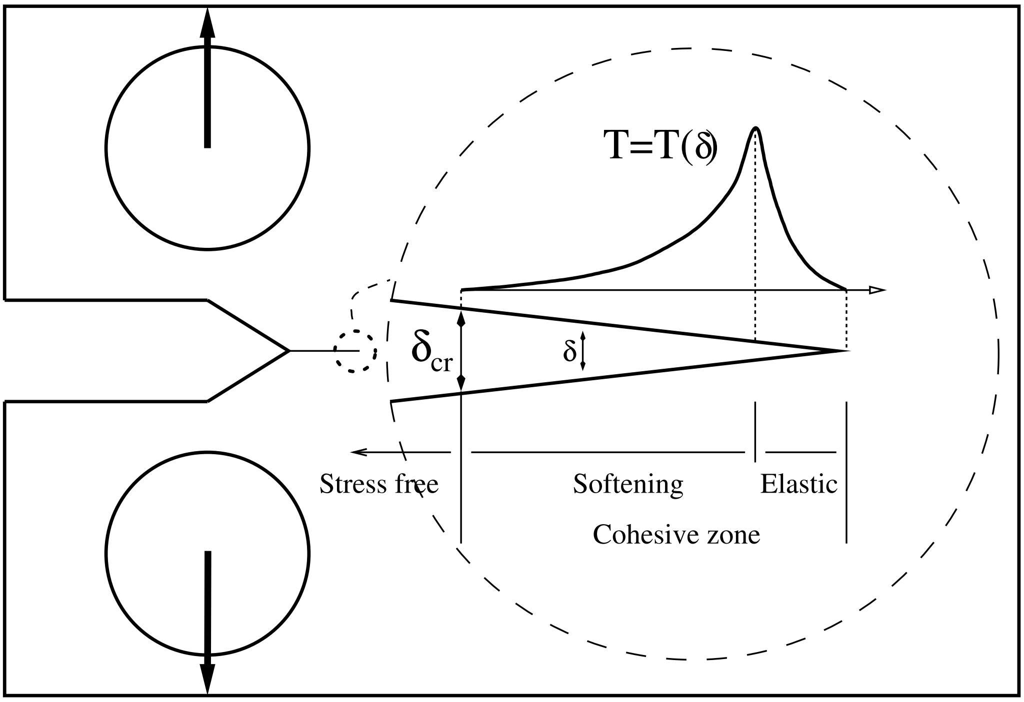

Figure 1.1: Cohesive zone concept at the crack tip. Traction of crack surfaces, T, is a function of crack face separation, δ.

have zero thickness. They can open up similar to a crack, and a traction-separation law (TSL) governs their behavior while the bulk elements remain undamaged. In a TSL, traction is a function of the displacement jump or separation. The concept of a cohesive zone model is represented in Figure 1.1. It is assumed that at the crack tip, there is a process zone or cohesive zone with a given length. In this zone, at the front of the crack tip material is undamaged. Towards the back of the crack, as crack opening increases, the material becomes more and more damaged. After a critical separation, it becomes fully broken. At a point in the material where crack forms and opposite faces separate, the material's resistance to separation decreases with increasing separation. This is based on the fact that the cohesive force between atoms and molecules first increase, then decrease as they get further from stable position, see Figure 1.2. The energy spent to separate the molecules is the energy required to create a new crack surface. This phenomenon of separating molecules and creating a fracture surface is phenomenologically represented by a Traction-Separation Law, TSL, in cohesive zone modelling. There is no unique form of the traction-separation law, and countless of them have been suggested in the literature. Based on atomic

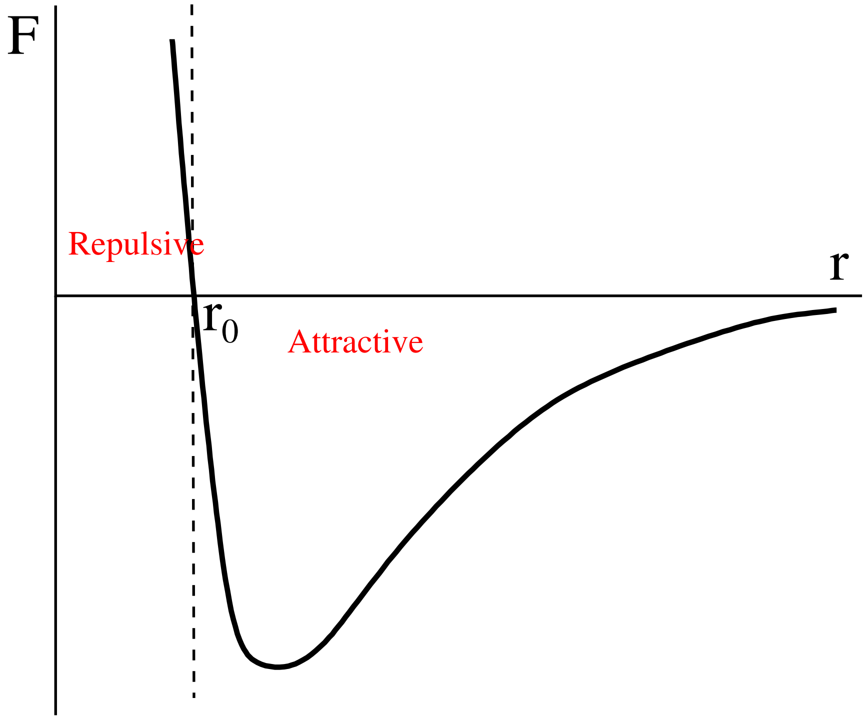

Figure 1.2: Repulsive and attractive forces with respect to distance between atoms.

binding energy calculations by Rose et al. [53,54], Xu and Needleman [55] suggested an exponential form for normal traction versus normal separation. Bilinear being the simplest one, exponential, polynomial, and trilinear forms exist; see Figure 1.3. For ductile fracture, often exponential (Fig. 1.3(e)) and trilinear (Fig. 1.3(b)) forms are used. The maximum traction, the area under the traction-separation curve, or fracture energy, and the critical separation where the traction becomes zero are the main characteristics of such laws. They are mainly divided into two forms, initially elastic, or intrinsic, and initially rigid, or extrinsic. In the former, traction starts from zero, increases to a non-zero value, then decreases, while in the latter, traction starts from a finite value and then decreases (Fig. 1.3(f)). There are differences in their implementation due to their nature, which will be discussed next.

Cohesive elements are zero-thickness surface elements that respond to loading according to a TSL. These elements are inserted between other bulk elements in a finite element mesh, where cracks are expected to form. For the case of intrinsic TSLs, implementation is straightforward. Because cohesive elements can be inserted into the potential crack paths before the analysis begins. However, this convenience comes

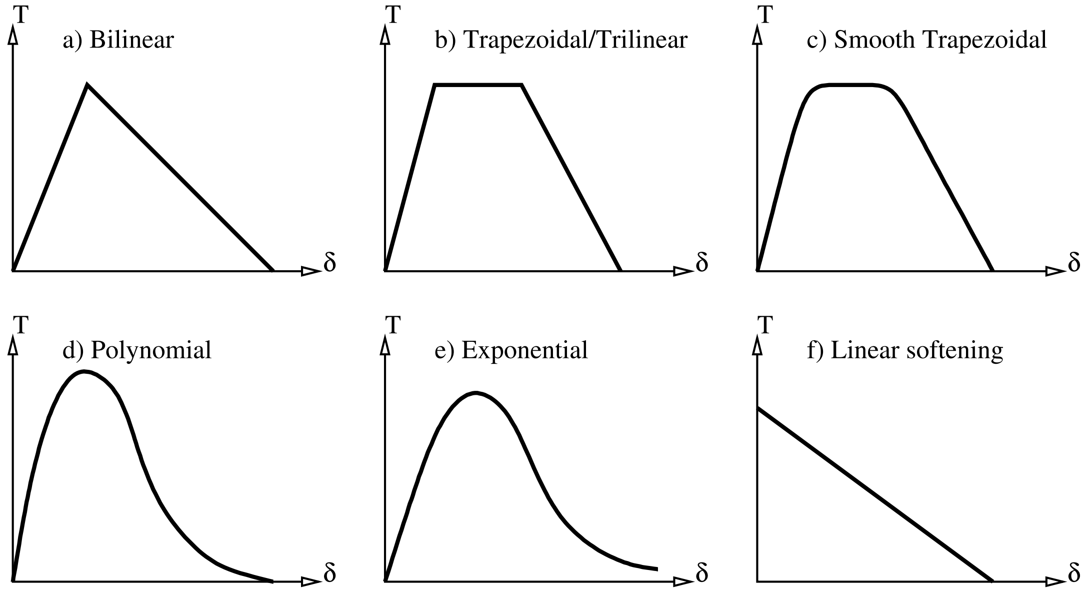

Figure 1.3: Some common types of traction-separation laws. Bilinear (a), trapezoidal (b), smooth trapezoidal (c), polynomial (d), exponential (e), linear softening (f).

together with a problem, namely, artificial compliance. Remember that in intrinsic TSLs, there is an initial region where traction increases from zero to maximum. This region has an elastic slope. This fact reduces the stiffness of the material and affects the macroscopic response [56]. Therefore, it is advised that the elastic slope of the TSL should be reasonably big. If it is too big, convergence problems can arise. A way around is taking the slope as infinite and allowing separation of cohesive elements only when maximum traction is reached. This can be done by using Lagrange multipliers [57], or in Abaqus software, multi-point-constraint (MPC) subroutine can be used to tie nodes [58]. However, the implementation of it becomes cumbersome when 3D and mixed-mode are involved. A built-in solution to artificial compliance is extrinsic TSLs since they do not have an elastic slope (Fig. 1.3(f)). In extrinsic cohesive zone models, cohesive elements are inserted during the analysis when a fracture criterion is met. This approach is challenging to implement as it requires mesh manipulation during analysis. Nodes need to be duplicated to insert a cohesive element. Another advantage of extrinsic CZM is that it is not necessary to know crack paths a priori [59]. Whereas, if this is the case for intrinsic CZM, cohesive elements should be inserted everywhere, but that makes the artificial compliance problem worse and increases computational cost. Both approaches suffer from mesh dependency. Due to the fact that cracks can only form on cohesive elements, the crack path is hugely dependant on mesh size. Hence, CZMs are very suited to problems where the crack path is known. For example, interface debonding problems, i.e. matrix-inclusion debonding or delamination in composites [60–63]. Still, recent developments showed that mesh dependency could be solved by coupling CZM to advanced finite element methods. For example, [64] modeled 2D ductile fracture using CZM with X-FEM. There is not a single correct form for the TSLs. This is an advantage of cohesive zone modelling since it allowed researchers to introduce different physical mechanisms into cohesive zone modelling. For example, a decay factor is introduced to diminish maximum traction under constant amplitude displacement cycling to model fatigue crack growth [65]. Busto et al. [66] modelled fatigue by using an irreversible TSL with a damage parameter and modelled hydrogen embrittlement by including hydrogen concentration coupled with a diffusion mechanism to penalize traction. Zhou et al. [67] modelled dynamic crack propagation in brittle materials by making the critical separation, where tractions become zero, a function of crack tip velocity. Valoroso et al. [68] modelled rate-dependency by amplifying the critical energy release rate with a function. Banerjee and Manivasagam [69] proposed an effective triaxiality parameter for mode-I to model ductile fracture at different stress states. Chanda and Ru [70] related maximum traction of TSL to maximum fraction stress obtained from Johnson and Cook model at a range of temperatures to model temperature dependant fracture of pipeline steels. These examples show how the effect of some physical mechanisms can be incorporated relatively easily. Of course, if desired, they can be directly coupled to have a more physically accurate model [66, 71].

Cohesive traction separation laws may be derived by following theoretical, experimental, or computational approaches. Here, some of the early theoretical works and improvements will be discussed. Needleman [72] introduced a debonding potential, ϕ, which was used to model inclusion debonding. This potential is a function of normal and tangential separations, $\phi(\delta_n, \delta_t, \delta_b)$. Tractions are obtained simply by taking the derivative of ϕ with respect to δ_n, δ_t and δ_b. The motivation in choosing the form of potential is to obtain a specific type of response in normal traction, as stated by the author. The potential results in cubic-polynomial normal traction and linear tangential traction. Since tangential traction can increase endlessly, the model is limited to small shear separations. Later on, the same author [73] proposed a potential energy that agrees with the universal binding energy [53]. Normal-tangential tractions are of exponential-periodic form. However, the model does not include fracture parameters for mode-II and cannot describe mixed-mode response. Beltz and Rice [74, 75] generalized [73] and introduced a length scale parameter to make T_n satisfy a more logical boundary condition under mixed-mode loading. However, this potential cannot be used for mode-II failure since tangential traction is periodic. A one-dimensional effective displacement-based model was introduced by Tvergaard [76]. Effective traction as a function of effective displacement is given as, $\overline{T}(\overline{\Delta}) = \frac{27}{4}\sigma_{max}\overline{\Delta}(1 - 2\overline{\Delta} + \overline{\Delta}^2)$, which is same form as the normal traction of [72], where σ_{max} is maximum traction. Effective displacement is $\overline{\Delta} = \sqrt{(\Delta_n/\delta_n)^2 + (\Delta_t/\delta_t)^2}$, and tractions are given as $T_n = \frac{\overline{T}(\overline{\Delta})}{\overline{\Delta}}\frac{\Delta_n}{\delta_n}$, $T_t = \frac{\overline{T}(\overline{\Delta})}{\overline{\Delta}}\alpha_e\frac{\Delta_t}{\delta_t}$, where α_e is associated with mode mixity, $\overline{\Delta}_{n/t}$ is normal/tangential separation, $\delta_{n/t}$ is normal/tangential failure separation. This approach allows us to model mixed-mode fracture problems with a mode mixity parameter using a 1D framework for tractions. Later on, Tvergaard and Hutchinson [77] used a 1D potential leading to $\alpha_e = \delta_n/\delta_t$. However, different fracture energies of mode-I and mode-II are not considered. Effective displacement methods have some common problems. Stiffness can be positive under softening conditions, fracture energies for mode-I and mode-II are the same, and negative normal separation has the same effect as positive one [78]. [73] was improved by Xu and Needleman [55]. Both normal and tangential tractions are of exponential form intending to model pure mode-II failure. Also, the ratio of mode-I and mode-II fracture energies can be specified with a parameter, q. This model was successful and has been used extensively to the date. However, it has some defects, as pointed out by Park and Paulino [78], and it was improved by Bosch et al. [79]. Camacho and Ortiz [59] introduced the extrinsic cohesive zone models, which do not have an initial elastic region in TSL. It was used it to model dynamic fragmentation [80] and microbranching [81]. Addressing the problems in previous CZMs, Park et al. [82] proposed the potential based Park-Paulinho-Rosler, PPR, cohesive zone model. It can model mixed-mode fracture for a range of materials and is very flexible. Both tractions have polynomial form, mode-I and mode-II fraction energies, and maximum tractions can be specified separately. Also, the size of the elastic regime in TSL and the shape of the softening region can be selected.

The theoretical approaches discussed above are phenomenological. Usually, a potential is assumed to obtain the desired form of the TSL, which can be motivated by physical reasons [55]. There is not a consensus on the form of TSL for ductile fracture. In ductile fracture, elasticity, plasticity, and damage are included together, and the form of TSL cannot be determined experimentally. An experimental approach is to assume a form of the TSL, then fit the maximum traction and cohesive energy to best represent the macroscopic response of experimental specimens [83–85]. However, Scheider [86] showed that the shape of TSL has a significant effect on the results of crack propagation simulations of ductile materials. Li and Chandra [87] suggested that forms of CZMs are results of different micromechanisms taking part in energy dissipation during fracture. A widely used and physically motivated numerical approach to obtain traction-separation relations for ductile materials is using the well-known GTN model. GTN model, a continuum damage model, based on nucleation, growth and coalescence of pores, is used to obtain the macroscopic response, which can then be used to fit cohesive parameters of a selected form. Tvergaard and Hutchinson [88] obtained parameters of TSL by modelling a 'void-sheet' with multiple interacting voids ahead of the crack tip by using the Gurson model. Schieder [89] extracted the TSL from the mesoscopic response of a representative volume element with a heterogeneous microstructure using Gurson's model. Andersen et al. (2019) [90] analyzed ductile plate tearing with GTN to obtained a micromechanics based cohesive zone model with bilinear and trilinear TSLs. Andersen et al. (2020) [91] showed that heterogeneous microstructure strongly influences the cohesive energy of TSL in the tearing of ductile plates where GTN is used as a material model.

Cohesive zone modelling has been one of the most popular approaches for modelling the fracture process, yet its constitutive TSLs are mostly based on phenomenological relations, as discussed before. Usually, in ductile fracture, the physics at the fracture process zone is incorporated into cohesive parameters of a TSL using homogenization schemes. In this thesis, a more direct approach is followed. The idea here is to bridge the information obtained from the physical fracture mechanism due to void growth to a traction-separation law to obtain a physically motivated relation to be implemented in ductile crack propagation simulations. The derivation and the numerical analysis of a traction-separation law based on the growth of pores are discussed. First, an array of cylindrical representative volume elements with initial cylindrical pores is considered. Under normal and shear displacements, traction separation relations are obtained by applying the upper bound theorem for mode-I and mode-II, respectively. As a result, micromechanical parameters appear in the traction separation-law directly, such as pore fraction and pore height. The evolution of these parameters is governed by normal and tangential separations, which leads to an implicit mixed-mode capability. For mixed-mode, a yield function consisting of normal and tangential tractions and pore variables is obtained. Hence, an implicit elastoplastic numerical integration scheme is employed to solve the mixed-mode system of equations. The performance of the model and the effect of micromechanical parameters are investigated through numerical simulations.

The thesis is organized as follows. First, in Chapter 2, derivations of the models and equations are detailed for micromechanics based cohesive zone model (MBCZM) for mode-I, mode-II and mixed-mode loading. Then, in Chapter 3 numerical implementation of the model is presented. In Chapter 4, numerical simulations are conducted using MBCZM. Finally, in Chapter 6, the conclusions and the future remarks are given.

CHAPTER 2

DERIVATION OF PHYSICS BASED COHESIVE ZONE MODEL

In this chapter, the steps for obtaining the traction-separation equations are presented in detail. A cylindrical RVE with a cylindrical pore is subjected to tractions where the material is rigid-perfectly plastic. The upper-bound theorem is applied to determine tractions. Obtained traction-separation laws are based on micromechanical parameters such as initial pore fraction, initial pore height and pore spacing. The evolution of the micromechanical parameters under given boundary conditions determine the change in tractions. Derivations are done first for pure mode-I, II, then for mixed-mode. The derivation presented in the following are based on the initial studies in [1–3]. Note that the presented cylindrical RVE is a non-space filling type of RVE, which has been used in the literature together with the space filling RVEs. Please check the recent study in Firooz et al. [92] to see an overview on the issue. The advantage of this type of RVE is that maximum void volume fraction, 1, can be reached which is also observed in a real cutout of a material. Also, it is suitable to predict isotropic material behavior because it can capture isotropy intrinsically.

2.1 Traction-separation relation for Mode-I loading

Imagine an array of cylindrical volumes in a plane, each with a cylindrical hole in the middle. Each cylinder has diameter $2l$, height h, and the hole represents an idealized pore with a radius of a (Fig. 2.1). In Fig. 2.2, a close-up to the crack tip under mode-I loading is shown, and crack opening process is represented by the cylindrical RVEs. Take one cylinder as representative volume element subject to following boundary conditions visualized in Fig. 2.2,

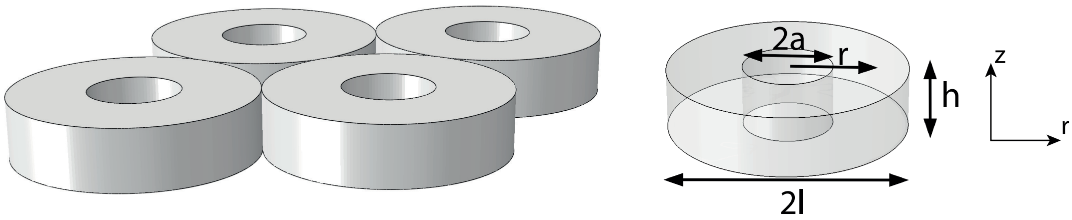

Figure 2.1: Idealization of pores within a plane as cylinders and dimensions of the RVE.

– $\delta_n = 0$ at $z = 0$, longitudinal displacement, δ_n, is fixed at the bottom surface of RVE.
– $u = 0$ at $r = l$, radial displacement, u, at outer lateral surface is zero, i.e. in plane macroscopic strain is zero.
– δ_n at $z = h$, displacement is applied at the top surface of RVE.

For mode-I loading, RVE is displaced by δ_n in z direction (Fig. 2.2). Since it is constrained, rate of displacement in normal direction is $\dot{\delta}_n = \dot{h}$. This is another advantage of the cylindrical RVE, a simple velocity field, $\dot{\delta}_n = \dot{h}$, is obtained with the given boundary conditions. If a space-filling cubic RVE were used, pore growth and the velocity field would be more complex. Apply upper bound theorem, which states work done by the limit load is smaller or equal to the integral energy dissipation of the effective strain rate at yield stress.

$$\pi l^2 T_n \dot{\delta}_n \leq \int_a^l \dot{\varepsilon_e} \sigma_y 2\pi r h dr \tag{2.1}$$

Assuming the material is rigid-perfectly plastic, incompressibility condition gives $\dot{\varepsilon_r} + \dot{\varepsilon_\theta} + \dot{\varepsilon_z} = 0$, in polar coordinates. Using small strain-displacement relations $\dot{\varepsilon_z} = \dot{h}/h,\ \dot{\varepsilon_\theta} = \dot{u}/r,\ \dot{\varepsilon_r} = d\dot{u}/dr$ for axisymmetric loading we have,

$$\frac{d\dot{u}}{dr} + \frac{\dot{u}}{r} + \frac{\dot{h}}{h} = 0 \text{ or } \frac{d\dot{u}}{dr} + \frac{1}{r}\dot{u} = -\frac{\dot{h}}{h}$$

This is a first order linear ordinary differential equation (ODE) with the boundary condition $\dot{u} = 0$ at $r = l$. For the general first order linear ODE, $\dot{y} + a(x)y = f(x)$, solution is given by,

$$y = \frac{\int u(x) f(x) dx + C}{u(x)} \quad \text{where } u(x) = e^{\int a(x)dx} \text{ is integrating factor}$$

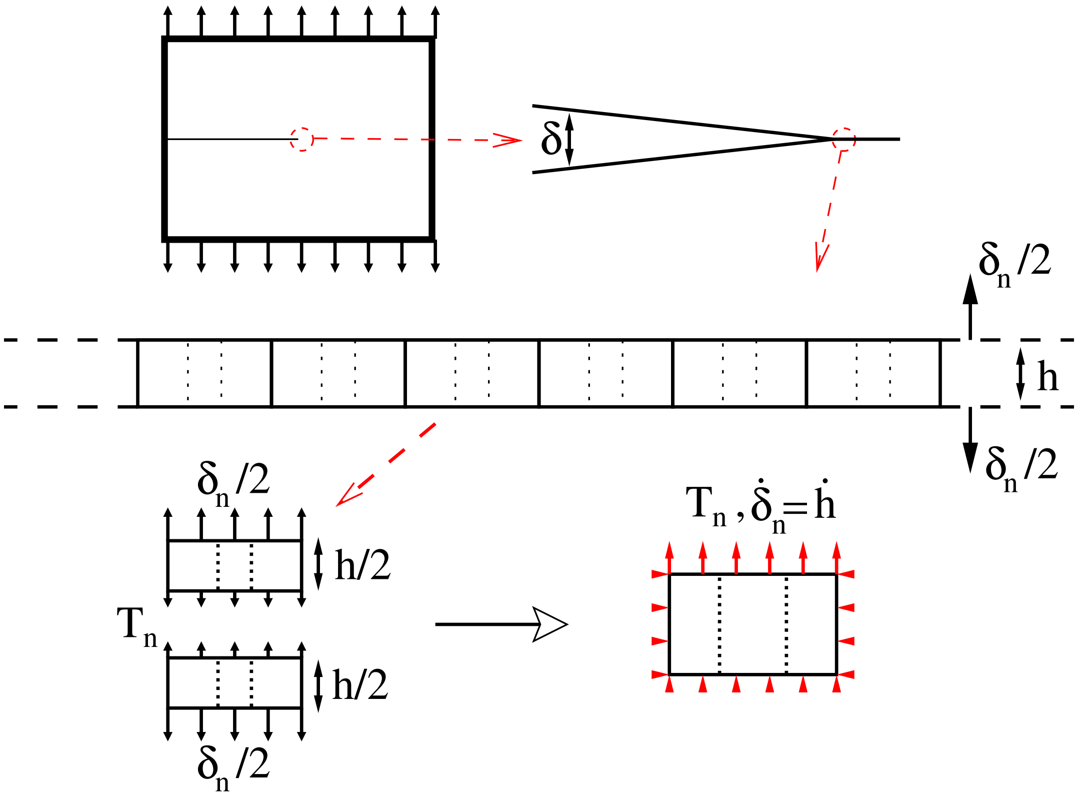

Figure 2.2: Crack opening represented by RVEs under mode-I loading.

Applying it to our equation, integrating factor becomes,

$$e^{\int 1/r dr} = e^{lnr} = r$$

And solution is given by,

$$\dot{u} = \frac{\displaystyle\int r\frac{-\dot{h}}{h}dr + C}{r} = \frac{-\dfrac{r^2}{2}\dfrac{\dot{h}}{h} + C}{r} = -\frac{r}{2}\frac{\dot{h}}{h} + \frac{C}{r}$$

where C is a constant. Applying boundary condition $\dot{u} = 0$ at $r = l$, C is found as,

$$0 = -\frac{l}{2}\frac{\dot{h}}{h} + \frac{C}{l} \quad \text{or} \quad C = \frac{\dot{h}}{h}\frac{l^2}{2}$$

Noting that $\dot{\varepsilon_z} = \dot{h}/h$, we obtain,

$$\begin{aligned} \dot{u} = (\dot{\varepsilon_z} r/2)(l^2/r^2 - 1), \quad \dot{\varepsilon_\theta} = \frac{\dot{u}}{r} &= \frac{\dot{\varepsilon_z}}{2}\left(\frac{l^2}{r^2} - 1\right) \\ \dot{\varepsilon_r} = -(\dot{\varepsilon_\theta} + \dot{\varepsilon_z}) &= -\frac{\dot{\varepsilon_z}}{2}\left(\frac{l^2}{r^2} + 1\right) \end{aligned} \qquad (2.2)$$

Then, using (2.2) effective strain rate can be written as,

$$\dot{\varepsilon}_e = \sqrt{\frac{2}{9}\left[(\dot{\varepsilon_r} - \dot{\varepsilon_\theta})^2 + (\dot{\varepsilon_r} - \dot{\varepsilon_z})^2 + (\dot{\varepsilon_\theta} - \dot{\varepsilon_z})^2\right]} = \dot{\varepsilon_z}\sqrt{1 + \frac{l^4}{3r^4}} \tag{2.3}$$

Noting $\dot{\delta}_n = \dot{h}$ and $\dot{\varepsilon}_z = \dot{h}/h$, and substituting (2.2) and (2.3) into (2.1), we get,

$$T_n \leq \sigma_y \int_f^1 \sqrt{1 + \left(\frac{1}{3\nu^2}\right)} d\nu$$

$$\text{where} \;\; \nu = r^2/l^2, \;\; d\nu = 2r/l^2 dr \;\; \text{and} \;\; f = a^2/l^2 \tag{2.4}$$

with f being the area fraction of pores.

Now, the integral in (2.4) can be evaluated in two ways [93].

$$\text{Minkowski inequality:} \; \left(\int (f+g)^k dx\right)^{\frac{1}{k}} > \left(\int f^k dx\right)^{\frac{1}{k}} + \left(\int g^k dx\right)^{\frac{1}{k}} \; \text{or}$$

$$\text{Jensen's inequality:} \; \int (f+g)^k dx < \int f^k dx + \int g^k dx \;\; \text{where} \;\; k < 1$$

Using Jensen's inequality retains the upper bound theorem's formal nature, while the Minkowski inequality is a better approximation of the integral but is the opposite sense of the upper bound theorem. Additionally, Minkowski inequality results in a continuous function for mixed-mode loading while Jensen's inequality results in a discontinuous one. Depending on the inequality, different traction-separation equations are obtained, each having their merits and demerits, which can be calibrated with experiments. Both ways will be shown here. It should be noted that the upper bounds obtained by using these inequalities are in a strict sense only estimates.

Applying Jensen's inequality to (2.4) gives,

$$\int_f^1 \sqrt{1 + \frac{1}{3v^2}} dv < \int_f^1 \sqrt{1} dv + \int_f^1 \sqrt{\frac{1}{3v^2}} dv$$

$$\int_f^1 \sqrt{1 + \frac{1}{3v^2}} dv < (1-f) + \int_f^1 \frac{1}{\sqrt{3}|v|} dv \;\; \text{where} \;\; f > 0$$

$$\int_f^1 \sqrt{1 + \frac{1}{3v^2}} dv < (1-f) + \frac{1}{\sqrt{3}} ln \frac{1}{f}$$

$$T_n \leq \sigma_y \left[(1-f) + \left(\frac{1}{\sqrt{3}} ln \frac{1}{f} \right) \right] \tag{2.5}$$

or the yield function,

$$g = \frac{T_n}{(1-f) + \frac{1}{\sqrt{3}} ln \frac{1}{f}} - \sigma_y = \overline{\sigma} - \sigma_y \tag{2.6}$$

Applying Minkowski inequality to (2.4) gives,

$$\left[\int_f^1 \sqrt{1 + \frac{1}{3v^2}} dv \right]^2 > \left[\int_f^1 \sqrt{1} dv \right]^2 + \left[\int_f^1 \sqrt{\frac{1}{3v^2}} dv \right]^2$$

$$\left[\int_f^1 \sqrt{1 + \frac{1}{3v^2}} dv \right]^2 > (1-f)^2 + \left[\int_f^1 \frac{1}{\sqrt{3}|v|} dv \right]^2 \quad \text{where } \ f > 0$$

$$\left[\int_f^1 \sqrt{1 + \frac{1}{3v^2}} dv \right]^2 > (1-f)^2 + \left[\frac{1}{\sqrt{3}} ln \frac{1}{f} \right]^2$$

$$\int_f^1 \sqrt{1 + \frac{1}{3v^2}} dv > \left[(1-f)^2 + \left[\frac{1}{\sqrt{3}} ln \frac{1}{f} \right]^2 \right]^{\frac{1}{2}}$$

$$T_n \approx \sigma_y \left[(1-f)^2 + \left(\frac{1}{\sqrt{3}} ln \frac{1}{f} \right)^2 \right]^{\frac{1}{2}} \tag{2.7}$$

which is no longer an upper bound, but an approximation. In yield function form,

$$g = \left[\frac{T_n^2}{(1-f)^2 + \left(\frac{1}{\sqrt{3}} ln \frac{1}{f} \right)^2} \right]^{\frac{1}{2}} - \sigma_y = \overline{\sigma} - \sigma_y \tag{2.8}$$

(2.7) and (2.5) give traction as a function of pore fraction, f. Thus, the evolution of f is needed to calculate the traction. Since the matrix is incompressible, the conservation of volume can be used to find it. For a change dh in height, the pore radius will grow by da,

$$\begin{aligned}\pi(l^2-a^2)h =&\pi(l^2-(a+da)^2)(h+dh)\\(l^2-a^2)h =&(l^2-a^2-2ada-da^2)(h+dh)\\2ahda =&(l^2-a^2)dh \text{ where } f=a^2/l^2\\\frac{2ada}{l^2}h =&(1-f)dh \text{ where } df=2ada/l^2\\hdf =&(1-f)dh\end{aligned}$$

Then, evolution equations are,

$$\begin{aligned}df =&\frac{dh}{h}(1-f)\\dh =&d\delta_n \quad \text{from boundary condition.}\end{aligned}$$

Assuming $f=f_0$ when $h=h_0$, it can be written,

$$\begin{aligned}\int_{f_0}^{f}\frac{df}{1-f} =&\int_{h_0}^{h}\frac{dh}{h}\\-ln(1-f)|_{f_0}^{f} =&lnh|_{h_0}^{h}\\\frac{1-f}{1-f_0} =&\frac{h_0}{h}\end{aligned}$$

Also assume that $h=h_0$ when $\delta_n=0$. Using $dh=d\delta_n$, we have $h=h_0+\delta_n$. Substituting,

$$\begin{aligned}1-f =&\frac{h_0(1-f_0)}{h_0+\delta_n}\\f =&\frac{\delta_n+h_0f_0}{\delta_n+h_0}\end{aligned}$$

Then, substituting f to (2.5) gives T_n for Jensen's inequality,

$$T_n=\sigma_y\left[\frac{h_0(1-f_0)}{(\delta_n+h_0)}+\frac{1}{\sqrt{3}}ln\left(\frac{(\delta_n+h_0)}{(\delta_n+h_0f_0)}\right)\right] \tag{2.9}$$

And, substituting to (2.7) gives T_n for Minkowski inequality.

$$T_n=\sigma_y\left[\left(\frac{h_0(1-f_0)}{(\delta_n+h_0)}\right)^2+\left(\frac{1}{\sqrt{3}}ln\left(\frac{(\delta_n+h_0)}{(\delta_n+h_0f_0)}\right)\right)^2\right]^{\frac{1}{2}} \tag{2.10}$$

Figure 2.3 shows the variation of T_n with δ_n for Jensen's and Minkowski inequality respectively. Maximum traction decreases with increasing f_0 and decrease rate of

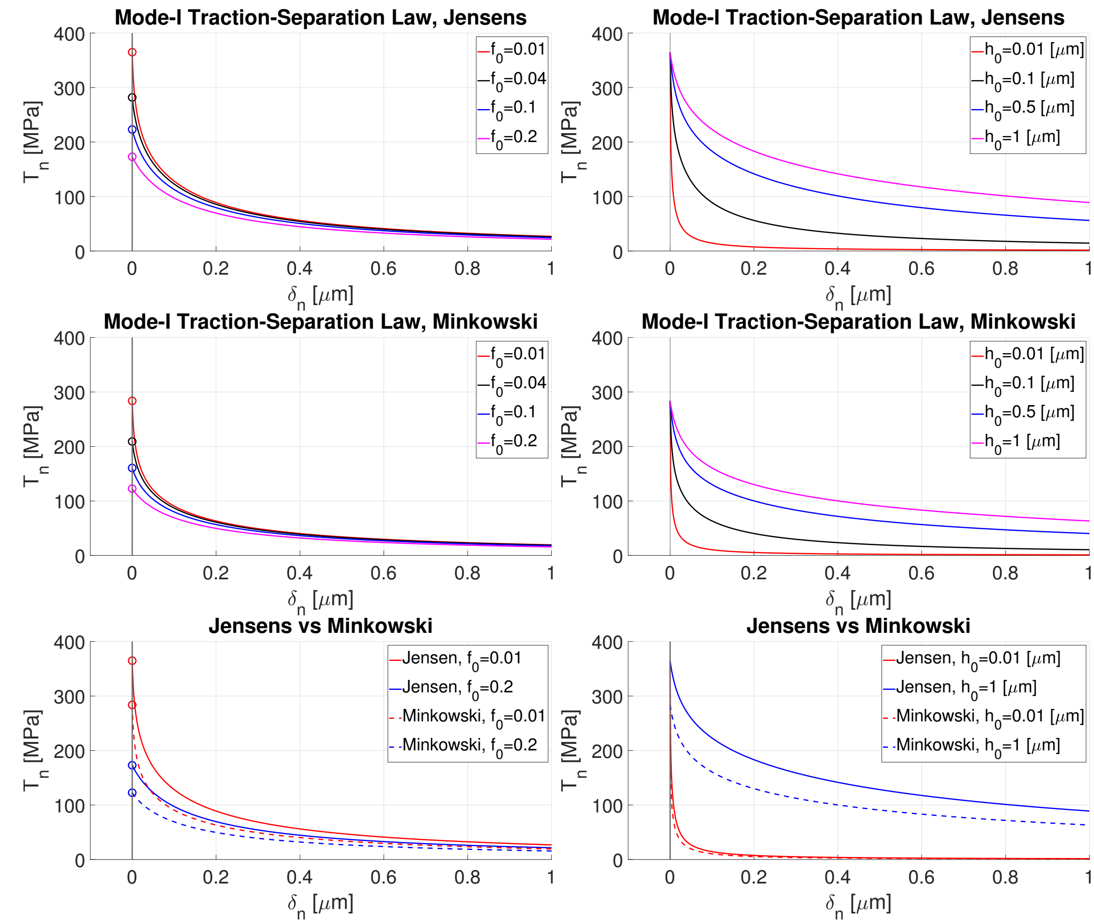

Figure 2.3: Dependence of Mode-I traction-separation law on initial volume fraction and height of voids for $\sigma_y = 100$ MPa and $h_0 = 0.2\mu m$ (left) and $f_0 = 0.01$ (right), by using Jensen's inequality (top) and Minkowski inequality (middle), and a comparison of them (bottom).

traction is controlled by h_0. Pores can obtain an elliptical shape during growth. h_0 is an idealized means to represent that elliptical shape. If h_0 is small, pore is like a crack and it can grow faster under normal, mode-I, loading.

2.2 Traction-separation relation for Mode-II loading

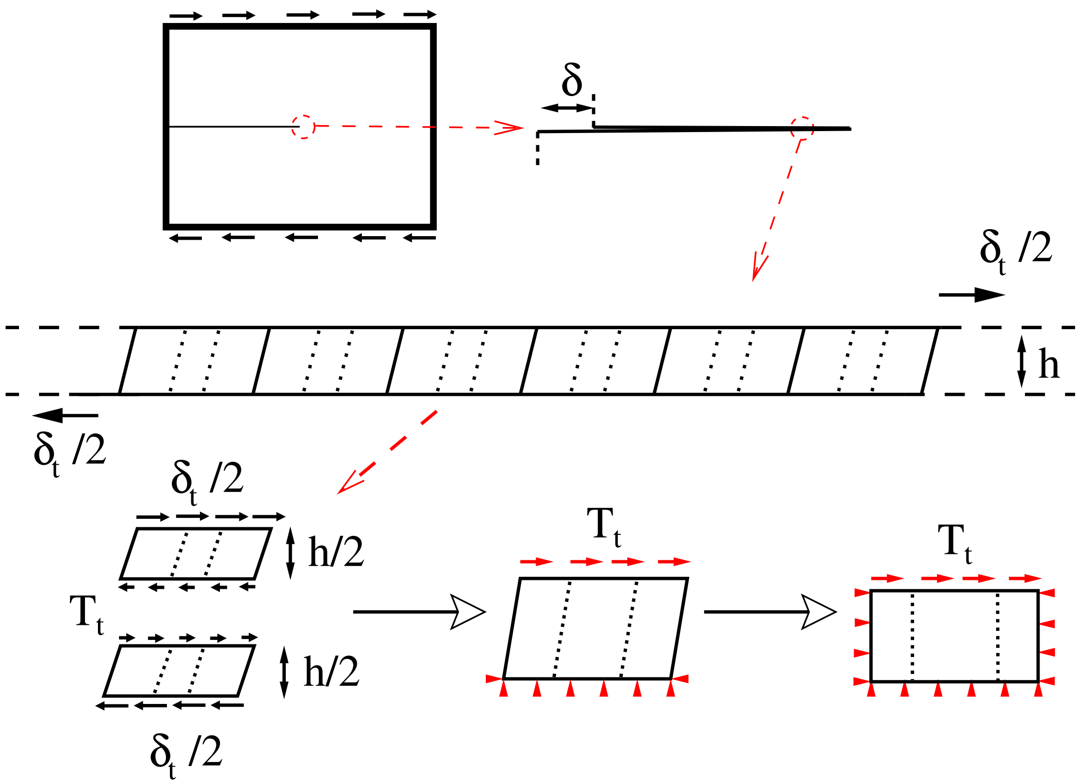

Figure 2.4: Crack opening represented by RVEs under mode-I loading.

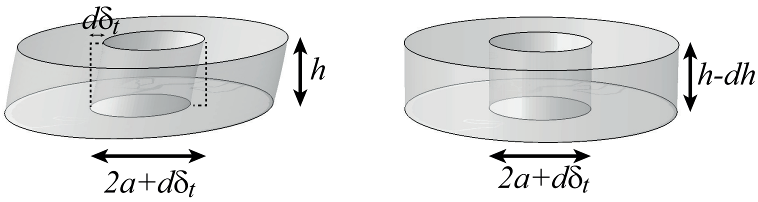

Figure 2.5: Geometry change under shear loading.

Similar to mode-I, in Fig. 2.4, under mode-II loading fracture process zone is represented by the RVEs. For mode-II, RVE is loaded in radial direction. Shear loading elongates the pores in the direction of shear and causes them to be more like a crack [94](see Fig. 2.5 (left)). The new shape can be approximated as shown in Fig. 2.5(right). Upper bound theorem for mode-II loading gives,

$$\pi l^2 T_t \dot{\delta}_t \leq \int_a^l \dot{\varepsilon}_e \sigma_y 2\pi r h dr \tag{2.11}$$

For pure mode-II effective strain rate can be written as,

$$\dot{\varepsilon}_e = \sqrt{\dot{\gamma}^2/3} \quad \text{where} \quad \dot{\gamma} = \dot{\delta}_t/h$$

Substituting and applying the change of variables given in (2.4),

$$T_t \le \sigma_y \int_f^1 \sqrt{\left(\frac{1}{3}\right)} d\nu \ \text{ or } \ T_t \le \frac{\sigma_y}{\sqrt{3}}(1-f) \tag{2.12}$$

In yield function form,

$$g = \frac{\sqrt{3}T_t}{(1-f)} - \sigma_y = \overline{\sigma} - \sigma_y \tag{2.13}$$

Again, the evolution of pore fraction is needed. From the definition of pore fraction, $f = a^2/l^2$,

$$df = \frac{2a}{l}\frac{da}{l} = 2\sqrt{f}\frac{d\delta_t}{l} \ \text{ where } \ da = d\delta_t$$

In shear deformation assuming volume of the RVE is preserved, it can be written,

$$\begin{aligned}\pi(2a)^2 h =& \pi(2a + d\delta_t)^2(h - dh)\\ \pi 4a^2 h =& \pi 4a^2 h + 4\pi a h d\delta_t - 4\pi a^2 dh\\ dh =& \frac{d\delta_t}{a} h\end{aligned}$$

Similar to Mode-I, assume that $f = f_0$ when $\delta_t = 0$,

$$\begin{aligned}\int_{f_0}^{f} \frac{df}{2\sqrt{f}} =& \int_0^{\delta_t} \frac{d\delta_t}{l}\\ \sqrt{f}|_{f_0}^{f} =& \frac{\delta_t}{l}|_0^{\delta_t}\\ f =& \left(\sqrt{f_0} + \frac{\delta_t}{l}\right)^2\end{aligned}$$

Substituting to (2.14), mode-II traction-separation law is obtained in terms of initial pore fraction, f_0, and pore spacing l.

$$T_t = \frac{\sigma_y}{\sqrt{3}}\left[1 - \left(\sqrt{f_0} + \frac{\delta_t}{l}\right)^2\right] \tag{2.14}$$

Figure 2.6 show the variation of T_t with δ_t.

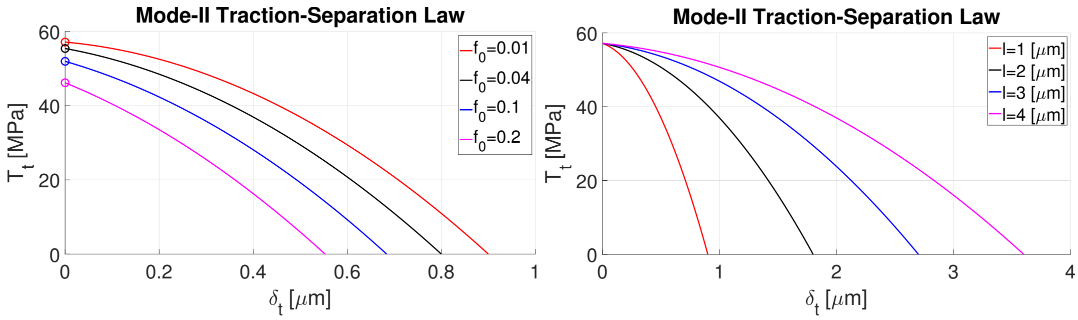

Figure 2.6: Mode-II traction-separation equation for $\sigma_y = 100$ MPa and $l = 1\mu m$ with changing f_0 (left), and $f_0 = 0.01$ with changing l (right).

2.3 Traction-separation relation for Mixed-Mode loading

Remember for mode-I loading, $dh = d\delta_n$ and $df = d\delta_n(1-f)/h$. And, for mode-II loading, $dh = d\delta_t(h/a)$ and $df = d\delta_t(2\sqrt{f}/l)$. Note that for mode-II dh is negative for positive δ_t. Superposing, for combined normal and shear deformation we get,

$$\begin{aligned} df &= d\delta_n \frac{(1-f)}{h} + d\delta_t \frac{2\sqrt{f}}{l} \\ dh &= d\delta_n - d\delta_t \frac{h}{a} \end{aligned} \tag{2.15}$$

Upper bound theorem for mixed-mode gives,

$$T_n\dot{\delta}_n + T_t\dot{\delta}_t \leq \sigma_y \int_f^1 \sqrt{\dot{\delta}_n^2\left(1+\frac{1}{3\nu^2}\right) + \frac{\dot{\delta}_t^2}{3}} d\nu \quad \text{where} \quad \nu = \frac{r^2}{l^2} \tag{2.16}$$

Applying Jensen inequality to 2.16 gives,

$$T_n\dot{\delta}_n + T_t\dot{\delta}_t \leq \sigma_y \left[\int_f^1 \sqrt{\dot{\delta}_n^2\left(1+\frac{1}{3\nu^2}\right)} dv + \int_f^1 \sqrt{\frac{\dot{\delta}_t^2}{3}} dv\right]$$

$$T_n\dot{\delta}_n + T_t\dot{\delta}_t \leq \sigma_y \left[\dot{\delta}_n \int_f^1 \sqrt{1+\frac{1}{3\nu^2}} dv + \dot{\delta}_t \int_f^1 \sqrt{\frac{1}{3}} dv\right]$$

The first integral on the right hand side was found before for pure mode-I. Substituting,

$$T_n\dot{\delta}_n + T_t\dot{\delta}_t \leq \sigma_y \left[\dot{\delta}_n \left((1-f) + (\frac{1}{\sqrt{3}} ln\frac{1}{f})\right) + \dot{\delta}_t \left(\frac{1-f}{\sqrt{3}}\right)\right]$$

Letting $\bar{\dot{\delta}} = \dot{\delta}_t/\dot{\delta}_n$,

$$T_n\dot{\delta}_n\left(1+\frac{T_t}{T_n}\bar{\dot{\delta}}\right) \leq \sigma_y\dot{\delta}_n\left[\left((1-f)+(\frac{1}{\sqrt{3}}ln\frac{1}{f})\right)+\bar{\dot{\delta}}\left(\frac{1-f}{\sqrt{3}}\right)\right]$$

For a specified T_t/T_n,

$$T_n \leq \frac{\sigma_y\left[\left((1-f)+\frac{1}{\sqrt{3}}ln\frac{1}{f}\right)+(1-f)\frac{\bar{\dot{\delta}}}{\sqrt{3}}\right]}{\left(1+\frac{T_t}{T_n}\bar{\dot{\delta}}\right)} \quad \text{where} \quad \bar{\dot{\delta}} = \frac{\dot{\delta}_t}{\dot{\delta}_n} \tag{2.17}$$

R.H.S is minimized by $\bar{\dot{\delta}} = 0$ or $\bar{\dot{\delta}} = \infty$ which gives,

$$T_n \leq \sigma_y\left[(1-f)+\frac{1}{\sqrt{3}}ln\frac{1}{f}\right] \tag{2.18}$$

$$T_t \leq \frac{\sigma_y}{\sqrt{3}}(1-f) \tag{2.19}$$

respectively.

Applying Minkowski inequality to (2.16) gives,

$$\left[\int_f^1\sqrt{\dot{\delta}_n^2\left(1+\frac{1}{3\nu^2}\right)+\frac{\dot{\delta}_t^2}{3}dv}\right]^2 > \left[\int_f^1\sqrt{\dot{\delta}_n^2\left(1+\frac{1}{3\nu^2}\right)dv}\right]^2 + \left[\int_f^1\sqrt{\frac{\dot{\delta}_t^2}{3}dv}\right]^2$$

$$\int_f^1\sqrt{\dot{\delta}_n^2\left(1+\frac{1}{3\nu^2}\right)+\frac{\dot{\delta}_t^2}{3}dv} > \left[\dot{\delta}_n^2\left[\int_f^1\sqrt{\left(1+\frac{1}{3\nu^2}\right)dv}\right]^2+\dot{\delta}_t^2\left[\int_f^1\sqrt{\frac{1}{3}dv}\right]^2\right]^{\frac{1}{2}}$$

Again, the first integral on the right hand side was found before for pure mode-I. Substituting,

$$\int_f^1\sqrt{\dot{\delta}_n^2\left(1+\frac{1}{3\nu^2}\right)+\frac{\dot{\delta}_t^2}{3}dv} > \left[\dot{\delta}_n^2\left[(1-f)^2+\left(\frac{1}{\sqrt{3}}ln\frac{1}{f}\right)^2\right]+\frac{\dot{\delta}_t^2}{3}(1-f)^2\right]^{\frac{1}{2}}$$

Then,

$$T_n\dot{\delta}_n + T_t\dot{\delta}_t \approx \sigma_y\left(\dot{\delta}_n^2\left[(1-f)^2+\left(\frac{1}{\sqrt{3}}ln\frac{1}{f}\right)^2\right]+\frac{\dot{\delta}_t^2}{3}(1-f)^2\right)^{\frac{1}{2}}$$

Letting $\bar{\dot{\delta}} = \dot{\delta}_t/\dot{\delta}_n$,

$$T_n\dot{\delta}_n\left(1+\frac{T_t}{T_n}\bar{\dot{\delta}}\right) \approx \sigma_y\dot{\delta}_n\left(\left[(1-f)^2+\left(\frac{1}{\sqrt{3}}ln\frac{1}{f}\right)^2\right]+\frac{\bar{\dot{\delta}}^2}{3}(1-f)^2\right)^{\frac{1}{2}}$$

$$T_n \approx \frac{\sigma_y\left(\left[(1-f)^2+\left(\frac{1}{\sqrt{3}}ln\frac{1}{f}\right)^2\right]+\frac{\bar{\dot{\delta}}^2}{3}(1-f)^2\right)^{\frac{1}{2}}}{\left(1+\frac{T_t}{T_n}\bar{\dot{\delta}}\right)} \quad \text{where} \quad \bar{\dot{\delta}} = \frac{\dot{\delta}_t}{\dot{\delta}_n}$$

Minimize RHS by finding the $\bar{\dot{\delta}}$, where $\dfrac{\partial(RHS)}{\partial\bar{\dot{\delta}}} = 0$. Taking derivative of RHS, and letting $A = \left[(1-f)^2+\left(\frac{1}{\sqrt{3}}ln\frac{1}{f}\right)^2\right]+\dfrac{\bar{\dot{\delta}}^2}{3}(1-f)^2$,

$$0 = \frac{\frac{1}{2}(A)^{-\frac{1}{2}}\left(\frac{2}{3}(1-f)^2\bar{\dot{\delta}}\right)\left(1+\frac{T_t}{T_n}\bar{\dot{\delta}}\right)-(A)^{\frac{1}{2}}\left(\frac{T_t}{T_n}\right)}{\left(1+\frac{T_t}{T_n}\bar{\dot{\delta}}\right)^2}$$

$$(A)\left(\frac{T_t}{T_n}\right) = \frac{1}{2}\left(\frac{2}{3}(1-f)^2\bar{\dot{\delta}}\right)\left(1+\frac{T_t}{T_n}\bar{\dot{\delta}}\right)$$

$$\left[(1-f)^2+\left(\frac{1}{\sqrt{3}}ln\frac{1}{f}\right)^2\right]\frac{T_t}{T_n}+\frac{\bar{\dot{\delta}}^2}{3}(1-f)^2\frac{T_t}{T_n} = \frac{\bar{\dot{\delta}}(1-f)^2}{3}+\frac{\bar{\dot{\delta}}^2}{3}(1-f)^2\frac{T_t}{T_n}$$

$$\bar{\dot{\delta}} = \frac{3}{(1-f)^2}\frac{T_t}{T_n}\left[(1-f)^2+\left(\frac{1}{\sqrt{3}}ln\frac{1}{f}\right)^2\right]$$

Substitute $\bar{\dot{\delta}}$ back into RHS,

$$T_n \approx \frac{\sigma_y\left[\left[(1-f)^2+\left(\frac{1}{\sqrt{3}}ln\frac{1}{f}\right)^2\right]+\frac{3\left[\frac{T_t}{T_n}\right]^2}{(1-f)^2}\left[(1-f)^2+\left(\frac{1}{\sqrt{3}}ln\frac{1}{f}\right)^2\right]^2\right]^{\frac{1}{2}}}{\left(1+\frac{3}{(1-f)^2}\left(\frac{T_t}{T_n}\right)^2\left[(1-f)^2+\left(\frac{1}{\sqrt{3}}ln\frac{1}{f}\right)^2\right]\right)}$$

$$T_n \approx \frac{\sigma_y \left[(1-f)^2 + \left(\frac{1}{\sqrt{3}} ln\frac{1}{f}\right)^2\right]^{\frac{1}{2}} \left[1 + \frac{3\left[\frac{T_t}{T_n}\right]^2}{(1-f)^2}\left[(1-f)^2 + \left(\frac{1}{\sqrt{3}} ln\frac{1}{f}\right)^2\right]\right]^{\frac{1}{2}}}{\left(1 + \frac{3}{(1-f)^2}\left(\frac{T_t}{T_n}\right)^2\left[(1-f)^2 + \left(\frac{1}{\sqrt{3}} ln\frac{1}{f}\right)^2\right]\right)}$$

$$T_n \approx \frac{\sigma_y \left(\left[(1-f)^2 + \left(\frac{1}{\sqrt{3}} ln\frac{1}{f}\right)^2\right]\right)^{\frac{1}{2}}}{\left(1 + \frac{3}{(1-f)^2}\left(\frac{T_t}{T_n}\right)^2\left[(1-f)^2 + \left(\frac{1}{\sqrt{3}} ln\frac{1}{f}\right)^2\right]\right)^{\frac{1}{2}}}$$

$$\sigma_y \approx \frac{T_n\left(1 + \frac{3}{(1-f)^2}\left(\frac{T_t}{T_n}\right)^2\left[(1-f)^2 + \left(\frac{1}{\sqrt{3}} ln\frac{1}{f}\right)^2\right]\right)^{\frac{1}{2}}}{\left(\left[(1-f)^2 + \left(\frac{1}{\sqrt{3}} ln\frac{1}{f}\right)^2\right]\right)^{\frac{1}{2}}}$$

$$\sigma_y \approx \frac{\left(T_n^2 + \frac{3T_t^2}{(1-f)^2}\left[(1-f)^2 + \left(\frac{1}{\sqrt{3}} ln\frac{1}{f}\right)^2\right]\right)^{\frac{1}{2}}}{\left(\left[(1-f)^2 + \left(\frac{1}{\sqrt{3}} ln\frac{1}{f}\right)^2\right]\right)^{\frac{1}{2}}}$$

$$\left(\frac{T_n^2}{\left((1-f)^2 + \left(\frac{1}{\sqrt{3}} ln\frac{1}{f}\right)^2\right)} + \frac{3T_t^2}{(1-f)^2}\right)^{\frac{1}{2}} - \sigma_y \approx 0$$

Results in the yield function,

$$g = \left[\frac{T_n^2}{(1-f)^2 + \left(\frac{1}{\sqrt{3}} ln\frac{1}{f}\right)^2} + \frac{3T_t^2}{(1-f)^2}\right]^{\frac{1}{2}} - \sigma_y = \overline{\sigma} - \sigma_y \qquad (2.20)$$

Notice that letting $T_t = 0$ in (2.20) would give the same result for T_n as previous section (2.8), and (2.18) is already the same as before (2.5). And, by letting $T_n = 0$ in (2.20), we get the same form as (2.19) for pure mode-II loading.

Now, the traction-separation relations for mode-I-II and mixed-mode loadings are obtained. Note that the Minkowski version of TSLs, equations (2.10) and (2.20), will be used in implementation since it results in a continuous yield function for mixed-mode. Tractions are expressed as a function of pore fraction, f. In pure mode cases f can be determined as a function of separation $\delta_{n,t}$. However, for the mixed-mode case, an explicit expression does not exist. Instead, there is a yield function including normal-tangential traction and f, obtained by applying the upper-bound theorem. This nature results in an intrinsic mixed-mode capability, where the evolution of f is driven by both δ_n and δ_t. Hence, tractions for mixed-mode are evaluated by utilizing an implicit numerical integration scheme similar to plasticity. Details of implementation are given in the next chapter.

CHAPTER 3

NUMERICAL IMPLEMENTATION OF MBCZM

The traction-separation relations are implemented into Abaqus as a user-defined element (UEL). In the simplest form, Abaqus provides the displacements at the nodes of the element and expects the residual force vector (RHS) and the Jacobian (stiffness) matrix (AMATRX) in return. These matrices can be calculated with the normal and tangential tractions, and their derivatives with respect to normal and tangential separations.

First, the finite element framework for a 2D, 4 node element is presented in detail. The weak form of the problem is explained. The shape functions and global to local transformation matrices are shown for the 4-noded linear cohesive element. With these, the internal force vector and the tangent matrix of a cohesive surface element can be found.

Second, the numerical procedure is shown using the uncoupled form of traction-separation relations for pure mode-I and mode-II problems. In uncoupled form, traction can be expressed analytically in terms of separations. Tractions and their derivatives are implemented into the UEL subroutine. An algorithm including contact, loading, unloading, and failure conditions is presented. The subroutine is tested with a simple model, where a single cohesive element is placed between two bulk elements. Next, the traction-separation relations are derived in incremental form, later to be implemented in mixed-mode. The incremental form is compared with the analytical form.

Third, mixed-mode implementation scheme is presented. In the mixed-mode tractions cannot be written explicitly but as a yield function. Therefore, a plasticity formulation is used to satisfy the yield function for mixed-mode. This formulation is summarized for the general plasticity case. Then, it is applied to our cohesive zone model framework for mode-I, mode-II and finally mixed-mode.

The micromechanics based TSL is an initially rigid (extrinsic) model with no initial elastic region; there is only softening. This type of cohesive zone models require mesh manipulation during analysis, and they are difficult to implement. Therefore, for the ease of implementation, an initial elastic part is added to micromechanics based TSL for all implementation schemes turning it into an initially elastic (intrinsic) cohesive zone model. The elastic regime is chosen very small compared to the softening part in order to capture the original behavior.

3.1 Finite element framework

The weak form of the problem is obtained from the principal of virtual work. Work done by the external tractions on the boundary is equal to the summation of virtual strain energy in the domain (Ω) and the cohesive fracture energy on the fracture surface (Γ_f).

$$\int_{\Gamma} \mathbf{T}_{ext} \mathrm{d}\mathbf{u} \; \mathrm{d}S \;=\; \int_{\Omega} \boldsymbol{\sigma} : \mathrm{d}\boldsymbol{\varepsilon} \; \mathrm{d}V \;+\; \int_{\Gamma_f} \mathbf{T} \mathrm{d}\boldsymbol{\delta} \; \mathrm{d}S \tag{3.1}$$

where $\mathrm{d}\mathbf{u}$, $\mathrm{d}\boldsymbol{\varepsilon}$ and $\mathrm{d}\boldsymbol{\delta}$ are virtual displacement, virtual strain and virtual separation, respectively. In addition, $\boldsymbol{\sigma}$ is the Cauchy stress tensor, while $\mathbf{T}$ is cohesive traction along the fracture surface. The first term on the right-hand side of Eq. (3.1) is associated with the internal force of bulk elements, while the second term is related to the internal cohesive force of cohesive surface elements. The term on the left-hand side of Eq. (3.1) corresponds to the external force.

Following the finite element discretization, the displacement field $\mathbf{u}$ is approximated by interpolation of nodal displacements $\overline{\boldsymbol{u}}$ with shape functions,

$$\mathbf{u}(\mathbf{X}) = \mathbf{N}\overline{\boldsymbol{u}} \tag{3.2}$$

where $\mathbf{N}$ is a shape function matrix, and $\mathbf{X}$ denotes the global coordinates.

In addition, the local separation $\boldsymbol{\delta}$ is approximated by using the nodal displacement $\overline{\boldsymbol{u}}$. In order to obtain the local separation based on the global nodal displacement, the global coordinates $\mathbf{X}$ are first transformed to the local coordinates $\mathbf{x}$ of a cohesive element, i.e.

$$\mathbf{x} = \boldsymbol{\Lambda} \boldsymbol{X} \tag{3.3}$$

where $\boldsymbol{\Lambda}$ is a coordinate transformation matrix. Using a rotational matrix $\mathbf{R}$ consisting of $\boldsymbol{\Lambda}$, the global node displacement $\overline{\boldsymbol{u}}$ is transformed to the local node displacement $\overline{\boldsymbol{v}}$.

$$\overline{\boldsymbol{v}} = \mathbf{R}\overline{\boldsymbol{u}} \tag{3.4}$$

From local displacements, one can obtain normal and tangential separations of the cohesive element ($\overline{\boldsymbol{\delta}}$).

$$\overline{\boldsymbol{\delta}} = \mathbf{L}\overline{\boldsymbol{v}} \tag{3.5}$$

where $\mathbf{L}$ is the local displacement-separation relation matrix. Then, separation along a cohesive element is found using shape functions.

$$\boldsymbol{\delta}(\boldsymbol{x}) = \mathbf{N}\overline{\boldsymbol{\delta}} \tag{3.6}$$

Substitution of (3.4) and (3.5) into (3.6) gives,

$$\boldsymbol{\delta}(\boldsymbol{x}) = \mathbf{NLR}\overline{\boldsymbol{u}} = \mathbf{B}\overline{\boldsymbol{u}} \tag{3.7}$$

where $\mathbf{B}$ is a global displacement-separation transformation matrix.

The internal force vector $\mathbf{f}_{coh}$ of a cohesive element can be found from the local traction by using transpose of global displacement-separation transformation matrix.

$$\mathbf{f}_{coh} = \int_{\Gamma_f} \boldsymbol{B}^{\boldsymbol{T}} \boldsymbol{T} dS \tag{3.8}$$

The gradient of the internal force vector leads to the tangent matrix $\mathbf{K}_{coh}$, i.e.

$$\mathbf{K}_{coh} = \frac{\partial \mathbf{f}_{coh}}{\partial \overline{\boldsymbol{u}}} = \int_{\Gamma_f} \boldsymbol{B}^{\boldsymbol{T}} \frac{\partial \mathbf{T}}{\partial \boldsymbol{\delta}} \frac{\partial \boldsymbol{\delta}}{\partial \overline{\boldsymbol{u}}} dS = \int_{\Gamma_f} \boldsymbol{B}^{\boldsymbol{T}} \frac{\partial \mathbf{T}}{\partial \boldsymbol{\delta}} \boldsymbol{B} dS \tag{3.9}$$

Traction vector $\mathbf{T}$ and tangent matrix $\partial \mathbf{T}/\partial \boldsymbol{\delta}$ are found from the micromechanics based traction separation law relations.

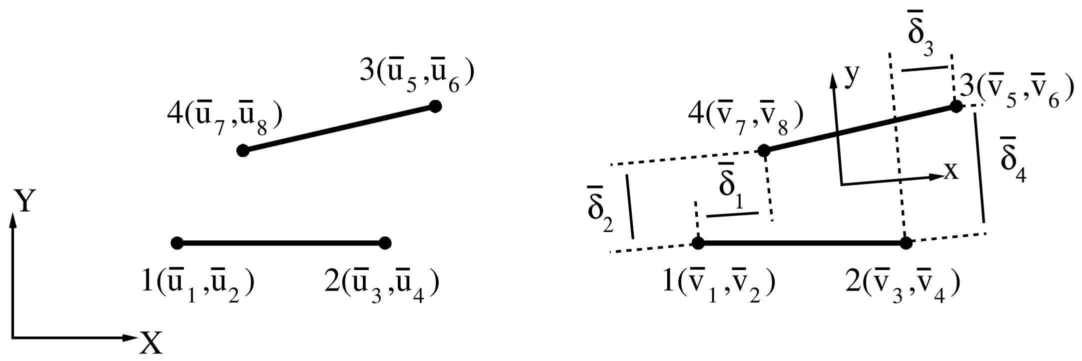

Figure 3.1: 2D linear cohesive surface element and nodal displacements in the global (left) and the local (right) coordinates.

This is the general framework applicable to 2D and 3D elements. Now, consider a 2D linear cohesive surface element (Fig. 3.1). This type of element has 4 nodes each with 2 degrees of freedom. Thus, the global nodal displacement vector is $\overline{\boldsymbol{u}} = (\overline{u}_1, \overline{u}_2, \overline{u}_3, \overline{u}_4, \overline{u}_5, \overline{u}_6, \overline{u}_7, \overline{u}_8)$. In Fig. 3.1, capital X and Y represent the gloabal coordinate system while small x and y represent the local coordinate system of the cohesive element. Notice that the x axis of the local coordinate system is the bisector of the angle between upper edge (node 3-4) and the lower edge (node 1-2) of cohesive element. This is according to the finite strain definition. In the local coordinate system, nodal displacements are $\overline{\boldsymbol{v}} = (\overline{v}_1, \overline{v}_2, \overline{v}_3, \overline{v}_4, \overline{v}_5, \overline{v}_6, \overline{v}_7, \overline{v}_8)$ which are obtained from the global coordinates by using the rotational matrix **R**,

$$\mathbf{R} = \begin{bmatrix} \boldsymbol{\Lambda} & \mathbf{0} & \mathbf{0} & \mathbf{0} \\ \mathbf{0} & \boldsymbol{\Lambda} & \mathbf{0} & \mathbf{0} \\ \mathbf{0} & \mathbf{0} & \boldsymbol{\Lambda} & \mathbf{0} \\ \mathbf{0} & \mathbf{0} & \mathbf{0} & \boldsymbol{\Lambda} \end{bmatrix} \quad \text{where} \quad \boldsymbol{\Lambda} = \begin{bmatrix} cos\theta & sin\theta \\ -sin\theta & cos\theta \end{bmatrix}$$

where θ is the angle between local and global coordinates. Then, in the local coordinate system, the separations at the ends of cohesive element are given as,

$$\overline{\delta}_1 = \overline{v}_7 - \overline{v}_1, \;\; \overline{\delta}_2 = \overline{v}_8 - \overline{v}_2, \;\; \overline{\delta}_3 = \overline{v}_5 - \overline{v}_3, \;\; \overline{\delta}_4 = \overline{v}_6 - \overline{v}_4, \tag{3.10}$$

which gives **L**,

$$\mathbf{L} = \begin{bmatrix} -1 & 0 & 0 & 0 & 0 & 0 & 1 & 0 \\ 0 & -1 & 0 & 0 & 0 & 0 & 0 & 1 \\ 0 & 0 & -1 & 0 & 1 & 0 & 0 & 0 \\ 0 & 0 & 0 & -1 & 0 & 1 & 0 & 0 \end{bmatrix}$$

Separation along the element is given by the shape function matrix **N**,

$$\mathbf{N} = \begin{bmatrix} N_1 & 0 & N_2 & 0 \\ 0 & N_1 & 0 & N_2 \end{bmatrix}$$

where $N_1 = \dfrac{1-\xi}{2}, \quad N_2 = \dfrac{1+\xi}{2}$ are linear shape functions.

By combining **N, L** and **R** matrices, the global displacement-separation relation matrix **B** is obtained,

$$\mathbf{B} = \begin{bmatrix} -CN_1 & -SN_1 & -CN_2 & -SN_2 & CN_2 & SN_2 & CN_1 & SN_1 \\ SN_1 & -CN_1 & SN_2 & -CN_2 & -SN_2 & CN_2 & -SN_1 & CN_1 \end{bmatrix}$$

where $C = cos\theta$ and $S = sin\theta$.

Finally, with **T** and $\partial\mathbf{T}/\partial\boldsymbol{\delta}$ from cohesive law, and **B** from finite element framework, the internal force vector (3.8) and the tangent matrix (3.9) can be calculated using Gauss quadrature numerical integration scheme. Note that similar steps are explained in the educational paper for PPR cohesive zone model implementation by Park and Paulino [95].

3.2 Mode I-II uncoupled implementation

Tractions in terms of separations and the derivatives of tractions with respect to separations are required. These relations can be obtained analytically for the micromechanics based cohesive zone model for pure mode I and mode II problems. As it is shown in equation (2.7), which gives normal traction in terms of normal separation. Similarly, (2.14) gives tangential traction in terms of tangential separation only. As stated before, to make the implementation easier, an elastic part is added to the traction relations making the cohesive zone model an initially elastic one. See Fig. 3.2

for a comparison. Note that the elastic slope is reasonably high so that the behavior is similar to the extrinsic model. Also, even tough it is called as elastic region, Poisson's ratio is not specified and it is not required to define a traction-separation relation, at the least this is the case for the phenomenological CZMs in the literature. However, the derived tractions are not phenomenological, and a poisson's ratio may be required, but even then the added elastic region is negligible compared to softening region. Therefore, this approach should not result in a significant error.

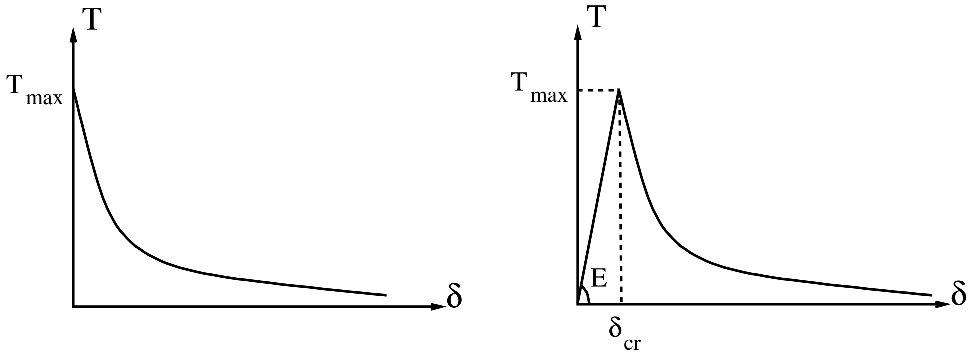

Figure 3.2: Initially rigid (extrinsic) and initially elastic (intrinsic) traction separation laws.

The tractions and the derivatives of tractions are evaluated by considering four cases: contact, loading, unloading/reloading and complete failure. See Algorithm 1 below for an outline, where $\delta_{n/t}$ are current normal/tangential separations, $T_{n/t}$ are normal/-tangential tractions, $D_{nn/nt/tt/tn}$ are derivatives of tractions with respect to separations, $\delta_{n/t,max}$ are maximum separations reached during the analysis, $\delta_{n/t,cr}$ are the critical separations where maximum traction is reached, $\delta_{t,final}$ is the final separation where tangential traction becomes zero, $E_{n/t}$ are the elastic part slopes, and f is the current pore fraction.

As it was shown in section 2, Eqns. (2.7)(2.14), if normal and tangential tractions are uncoupled, which is the case for pure mode I-II problems, the tractions in terms of separations can be analytically expressed, i.e.

$$T_n(f) = \sigma_y \left((1-f)^2 + \left(\frac{1}{\sqrt{3}} ln \frac{1}{f} \right)^2 \right)^{\frac{1}{2}} \text{ where } f = \frac{\delta_n + h_0 f_0}{\delta_n + h_0} \tag{3.11}$$

$$T_t(f) = \frac{\sigma_y}{\sqrt{3}}(1-f) \text{ where } f = \left(\sqrt{f_0} + \frac{\delta_t}{l} \right)^2 \tag{3.12}$$

–Normal cohesive interaction:

if $\delta_n < 0$ *(Contact)* **then**
| $T_n = D_{nn}\delta_n,\ \ D_{nn} = E_n,\ \ D_{nt} = 0$

else if $\delta_n \geqslant \delta_{n,max}$ *and* $\delta_n \leqslant \delta_{n,cr}$ *(Loading-Elastic)* **then**
| $T_n = D_{nn}\delta_n,\ \ D_{nn} = E_n,\ \ D_{nt} = 0$

else if $\delta_n \geqslant \delta_{n,max}$ *and* $\delta_n > \delta_{n,cr}$ *(Loading-Softening)* **then**
| $T_n = T_n(f),$ where $f = f(\delta_n),\ \ D_{nn} = \frac{\partial T_n}{\partial f}\frac{\partial f}{\partial \delta_n},\ \ D_{nt} = 0$

else if $\delta_n < \delta_{n,max}$ *(Unloading/reloading)* **then**
| $T_n = T_n(f_{max})\frac{\delta_n}{\delta_{n,max}},\ \ D_{nn} = T_n(f_{max})\frac{1}{\delta_{n,max}},\ \ D_{nt} = 0$

end

–Tangential cohesive interaction:

if $|\delta_t| \geqslant \delta_{t,max}$ *and* $|\delta_t| \leqslant \delta_{t,cr}$ *and* $|\delta_t| < \delta_{t_{final}}$ *(Loading-Elastic)* **then**
| $T_t = D_{tt}|\delta_t|sign(\delta_t),\ \ D_{tt} = E_t,\ \ D_{tn} = 0$

else if $|\delta_t| \geqslant \delta_{t,max}$ *and* $|\delta_t| > \delta_{t,cr}$ *and* $|\delta_t| < \delta_{t_{final}}$ *(Loading-Softening)*
then
| $T_t = T_t(f)sign(\delta_t),$ where $f = f(|\delta_t|),\ \ D_{tt} = \frac{\partial T_t}{\partial f}\frac{\partial f}{\partial \delta_t},\ \ D_{tn} = 0$

else if $|\delta_t| < \delta_{t,max}$ *and* $|\delta_t| < \delta_{t_{final}}$ *(Unloading/reloading)* **then**
| $T_t = T_t(f_{max})sign(\delta_t)\frac{|\delta_t|}{\delta_{t,max}},\ \ D_{tt} = T_t(f_{max})\frac{1}{\delta_{t,max}},\ \ D_{tn} = 0$

else if $|\delta_t| \geqslant \delta_{t_{final}}$ *(Failure)* **then**
| $T_t = 0,\ \ D_{tt} = 0,\ \ D_{tn} = 0$

end

Algorithm 1: Evaluation of tractions and derivatives of tractions for analytical implementation.

As stated at the end of previous chapter, Minkowski version of TSLs are used for implementation. An initial elastic part should be added to make the model intrinsic. Elastic part is defined linearly with slope $E_{n/t}$, and it is defined until a critical separation $\delta_{n/t,cr}$ where maximum tractions in (3.11)(3.12) are reached. Then, tractions become,

$$\begin{aligned} T_n(\delta_n) =& E_n\delta_n, \ \text{if}\ \ \delta_n \leq \delta_{n,cr} \\ T_n(f) =& \sigma_y\left((1-f)^2 + \left(\frac{1}{\sqrt{3}}ln\frac{1}{f}\right)^2\right)^{\frac{1}{2}} \ \text{if}\ \ \delta_n > \delta_{n,cr},\ f = \frac{\delta_n - \delta_{n,cr} + h_0 f_0}{\delta_n - \delta_{n,cr} + h_0} \end{aligned} \tag{3.13}$$

$$\begin{aligned} T_t(\delta_t) =& E_t\delta_t, \ \text{if}\ \ \delta_t \leq \delta_{t,cr} \\ T_t(f) =& \frac{\sigma_y}{\sqrt{3}}(1-f) \ \text{if}\ \ \delta_t > \delta_{t,cr},\ f = \left(\sqrt{f_0} + \frac{\delta_t - \delta_{t,cr}}{l}\right)^2 \end{aligned} \tag{3.14}$$

Original tractions are slided by $\delta_{n/t,cr}$ in the separation axis simply by modifying f. If $E_{n/t}$ is specified, $\delta_{n/t,cr}$ can be found as,

$$\delta_{n,cr} = \frac{T_{n,max}}{E_n}, \quad \delta_{t,cr} = \frac{T_{t,max}}{E_t} \tag{3.15}$$

And maximum tractions are obtained by setting $\delta_{n/t} = 0$ in (3.11)(3.12),

$$T_{n,max} = \sigma_y \left[(1-f_0)^2 + \left(\frac{1}{\sqrt{3}} ln \frac{1}{f_0} \right)^2 \right]^{\frac{1}{2}} \quad \text{and} \quad T_{t,max} = \frac{\sigma_y}{\sqrt{3}} [1-f_0] \tag{3.16}$$

The derivatives of tractions with respect to separations are needed for the Jacobian in a finite element framework. Simply take derivative of (3.13) and (3.14).

$$\begin{aligned}
\frac{\partial T_n}{\partial \delta_n} =& E_n, \text{ if } \delta_n \leq \delta_{n,cr} \qquad (3.17)\\
\frac{\partial T_n}{\partial \delta_n} =& \frac{\partial T_n}{\partial f} \frac{\partial f}{\partial \delta_n} = \frac{\sigma_y}{2} \left[(1-f)^2 + \frac{1}{3}(lnf)^2 \right]^{-1/2} \left[2(1-f)(-1) + \frac{2}{3} \frac{lnf}{f} \right] ...\\
& ... \left[\frac{1-f}{h} \right] \text{ if } \delta_n > \delta_{n,cr}\\
\frac{\partial T_n}{\partial \delta_t} =& 0\\
\frac{\partial T_t}{\partial \delta_t} =& E_t, \text{ if } \delta_t \leq \delta_{t,cr} \qquad (3.18)\\
\frac{\partial T_t}{\partial \delta_t} =& \frac{\partial T_t}{\partial f} \frac{\partial f}{\partial \delta_t} = \left[\frac{-\sigma_y}{\sqrt{3}} \right] \left[\frac{2\sqrt{f}}{l} \right] \text{ if } \delta_t > \delta_{t,cr}\\
\frac{\partial T_t}{\partial \delta_n} =& 0
\end{aligned}$$

Note that the derivatives $\partial f / \partial \delta_{n/t}$ are obtained from the evolution equations for mode-I and mode-II, where,

$$df = \frac{d\delta_n}{h}(1-f), \quad \frac{df}{d\delta_n} = \frac{1-f}{h} \text{ for pure mode-I} \tag{3.19}$$

$$df = 2\sqrt{f}\frac{d\delta_t}{l}, \quad \frac{df}{d\delta_t} = \frac{2\sqrt{f}}{l} \text{ for pure mode-II} \tag{3.20}$$

The unloading/reloading relationship is linear towards the origin (see Fig.3.3). There are two main choices here. Unloading can be towards the origin, or it can be with an initial elastic slope similar to plasticity. The latter is suggested for ductile materials, while the former is suggested for brittle ones [96]. However, the former is used in early ductile models because unloading relations do not have a considerable effect

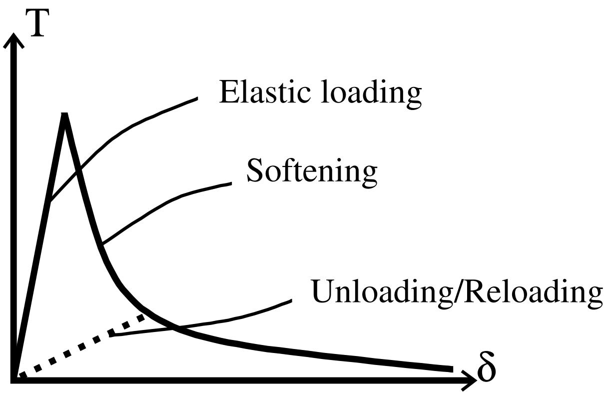

Figure 3.3: Regions of traction-separation law.

under monotonic loading. They become important when fatigue failure is modelled, where cyclic loading is the main driving force. Our numerical examples are also for monotonic loading, so unloading is taken towards the origin due its convenience.

In the implementation, the maximum separation reached is saved separately for mode-I and mode-II as $\delta_{n,max}$ and $\delta_{t,max}$ respectively. When, $\delta < \delta_{max}$, unloading is initiated, and f_{max} is calculated at δ_{max}, which can be used to calculate traction at δ_{max}. Then, it is multiplied with a factor $\delta_{n,t}/\delta_{max}$ to have linear unloading towards origin, i.e.

$$T_{n,t} = T_{n,t}(f_{max})\frac{\delta_{n,t}}{\delta_{max}} \text{ if } \delta < \delta_{max} \text{ (Unloading/reloading)} \tag{3.21}$$

, and derivative is simply,

$$\frac{\partial T_{n,t}}{\partial \delta} = T_{n,t}(f_{max})\frac{1}{\delta_{max}} \tag{3.22}$$

For contact condition in the normal direction, $\delta_n < 0$, a penalty stiffness is used, which is taken equal to the elastic slope here. As the material self penetrates, traction keeps increasing following penalty stiffness times separation, in a way to hinder penetration.

$$T_n = E_n \delta_n \text{ if } \delta_n < 0 \text{ (Contact)} \tag{3.23}$$

For pure mode analytical implementation, failure is defined only for mode-II. Mode-I behaves exponentially, approaching zero traction at infinite separation. For failure, a final separation $\delta_{t,final}$ is calculated, after which tractions and derivatives of tractions become zero. It can be calculated from (3.12), by setting traction T_t to zero and finding δ_t.

$$\delta_{t,final} = l(1 - f_0), \tag{3.24}$$

$$T_t = 0 \text{ and } \frac{\partial T_t}{\partial \delta_{t/n}} = 0 \text{ if } \delta_t \geqslant \delta_{t,final} \text{ (Failure)}. \tag{3.25}$$

Some numerical simulations are conducted in Abaqus to test the developed UEL subroutine. A simple model is created, including two bulk elements and one cohesive element in between. It is tested for pure mode-I and mode-II cases. Contact, loading, unloading/reloading and failure responses are obtained. Loading histories are represented in Figs. 3.4 and 3.6, and different conditions are numbered in the Figs. 3.5 and 3.7.

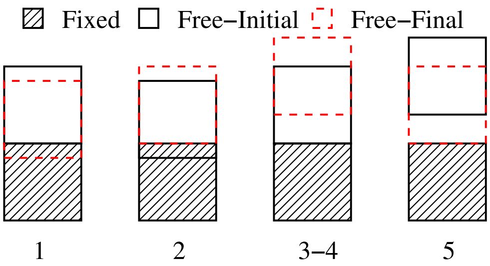

Figure 3.4: Mode-I loading history.

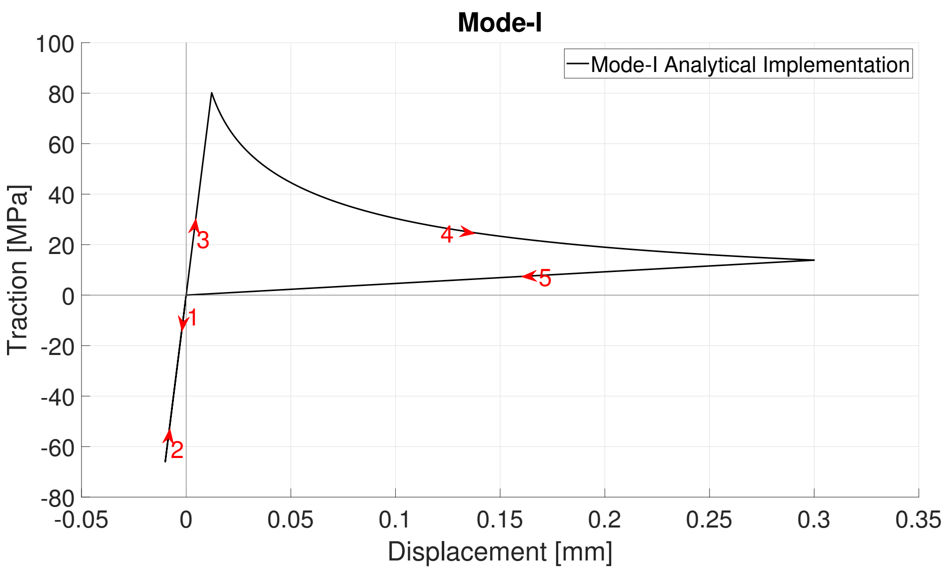

Figure 3.5: Traction versus displacement response to mode-I loading/unloading.

In Fig. 3.5, element is under mode-I loading. First, it is compressed, making it self-penetrate (1), and then unloaded to initial position (2). It is then put under tension where the elastic (3) and softening (4) regions can be seen. Finally, it is unloaded to the initial position where force goes back to zero as expected (5).

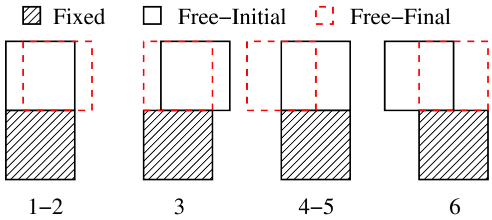

Figure 3.6: Mode-II loading history.

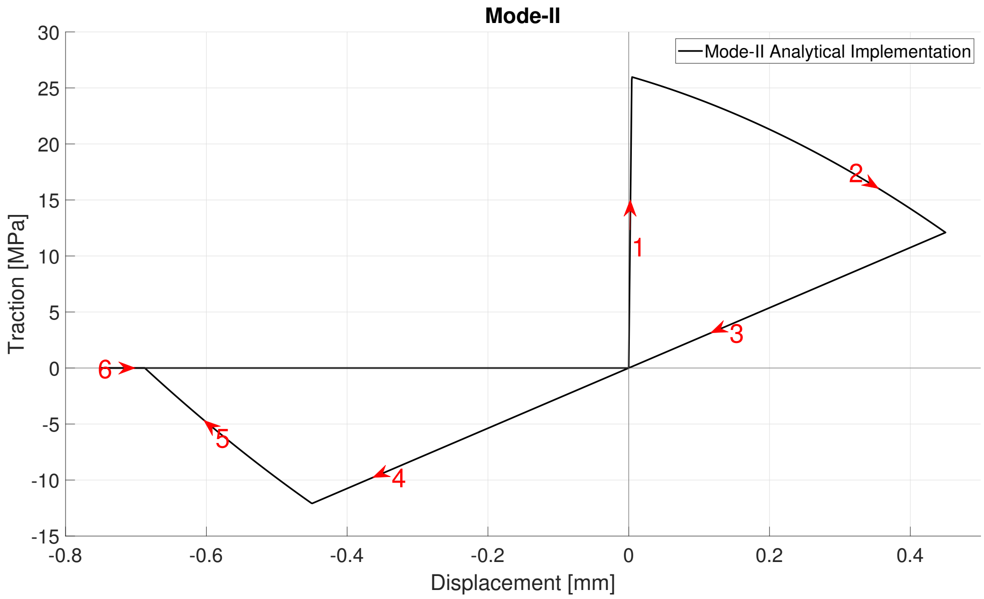

Figure 3.7: Traction versus displacement response to mode-II loading/unloading.

In Fig. 3.7, element is under mode-II loading. First, it is sheared to the right side, and elastic (1) and softening (2) response are observed. Then it is unloaded (3) and sheared to the other side. First, there is reloading (4) response, then the softening continues from where it was left on the other side and fails (5). Finally, it is unloaded to the initial position (6).

The results are as expected for pure mode analytical implementation. Next, incremental implementation of tractions is explained, which is a stepping stone towards mixed-mode implementation.

3.3 Mode I-II incremental implementation

In the previous section, evolution of pore fraction, df, and pore height, dh, were expressed separately for mode-I and mode-II, which allowed us to take their integrals, and express f and h as a function of δ_n and δ_t. This is not possible for mixed-mode evolution equations (2.15). Therefore, instead of obtaining T_n and T_t directly as a function of δ_n and δ_t by taking integral of df and dh, pore fraction f and pore height h are incrementally updated, and the tractions are written as a function of f and h. This allows us to update f using both δ_n and δ_t, which is required for mixed-mode implementation. The evolution of f and h are known from equation (2.15) for mixed mode. These relations are approximated with a backward Euler scheme, first for uncoupled pure mode-I and mode-II. Then, the relations for updating f and h are found for mixed-mode. This implementation is tested with the one element model and compared with uncoupled implementation.

For pure mode-I, we have,

$$\begin{aligned} df &= \frac{d\delta_n}{h}(1-f) \\ dh &= d\delta_n \end{aligned} \tag{3.26}$$

Using backward Euler scheme,

$$\begin{aligned} f_{n+1} - f_n &= \frac{\Delta\delta_n}{h_{n+1}}(1-f_{n+1}) \\ h_{n+1} - h_n &= \Delta\delta_n \end{aligned} \tag{3.27}$$

Hence,

$$\begin{aligned} f_{n+1} &= \frac{f_n + \frac{\Delta\delta_n}{h_{n+1}}}{1 + \frac{\Delta\delta_n}{h_{n+1}}} \\ h_{n+1} &= h_n + \Delta\delta_n \end{aligned} \tag{3.28}$$

For pure mode-II, we have,

$$\begin{aligned} df &= 2\sqrt{f}\frac{d\delta_t}{l} \\ dh &= -\frac{h}{a}d\delta_t \end{aligned} \tag{3.29}$$

Using backward Euler scheme,

$$f_{n+1} - f_n = 2\sqrt{f_{n+1}}\frac{\Delta\delta_t}{l}$$

$$h_{n+1} - h_n = -\frac{h_{n+1}}{a}\Delta\delta_t \text{ where } a = \sqrt{f_0}l \tag{3.30}$$

After some manipulation,

$$f_{n+1} = \left(\sqrt{f_n + \frac{\Delta\delta_t^2}{l^2}} + \frac{\Delta\delta_t}{l}\right)^2$$

$$h_{n+1} = \frac{h_n}{1 + \frac{\Delta\delta_t}{\sqrt{f_0}l}} \tag{3.31}$$

Rewriting equation (2.15) for mixed-mode,

$$df = \frac{d\delta_n}{h}(1-f) + 2\sqrt{f}\frac{d\delta_t}{l}$$

$$dh = d\delta_n - \frac{h}{a}d\delta_t \tag{3.32}$$

Using backward Euler scheme,

$$f_{n+1} - f_n = \frac{\Delta\delta_n}{h_{n+1}}(1 - f_{n+1}) + 2\sqrt{f_{n+1}}\frac{\Delta\delta_t}{l} \tag{3.33}$$

$$h_{n+1} - h_n = \Delta\delta_n - \frac{h_{n+1}}{a}\Delta\delta_t \text{ where } a = \sqrt{f_0}l \tag{3.34}$$

After some manipulation,

$$f_{n+1} = \frac{\left(\frac{\Delta\delta_t}{l} + \sqrt{\frac{(\Delta\delta_t)^2}{l^2} + \frac{(\Delta\delta_n)^2}{h_{n+1}^2} + f_n + \frac{\Delta\delta_n}{h_{n+1}}(f_n+1)}\right)^2}{\left(1 + \frac{\Delta\delta_n}{h_{n+1}}\right)^2} \tag{3.35}$$

$$h_{n+1} = \frac{h_n + \Delta\delta_n}{1 + \frac{\Delta\delta_t}{\sqrt{f_0}l}} \tag{3.36}$$

As a confirmation, by setting $\Delta\delta_t = 0$ or $\Delta\delta_n = 0$ in (3.35) and (3.36) pure mode update equations (3.28) and (3.31) are obtained respectively.

Tractions and derivatives are the same as analytical implementation. In addition, there are cross derivatives,

$$\frac{\partial T_n}{\partial \delta_t} = \frac{\partial T_n}{\partial f}\frac{\partial f}{\partial \delta_t} = \frac{\sigma_y}{2}\left[(1-f)^2 + \frac{1}{3}(lnf)^2\right]^{-1/2}\left[2(1-f)(-1) + \frac{2}{3}\frac{lnf}{f}\right]\left[\frac{2\sqrt{f}}{l}\right]$$

$$\frac{\partial T_t}{\partial \delta_n} = \frac{\partial T_t}{\partial f}\frac{\partial f}{\partial \delta_n} = \left[\frac{-\sigma_y}{\sqrt{3}}\right]\left[\frac{1-f}{h}\right] \tag{3.37}$$

Contact and unloading relations are the same. However, failure is determined by checking if $f \geqslant 1$, and both tractions become zero in case of failure. Considering these changes, Algorithm 1 is slightly modified as follows for incremental implementation,

–Normal cohesive interaction:

if $\delta_n < 0$ *(Contact)* **then**
$\quad T_n = D_{nn}\delta_n, \;\; D_{nn} = E_n, \;\; D_{nt} = 0$

else if $\delta_n \geqslant \delta_{n,max}$ *and* $\delta_n \leqslant \delta_{n,cr}$ *and* $f < 1$ *(Loading-Elastic)* **then**
$\quad T_n = D_{nn}\delta_n, \;\; D_{nn} = E_n, \;\; D_{nt} = 0$

else if $\delta_n \geqslant \delta_{n,max}$ *and* $\delta_n > \delta_{n,cr}$ *and* $f < 1$ *(Loading-Softening)* **then**
$\quad h_{i+1} = h(h_i, \Delta\delta_n, \Delta\delta_t), \;\; f_{i+1} = f(h_i, f_i, \Delta\delta_n, \Delta\delta_t)$
$\quad T_n = T_n(f_{i+1}), \;\; D_{nn} = \frac{\partial T_n}{\partial f}\frac{\partial f}{\partial \delta_n}, \;\; D_{nt} = \frac{\partial T_n}{\partial f}\frac{\partial f}{\partial \delta_t}$

else if $\delta_n < \delta_{n,max}$ *and* $f < 1$ *(Unloading/reloading)* **then**
$\quad T_n = T_n(f_{max})\frac{\delta_n}{\delta_{n,max}}, \;\; D_{nn} = T_n(f_{max})\frac{1}{\delta_{n,max}}, \;\; D_{nt} = 0$

end

–Tangential cohesive interaction:

if $|\delta_t| \geqslant \delta_{t,max}$ *and* $|\delta_t| \leqslant \delta_{t,cr}$ *and* $f < 1$ *(Loading-Elastic)* **then**
$\quad T_t = D_{tt}|\delta_t|sign(\delta_t), \;\; D_{tt} = E_t, \;\; D_{tn} = 0$

else if $|\delta_t| \geqslant \delta_{t,max}$ *and* $|\delta_t| > \delta_{t,cr}$ *and* $f < 1$ *(Loading-Softening)* **then**
$\quad h_{i+1} = h(h_i, \Delta\delta_n, \Delta\delta_t), \;\; f_{i+1} = f(h_i, f_i, \Delta\delta_n, \Delta\delta_t)$
$\quad T_t = T_t(f_{i+1})sign(\delta_t), \;\; D_{tt} = \frac{\partial T_t}{\partial f}\frac{\partial f}{\partial \delta_t}, \;\; D_{tn} = \frac{\partial T_t}{\partial f}\frac{\partial f}{\partial \delta_n}$

else if $|\delta_t| < \delta_{t,max}$ *and* $f < 1$ *(Unloading/reloading)* **then**
$\quad T_t = T_t(f_{max})sign(\delta_t)\frac{|\delta_t|}{\delta_{t,max}}, \;\; D_{tt} = T_t(f_{max})\frac{1}{\delta_{t,max}}, \;\; D_{tn} = 0$

end

–Failure check:

if $f \geqslant 1$ *(Failure)* **then**
$\quad T_t = 0, T_n = 0 \;\; D_{tt} = 0, D_{tn} = 0, D_{nt} = 0, D_{nn} = 0$

end

Algorithm 2: Evaluation of tractions and derivatives of tractions for incremental implementation.

Same as before, derivatives of f are found from,

$$\begin{aligned} df =& \frac{d\delta_n}{h}(1-f) + 2\sqrt{f}\frac{d\delta_t}{l} \quad \text{for mixed-mode} \\ \frac{df}{d\delta_n} =& \frac{1-f}{h}, \;\; \frac{df}{d\delta_t} = \frac{2\sqrt{f}}{l} \end{aligned} \tag{3.38}$$

In the incremental UEL implementation, in addition to maximum separations $\delta_{n/t,max}$, pore height h and pore fraction f are saved at the end of each increment as state variables.

In Figs. (3.8) and (3.9), the same numerical simulations for the previous analytical model are done with the incremental model. It is confirmed that the results are the same, and the incremental model can be extended to mixed mode.

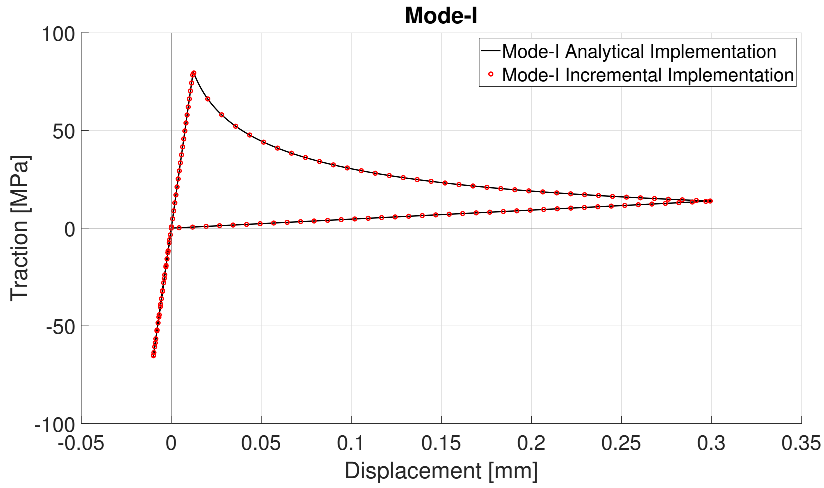

Figure 3.8: Traction versus displacement response to mode-I loading/unloading for incremental and analytical model.

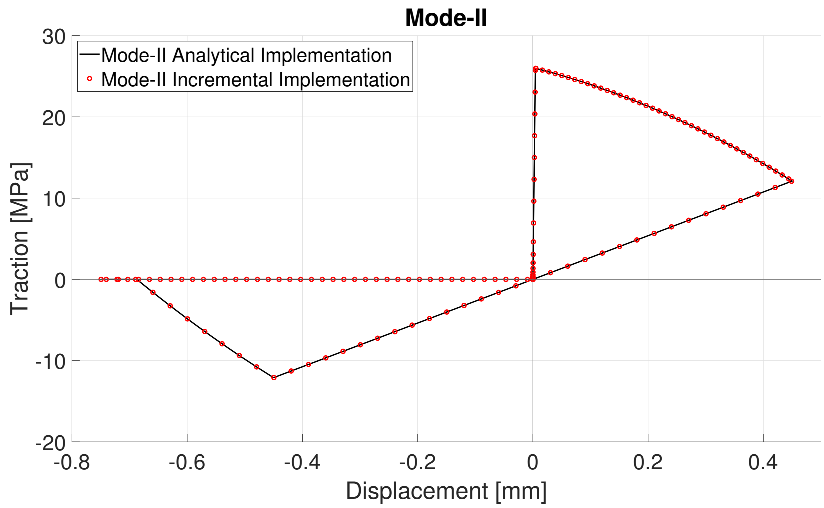

Figure 3.9: Traction versus displacement response to mode-II loading/unloading for incremental and analytical model.

3.4 Mixed-mode implementation scheme

In the mixed-mode derivation, a yield function as a function of tractions and pore fraction, f, was obtained, see equation (3.39), where f is a function of pore height, h, and separations. Evolution of h is also controlled by separations, $\delta_{n,t}$. Ultimately, our yield function is a function of tractions, T_n, T_t, and separations, δ_n, δ_t, see below.

$$g = \left[\frac{T_n^2}{(1-f)^2 + \left(\frac{1}{\sqrt{3}} ln \frac{1}{f} \right)^2} + \frac{3T_t^2}{(1-f)^2} \right]^{\frac{1}{2}} - \sigma_y = \overline{\sigma} - \sigma_y \tag{3.39}$$

$$\begin{aligned} df &= \frac{d\delta_n}{h}(1-f) + 2\sqrt{f}\frac{d\delta_t}{l} \\ dh &= d\delta_n - \frac{h}{a} d\delta_t \end{aligned} \tag{3.40}$$

Obviously, there is not an explicit form for the tractions, and they cannot be readily calculated. Therefore, to calculate the change of tractions resulting from a given change in separations, a numerical integration scheme for coupled elastoplastic and damage equations is employed [97]. It's general formulation is explained in the following subsection, which is then applied to the derived cohesive zone model. Yield functions of the derived cohesive zone model are used with this integration scheme to solve for tractions.

3.4.1 Numerical integration scheme for coupled elastoplastic and damage equations

In this section a generic implicit numerical integration scheme is addressed for a class of constitutive laws where, the yield function is given by,

$$F = \overline{\sigma}(\sigma_{ij}, \varepsilon_{ij}^p) - \sigma_y = 0. \tag{3.41}$$

and then applied to the yield type of mixed-mode traction separation relation to get the incremental update of tractions.

Assume that total strain is additively decomposed into elastic and plastic components,

$$\varepsilon_{ij} = \varepsilon_{ij}^e + \varepsilon_{ij}^p. \tag{3.42}$$

An increment of plastic strain $d\varepsilon_{ij}^p$ is allowed only if equation (3.41) is satisfied, meaning the stress state is on the yield surface. The direction of the plastic strain increment is given by the following flow rule,

$$d\varepsilon_{ij}^p = d\mu \frac{\partial F}{\partial \sigma_{ij}} = d\mu \frac{\partial \overline{\sigma}}{\partial \sigma_{ij}} \tag{3.43}$$

where $d\mu$ is the plastic multiplier. Or, we may write,

$$d\varepsilon_{ij}^p = d\mu \; g_{ij} \;\; \text{where} \;\; g_{ij} = \frac{\partial \overline{\sigma}}{\partial \sigma_{ij}}. \tag{3.44}$$

If $F < 0$, material response is elastic,

$$d\sigma_{ij} = D_{ijkl} d\varepsilon_{kl}^e = D_{ijkl} d\varepsilon_{kl} \tag{3.45}$$

where D_{ijkl} is a fourth order stiffness tensor.

In the context of an incremental numerical scheme, consider the case where the stress σ_{ij}, the total strain ε_{ij}, and the accumulated plastic strain ε_{ij}^p are known up to the current increment. In the current increment, the total strain increment $\Delta\varepsilon_{ij}$ is provided, and $\Delta\sigma_{ij}$ need to be found.

Again, If $F < 0$, response is elastic and simply,

$$\Delta\sigma_{ij} = D_{ijkl} \Delta\varepsilon_{kl}^e = D_{ijkl} \Delta\varepsilon_{kl}. \tag{3.46}$$

If $F \geq 0$, following implicit integration scheme is employed,

At the end of the current increment the stress state must be on the yield surface. Thus,

$$F = \overline{\sigma}(\sigma_{ij} + \Delta\sigma_{ij}, \varepsilon_{ij}^p + \Delta\varepsilon_{ij}^p) - \sigma_y = 0. \tag{3.47}$$

The direction of the plastic strain increment at the point $(\sigma_{ij} + \theta\Delta\sigma_{ij}, \varepsilon_{ij}^p + \theta\Delta\varepsilon_{ij}^p)$ is found, where $0 \leq \theta \leq 1$. A value in the range 0.5 to 1 ensures that the solution is unconditionally stable. Equation 3.44 gives,

$$G_{ij} = \Delta\varepsilon_{ij}^p - \Delta\mu \; g_{ij}(\sigma_{ij} + \Delta\sigma_{ij}, \varepsilon_{ij}^p + \Delta\varepsilon_{ij}^p) = 0. \tag{3.48}$$

Finally, the stress and strain increments must satisfy the elastic constitutive law,

$$H_{ij} = \sigma_{ij} + \Delta\sigma_{ij} - D_{ijkl}(\varepsilon^*_{kl} - \Delta\varepsilon^p_{ij}) = 0 \tag{3.49}$$

where

$$\varepsilon^*_{ij} = \varepsilon_{ij} + \Delta\varepsilon_{ij} - \varepsilon^p_{ij}. \tag{3.50}$$

If it is assumed that the elastic stiffness matrix is not a function of inelastic strain, then,

$$H_{ij} = \Delta\sigma_{ij} - D_{ijkl}(\Delta\varepsilon_{ij} - \Delta\varepsilon^p_{ij}) = 0. \tag{3.51}$$

Equations 3.47, 3.48 and 3.51 represent a set of 13 nonlinear equations and 13 unknowns ($\Delta\sigma_{ij}, \Delta\varepsilon^p_{ij}$ and $\Delta\mu$). This system of nonlinear equations can be solved by using Newton's method. After i iterations, the values of $(\Delta\sigma_{ij}, \Delta\varepsilon^p_{ij}\text{and}\Delta\mu)^i$ are given by,

$$\begin{bmatrix} \Delta\varepsilon^p_{kl} \\ \Delta\sigma_{kl} \\ \Delta\mu \end{bmatrix}_i = \begin{bmatrix} \Delta\varepsilon^p_{kl} \\ \Delta\sigma_{kl} \\ \Delta\mu \end{bmatrix}_{i-1} - \begin{bmatrix} \delta_{ik}\delta_{jl} - \theta\Delta\mu\dfrac{\partial g_{ij}}{\partial\varepsilon^p_{kl}} & -\theta\Delta\mu\dfrac{g_{ij}}{\partial\sigma_{kl}} & -g_{ij} \\ D_{ijkl} & \delta_{ik}\delta_{jl} & 0 \\ \dfrac{\partial\overline{\sigma}}{\partial\varepsilon^p_{kl}} & \dfrac{\partial\overline{\sigma}}{\partial\sigma_{kl}} & 0 \end{bmatrix}^{-1}_{i-1} \begin{bmatrix} G_{ij} \\ H_{ij} \\ F \end{bmatrix}_{i-1}$$

where subscript $i-1$ indicates that calculations are done using values obtained at the end of the previous increment. Iteration is continued until a small enough tolerance for G_{ij}, H_{ij} and F is reached.

In a finite element framework, we also need the Jacobian,

$$J_{ijkl} = \frac{\partial\Delta\sigma_{ij}}{\partial\Delta\varepsilon_{kl}} \tag{3.52}$$

It can be determined directly by noting that ($\Delta\sigma_{ij}, \Delta\varepsilon^p_{ij}$ and $\Delta\mu$) are functions of the total strain increment $\Delta\varepsilon_{ij}$. Taking derivative of equations 3.47, 3.48 and 3.51 with respect to $\Delta\varepsilon_{ij}$ then gives,

$$\begin{bmatrix} \delta_{ik}\delta_{jl} - \theta\Delta\mu\dfrac{\partial g_{ij}}{\partial\varepsilon^p_{kl}} & -\theta\Delta\mu\dfrac{g_{ij}}{\partial\sigma_{kl}} & -g_{ij} \\ D_{ijkl} & \delta_{ik}\delta_{jl} & 0 \\ \dfrac{\partial\overline{\sigma}}{\partial\varepsilon^p_{kl}} & \dfrac{\partial\overline{\sigma}}{\partial\sigma_{kl}} & 0 \end{bmatrix} \begin{bmatrix} \dfrac{\partial\Delta\varepsilon^p_{kl}}{\partial\Delta\varepsilon_{mn}} \\ J_{klmn} \\ \dfrac{\partial\Delta\mu}{\partial\Delta\varepsilon_{mn}} \end{bmatrix} = \begin{bmatrix} 0 \\ D_{ijmn} \\ 0 \end{bmatrix}$$

For the Jacobian, all quantities within the matrices are determined by using the values at the end of the final iteration for the determination of the stress increment.

This was the general formulation of the implicit numerical integration scheme. In order to apply it to the derived cohesive zone model, following changes are made. Strain tensor, ε_{ij}, is replaced by separations δ_n and δ_t, and separations are additively decomposed into elastic and plastic parts, i.e. $\delta = \delta^e + \delta^p$. Stress tensor, σ_{ij}, is replaced by tractions T_n and T_t. Fourth order stiffness tensor, D_{ijkl}, is replaced by elastic slopes E_n and E_t. Before the implicit numerical integration scheme is applied for our cohesive zone model, there are a few things to consider. f and h are updated incrementally considering contributions from both modes. When updating f and h there are some points taken into account,

1) f and h are updated only if the material is at the softening region of the traction-separation law (see Fig. 3.3), i.e. if the loading is plastic, yield function $F \geq 0$. This is achieved by updating f and h using plastic separations, δ_n^p and δ_t^p, instead of total separations δ_n and δ_t.
2) f and h are not updated if the material is under unloading/reloading/contact for that mode. For example, if the material is loaded in mode-I, but unloading in mode-II, f and h are updated as it is pure mode-I.
3) If the material is under loading, f and h are not updated if the loading is elastic.
4) Element fails when $f = 1$.
5) Elastic slopes should be as high as possible to have convergence and an accurate solution.

First, mode-I and mode-II are considered. These pure mode versions will be used for the unloading/reloading cases in mixed-mode.

3.4.2 Mode I using plasticity formulation

In this subsection, the generic iteration scheme explained previously is applied for mode-I loading case, and the system of equations is derived. Equations to be satisfied in the next increment,

$$F = \overline{\sigma} - \sigma_y = 0 \tag{3.53}$$

$$G_n = \Delta\delta_n^p - \Delta\mu\frac{\partial\overline{\sigma}}{\partial T_n} = 0 \tag{3.54}$$

$$H_n = T_n + \Delta T_n - E_n(\delta_n + \Delta\delta_n - \delta_n^p - \Delta\delta_n^p) = 0 \tag{3.55}$$

Unknowns: $\Delta\delta_n^p$, ΔT_n, $\Delta\mu$ where $\overline{\sigma} := \overline{\sigma}(\delta_n^p, T_n)$

Use Newton-Raphson's algorithm,

$$\mathbf{X}^n = \mathbf{X}^{n-1} - \left(\frac{\partial\mathbf{f}}{\partial\mathbf{X}^{n-1}}\right)^{-1}\mathbf{f}(\mathbf{X}^{n-1}) \tag{3.56}$$

Then,

$$\begin{bmatrix}\Delta\delta_n^p \\ \Delta T_n \\ \Delta\mu\end{bmatrix}_n = \begin{bmatrix}\Delta\delta_n^p \\ \Delta T_n \\ \Delta\mu\end{bmatrix}_{n-1} - \begin{bmatrix}\dfrac{\partial G_n}{\partial\delta_n^p} & \dfrac{\partial G_n}{\partial T_n} & \dfrac{\partial G_n}{\partial\mu} \\ \dfrac{\partial H_n}{\partial\delta_n^p} & \dfrac{\partial H_n}{\partial T_n} & \dfrac{\partial H_n}{\partial\mu} \\ \dfrac{\partial F}{\partial\delta_n^p} & \dfrac{\partial F}{\partial T_n} & \dfrac{\partial F}{\partial\mu}\end{bmatrix}_{n-1}^{-1} \begin{bmatrix}G_n \\ H_n \\ F\end{bmatrix}_{n-1}$$

Derivatives are given by,

$$\frac{\partial G_n}{\partial\delta_n^p} = 1 - \Delta\mu\frac{\partial\left(\frac{\partial\overline{\sigma}}{\partial T_n}\right)}{\partial\delta_n^p}, \quad \frac{\partial G_n}{\partial T_n} = -\Delta\mu\frac{\partial^2\overline{\sigma}}{\partial T_n^2}, \quad \frac{\partial G_n}{\partial\mu} = -\frac{\partial\overline{\sigma}}{\partial T_n} \tag{3.57}$$

$$\frac{\partial H_n}{\partial\delta_n^p} = E_n, \quad \frac{\partial H_n}{\partial T_n} = sign(T_n), \quad \frac{\partial H_n}{\partial\mu} = 0 \tag{3.58}$$

$$\frac{\partial F}{\partial\delta_n^p} = \frac{\partial\overline{\sigma}}{\partial\delta_n^p}, \quad \frac{\partial F}{\partial T_n} = \frac{\partial\overline{\sigma}}{\partial T_n}, \quad \frac{\partial F}{\partial\mu} = 0 \tag{3.59}$$

Letting $\dfrac{\partial\overline{\sigma}}{\partial T_n} = g_n$, we have,

$$\begin{bmatrix}\Delta\delta_n^p \\ \Delta T_n \\ \Delta\mu\end{bmatrix}_n = \begin{bmatrix}\Delta\delta_n^p \\ \Delta T_n \\ \Delta\mu\end{bmatrix}_{n-1} - \begin{bmatrix}1 - \Delta\mu\dfrac{\partial g_n}{\partial\delta_n^p} & -\Delta\mu\dfrac{\partial g_n}{\partial T_n} & -g_n \\ E_n & sign(T_n) & 0 \\ \dfrac{\partial\overline{\sigma}}{\partial\delta_n^p} & g_n & 0\end{bmatrix}_{n-1}^{-1} \begin{bmatrix}G_n \\ H_n \\ F\end{bmatrix}_{n-1}$$

$$\overline{\sigma} = \left[\frac{T_n^2}{(1-f)^2 + (lnf)^2/3}\right]^{\frac{1}{2}} = \frac{|T_n|}{[(1-f)^2 + (lnf)^{2/3}]^{\frac{1}{2}}} \tag{3.60}$$

$$df = d\delta_n^p \frac{(1-f)}{h} \tag{3.61}$$

$$dh = d\delta_n^p \tag{3.62}$$

$$d\delta_n = d\delta_n^e + d\delta_n^p \tag{3.63}$$

Evolution of f and h was found in (3.28), but here δ_n^p is used.

$$f_{n+1} = \frac{f_n + \dfrac{\Delta\delta_n^p}{h_{n+1}}}{1 + \dfrac{\Delta\delta_n^p}{h_{n+1}}} \tag{3.64}$$

$$h_{n+1} = h_n + \Delta\delta_n^p \tag{3.65}$$

Derivatives,

$$g_n = \frac{\partial\overline{\sigma}}{\partial T_n} = \frac{T_n}{\overline{\sigma}[(1-f)^2 + (lnf)^2/3]} \tag{3.66}$$

$$\frac{\partial g_n}{\partial T_n} = \frac{(\overline{\sigma} - T_n g_n)}{\overline{\sigma}^2[(1-f)^2 + (lnf)^2/3]} \tag{3.67}$$

$$\frac{\partial\overline{\sigma}}{\partial f} = \frac{1}{2\overline{\sigma}}\left[\frac{-T_n^2[-2(1-f) + \frac{2}{3}lnf\frac{1}{f}]}{[(1-f)^2 + (lnf)^2/3]^2}\right] \tag{3.68}$$

$$\frac{\partial g_n}{\partial f} = \frac{-T_n}{\overline{\sigma}^2}\left[\frac{\frac{\partial\overline{\sigma}}{\partial f}[(1-f)^2 + (lnf)^2/3] + \overline{\sigma}[-2(1-f) + \frac{2}{3}lnf\frac{1}{f}]}{[(1-f)^2 + (lnf)^2/3]^2}\right] \tag{3.69}$$

$$\frac{\partial g_n}{\partial\delta_n^p} = \frac{\partial g_n}{\partial f}\frac{\partial f}{\partial\delta_n^p} = \frac{\partial g_n}{\partial f}\frac{(1-f)}{h} \tag{3.70}$$

$$\frac{\partial\overline{\sigma}}{\partial\delta_n^p} = \frac{\partial\overline{\sigma}}{\partial f}\frac{\partial f}{\partial\delta_n^p} = \frac{\partial\overline{\sigma}}{\partial f}\frac{(1-f)}{h} \tag{3.71}$$

Following the steps in section 3.4.1, the derivative $\partial T_n/\partial\delta_n$ for the Jacobian can be found. Take derivative of (3.55) and (3.53) with respect to δ_n. We get,

$$\frac{\partial H_n}{\partial\delta_n} = \frac{\partial T_n}{\partial\delta_n} - E_n + E_n\frac{\partial\delta_n^p}{\partial\delta_n} = 0 \tag{3.72}$$

$$\frac{\partial F}{\partial\delta_n} = \frac{\partial\overline{\sigma}}{\partial\delta_n^p}\frac{\partial\delta_n^p}{\partial\delta_n} + \frac{\partial\overline{\sigma}}{\partial T_n}\frac{\partial T_n}{\partial\delta_n} = 0 \tag{3.73}$$

Here, there are two unknowns, $\frac{\partial T_n}{\partial \delta_n}$ and $\frac{\partial \delta_n^p}{\partial \delta_n}$, and two equations. Solving the system, we find,

$$\frac{\partial T_n}{\partial \delta_n} = \frac{-\frac{\partial \overline{\sigma}}{\partial \delta_n^p}}{g_n - \frac{\partial \overline{\sigma}}{\partial \delta_n^p}\frac{1}{E_n}} \tag{3.74}$$

3.4.3 Mode II using plasticity formulation

In this subsection, the formulation used for mode-I loading in previous subsection is repeated for mode-II loading. Equations to be satisfied in the next increment,

$$F = \overline{\sigma} - \sigma_y = 0 \tag{3.75}$$

$$G_t = \Delta\delta_t^p - \Delta\mu\frac{\partial \overline{\sigma}}{\partial T_t} = 0 \tag{3.76}$$

$$H_t = T_t + \Delta T_t - E_t(|\delta_t + \Delta\delta_t| - \delta_t^p - \Delta\delta_t^p) = 0 \tag{3.77}$$

Unknowns: $\Delta\delta_t^p$, ΔT_t, $\Delta\mu$ where $\overline{\sigma} := \overline{\sigma}(\delta_t^p, T_t)$

Use Newton-Raphson's algorithm,

$$\begin{bmatrix} \Delta\delta_t^p \\ \Delta T_t \\ \Delta\mu \end{bmatrix}_n = \begin{bmatrix} \Delta\delta_t^p \\ \Delta T_t \\ \Delta\mu \end{bmatrix}_{n-1} - \begin{bmatrix} \frac{\partial G_t}{\partial \delta_t^p} & \frac{\partial G_t}{\partial T_t} & \frac{\partial G_t}{\partial \mu} \\ \frac{\partial H_t}{\partial \delta_t^p} & \frac{\partial H_t}{\partial T_t} & \frac{\partial H_t}{\partial \mu} \\ \frac{\partial F}{\partial \delta_t^p} & \frac{\partial F}{\partial T_t} & \frac{\partial F}{\partial \mu} \end{bmatrix}_{n-1}^{-1} \begin{bmatrix} G_t \\ H_t \\ F \end{bmatrix}_{n-1}$$

Derivatives are given by,

$$\frac{\partial G_t}{\partial \delta_t^p} = 1 - \Delta\mu\frac{\partial\left(\frac{\partial \overline{\sigma}}{\partial T_t}\right)}{\partial \delta_t^p}, \quad \frac{\partial G_t}{\partial T_t} = -\Delta\mu\frac{\partial^2 \overline{\sigma}}{\partial T_t^2}, \quad \frac{\partial G_t}{\partial \mu} = -\frac{\partial \overline{\sigma}}{\partial T_t} \tag{3.78}$$

$$\frac{\partial H_t}{\partial \delta_t^p} = E_t, \quad \frac{\partial H_t}{\partial T_t} = sign(T_t), \quad \frac{\partial H_t}{\partial \mu} = 0 \tag{3.79}$$

$$\frac{\partial F_t}{\partial \delta_t^p} = \frac{\partial \overline{\sigma}}{\partial \delta_t^p}, \quad \frac{\partial F_t}{\partial T_t} = \frac{\partial \overline{\sigma}}{\partial T_t}, \quad \frac{\partial F_t}{\partial \mu} = 0 \tag{3.80}$$

Letting $\dfrac{\partial\overline{\sigma}}{\partial T_t} = g_t$, we have,

$$\begin{bmatrix} \Delta\delta_t^p \\ \Delta T_t \\ \Delta\mu \end{bmatrix}_n = \begin{bmatrix} \Delta\delta_t^p \\ \Delta T_t \\ \Delta\mu \end{bmatrix}_{n-1} - \begin{bmatrix} 1-\Delta\mu\dfrac{\partial g_t}{\partial\delta_t^p} & -\Delta\mu\dfrac{\partial g_t}{\partial T_t} & -g_t \\ E_t & sign(T_t) & 0 \\ \dfrac{\partial\overline{\sigma}}{\partial\delta_t^p} & g_t & 0 \end{bmatrix}_{n-1}^{-1} \begin{bmatrix} G_t \\ H_t \\ F \end{bmatrix}_{n-1}$$

$$\overline{\sigma} = \left[\frac{3T_t^2}{(1-f)^2}\right]^{\frac{1}{2}} = \frac{\sqrt{3}|T_t|}{(1-f)} \tag{3.81}$$

$$df = d\delta_t^p\frac{2\sqrt{f}}{l} \tag{3.82}$$

$$dh = -d\delta_t^p\frac{h}{a} \tag{3.83}$$

$$d\delta_t = d\delta_t^e + d\delta_t^p \tag{3.84}$$

Evolution of f and h was found in (3.31), but here δ_t^p is used.

$$f_{n+1} = \left(\sqrt{f_n + \frac{(\Delta\delta_t^p)^2}{l^2}} + \frac{\Delta\delta_t^p}{l}\right)^2 \tag{3.85}$$

$$h_{n+1} = \frac{h_n}{1+\dfrac{\Delta\delta_t^p}{\sqrt{f_0}l}} \tag{3.86}$$

Derivatives,

$$g_t = \frac{\partial\overline{\sigma}}{\partial T_t} = \frac{3T_t}{\overline{\sigma}(1-f)^2} \tag{3.87}$$

$$\frac{\partial g_t}{\partial T_t} = \frac{3}{(1-f)^2}\frac{(\overline{\sigma}-T_t g_t)}{\overline{\sigma}^2} \tag{3.88}$$

$$\frac{\partial\overline{\sigma}}{\partial f} = \frac{1}{2\overline{\sigma}}\left[\frac{6T_t^2}{(1-f)^3}\right] \tag{3.89}$$

$$\frac{\partial g_t}{\partial f} = \frac{-3T_t}{\overline{\sigma}^2}\frac{\partial\overline{\sigma}}{\partial f}\frac{1}{(1-f)^2} + \frac{3T_t}{\overline{\sigma}}\frac{2}{(1-f)^3} \tag{3.90}$$

$$\frac{\partial g_t}{\partial\delta_t^p} = \frac{\partial g_t}{\partial f}\frac{\partial f}{\partial\delta_t^p} = \frac{\partial g_t}{\partial f}\frac{2\sqrt{f}}{l} \tag{3.91}$$

$$\frac{\partial\overline{\sigma}}{\partial\delta_t^p} = \frac{\partial\overline{\sigma}}{\partial f}\frac{\partial f}{\partial\delta_t^p} = \frac{\partial\overline{\sigma}}{\partial f}\frac{2\sqrt{f}}{l} \tag{3.92}$$

Similarly, the derivative $\partial T_t/\partial \delta_t$ can be found. Take derivative of (3.77) and (3.75) with respect to δ_t. We get,

$$
\begin{aligned}
\frac{\partial H_t}{\partial \delta_t} &= \frac{\partial T_t}{\partial \delta_t} - E_t + E_t \frac{\partial \delta_t^p}{\partial \delta_t} = 0 && (3.93) \\
\frac{\partial F}{\partial \delta_t} &= \frac{\partial \overline{\sigma}}{\partial \delta_t^p}\frac{\partial \delta_t^p}{\partial \delta_t} + \frac{\partial \overline{\sigma}}{\partial T_t}\frac{\partial T_t}{\partial \delta_t} = 0 && (3.94)
\end{aligned}
$$

Here, there are two unknowns, $\dfrac{\partial T_t}{\partial \delta_t}$ and $\dfrac{\partial \delta_t^p}{\partial \delta_t}$, and two equations. Solving the system, we find,

$$
\frac{\partial T_t}{\partial \delta_t} = \frac{-\dfrac{\partial \overline{\sigma}}{\partial \delta_t^p}}{g_t - \dfrac{\partial \overline{\sigma}}{\partial \delta_t^p}\dfrac{1}{E_t}} \tag{3.95}
$$

3.4.4 Mixed-mode using plasticity formulation

Finally, similar to pure mode-I and mode-II cases, the iteration scheme is applied for mixed-mode loading. Equations to be satisfied in the next increment,

$$
\begin{aligned}
F &= \overline{\sigma} - \sigma_y = 0 && (3.96) \\
G_n &= \Delta\delta_n^p - \Delta\mu \frac{\partial \overline{\sigma}}{\partial T_n} = 0 && (3.97) \\
G_t &= \Delta\delta_t^p - \Delta\mu \frac{\partial \overline{\sigma}}{\partial T_t} = 0 && (3.98) \\
H_n &= T_n + \Delta T_n - E_n(\delta_n + \Delta\delta_n - \delta_n^p - \Delta\delta_n^p) = 0 && (3.99) \\
H_t &= T_t + \Delta T_t - E_t(|\delta_t + \Delta\delta_t| - \delta_t^p - \Delta\delta_t^p) = 0 && (3.100)
\end{aligned}
$$

Unknowns: $\Delta\delta_n^p$, $\Delta\delta_t^p$, ΔT_n, ΔT_t, $\Delta\mu$ where $\overline{\sigma} := \overline{\sigma}(\delta_n^p, \delta_t^p, T_n, T_t)$

Using Newton-Raphson's algorithm,

$$\begin{bmatrix} \Delta\delta_n^p \\ \Delta\delta_t^p \\ \Delta T_n \\ \Delta T_t \\ \Delta\mu \end{bmatrix}_n = \begin{bmatrix} \Delta\delta_n^p \\ \Delta\delta_t^p \\ \Delta T_n \\ \Delta T_t \\ \Delta\mu \end{bmatrix}_{n-1} - \begin{bmatrix} \frac{\partial G_n}{\partial\delta_n^p} & \frac{\partial G_n}{\partial\delta_t^p} & \frac{\partial G_n}{\partial T_n} & \frac{\partial G_n}{\partial T_t} & \frac{\partial G_n}{\partial\mu} \\ \frac{\partial G_t}{\partial\delta_n^p} & \frac{\partial G_t}{\partial\delta_t^p} & \frac{\partial G_t}{\partial T_n} & \frac{\partial G_t}{\partial T_t} & \frac{\partial G_t}{\partial\mu} \\ \frac{\partial H_n}{\partial\delta_n^p} & \frac{\partial H_n}{\partial\delta_t^p} & \frac{\partial H_n}{\partial T_n} & \frac{\partial H_n}{\partial T_t} & \frac{\partial H_n}{\partial\mu} \\ \frac{\partial H_t}{\partial\delta_n^p} & \frac{\partial H_t}{\partial\delta_t^p} & \frac{\partial H_t}{\partial T_n} & \frac{\partial H_t}{\partial T_t} & \frac{\partial H_t}{\partial\mu} \\ \frac{\partial F}{\partial\delta_n^p} & \frac{\partial F}{\partial\delta_t^p} & \frac{\partial F}{\partial T_n} & \frac{\partial F}{\partial T_t} & \frac{\partial F}{\partial\mu} \end{bmatrix}_{n-1}^{-1} \begin{bmatrix} G_n \\ G_t \\ H_n \\ H_t \\ F \end{bmatrix}_{n-1}$$

Derivatives are given by,

$$\begin{aligned}
&\frac{\partial G_n}{\partial\delta_n^p} = 1 - \Delta\mu\frac{\partial\left(\frac{\partial\overline{\sigma}}{\partial T_n}\right)}{\partial\delta_n^p}, && \frac{\partial G_n}{\partial\delta_t^p} = -\Delta\mu\frac{\partial\left(\frac{\partial\overline{\sigma}}{\partial T_n}\right)}{\partial\delta_t^p}, && \\
&\frac{\partial G_n}{\partial T_n} = -\Delta\mu\frac{\partial^2\overline{\sigma}}{\partial T_n^2}, && \frac{\partial G_n}{\partial T_t} = -\Delta\mu\frac{\partial^2\overline{\sigma}}{\partial T_t\partial T_n}, && \frac{\partial G_n}{\partial\mu} = -\frac{\partial\overline{\sigma}}{\partial T_n} \\
&\frac{\partial G_t}{\partial\delta_n^p} = -\Delta\mu\frac{\partial\left(\frac{\partial\overline{\sigma}}{\partial T_t}\right)}{\partial\delta_n^p}, && \frac{\partial G_t}{\partial\delta_t^p} = 1 - \Delta\mu\frac{\partial\left(\frac{\partial\overline{\sigma}}{\partial T_t}\right)}{\partial\delta_t^p}, && \\
&\frac{\partial G_t}{\partial T_n} = -\Delta\mu\frac{\partial^2\overline{\sigma}}{\partial T_t\partial T_n}, && \frac{\partial G_t}{\partial T_t} = -\Delta\mu\frac{\partial^2\overline{\sigma}}{\partial T_t^2}, && \frac{\partial G_t}{\partial\mu} = -\frac{\partial\overline{\sigma}}{\partial T_t} \\
&\frac{\partial H_n}{\partial\delta_n^p} = E_n, && \frac{\partial H_n}{\partial\delta_t^p} = 0, && \\
&\frac{\partial H_n}{\partial T_n} = 1, && \frac{\partial H_n}{\partial T_t} = 0, && \frac{\partial H_n}{\partial\mu} = 0 \\
&\frac{\partial H_t}{\partial\delta_n^p} = 0, && \frac{\partial H_t}{\partial\delta_t^p} = E_t, && \\
&\frac{\partial H_t}{\partial T_n} = 0, && \frac{\partial H_t}{\partial T_t} = 1, && \frac{\partial H_t}{\partial\mu} = 0 \\
&\frac{\partial F}{\partial\delta_n^p} = \frac{\partial\overline{\sigma}}{\partial\delta_n^p}, && \frac{\partial F}{\partial\delta_t^p} = \frac{\partial\overline{\sigma}}{\partial\delta_t^p}, && \\
&\frac{\partial F}{\partial T_n} = \frac{\partial\overline{\sigma}}{\partial T_n}, && \frac{\partial F}{\partial T_t} = \frac{\partial\overline{\sigma}}{\partial T_t}, && \frac{\partial F}{\partial\mu} = 0
\end{aligned}$$

Letting $\dfrac{\partial\overline{\sigma}}{\partial T_n} = g_n$ and $\dfrac{\partial\overline{\sigma}}{\partial T_t} = g_t$, we have,

$$[A_n] = \begin{bmatrix} \Delta\delta_n^p \\ \Delta\delta_t^p \\ \Delta T_n \\ \Delta T_t \\ \Delta\mu \end{bmatrix}_n , \quad [A_{n-1}] = \begin{bmatrix} \Delta\delta_n^p \\ \Delta\delta_t^p \\ \Delta T_n \\ \Delta T_t \\ \Delta\mu \end{bmatrix}_{n-1} , \quad [C_{n-1}] = \begin{bmatrix} G_n \\ G_t \\ H_n \\ H_t \\ F \end{bmatrix}_{n-1}$$

$$[B_{n-1}] = \begin{bmatrix} 1-\Delta\mu\dfrac{\partial g_n}{\partial\delta_n^p} & -\Delta\mu\dfrac{\partial g_n}{\partial\delta_t^p} & -\Delta\mu\dfrac{\partial g_n}{\partial T_n} & -\Delta\mu\dfrac{\partial g_n}{\partial T_t} & -g_n \\ -\Delta\mu\dfrac{\partial g_t}{\partial\delta_n^p} & 1-\Delta\mu\dfrac{\partial g_t}{\partial\delta_t^p} & -\Delta\mu\dfrac{\partial g_t}{\partial T_n} & -\Delta\mu\dfrac{\partial g_t}{\partial T_t} & -g_t \\ E_n & 0 & 1 & 0 & 0 \\ 0 & E_t & 0 & 1 & 0 \\ \dfrac{\partial\overline{\sigma}}{\partial\delta_n^p} & \dfrac{\partial\overline{\sigma}}{\partial\delta_t^p} & g_n & g_t & 0 \end{bmatrix}_{n-1}$$

Iterate by,

$$[A_n] = [A_{n-1}] - [B_{n-1}]^{-1}[C_{n-1}] \tag{3.101}$$

$$\overline{\sigma} = \left[\frac{T_n^2}{(1-f)^2 + (lnf)^2/3} + \frac{3T_t^2}{(1-f)^2}\right]^{\frac{1}{2}} \tag{3.102}$$

$$df = d\delta_n^p\frac{(1-f)}{h} + d\delta_t^p\frac{2\sqrt{f}}{l} \tag{3.103}$$

$$dh = d\delta_n^p - d\delta_t^p\frac{h}{a} \tag{3.104}$$

$$d\delta_n = d\delta_n^e + d\delta_n^p \tag{3.105}$$

$$d\delta_t = d\delta_t^e + d\delta_t^p \tag{3.106}$$

Update of f and h for mixed-mode was found in (3.35). Here, δ_n^p and δ_t^p are used.

$$f_{n+1} = \frac{\left(\frac{\Delta\delta_t^p}{l} + \sqrt{\frac{(\Delta\delta_t^p)^2}{l^2} + \frac{(\Delta\delta_n^p)^2}{h_{n+1}^2} + f_n + \frac{\Delta\delta_n^p}{h_{n+1}}(f_n+1)}\right)^2}{\left(1 + \frac{\Delta\delta_n^p}{h_{n+1}}\right)^2} \tag{3.107}$$

$$h_{n+1} = \frac{h_n + \Delta\delta_n^p}{1 + \frac{\Delta\delta_t^p}{\sqrt{f_0}l}} \tag{3.108}$$

Derivatives,

$$g_n = \frac{\partial\overline{\sigma}}{\partial T_n} = \frac{T_n}{\overline{\sigma}[(1-f)^2 + (lnf)^2/3]} \tag{3.109}$$

$$g_t = \frac{\partial\overline{\sigma}}{\partial T_t} = \frac{3T_t}{\overline{\sigma}(1-f)^2} \tag{3.110}$$

$$\frac{\partial g_n}{\partial T_n} = \frac{1}{[(1-f)^2 + (lnf)^2/3]}\frac{(\overline{\sigma} - T_n g_n)}{\overline{\sigma}^2} \tag{3.111}$$

$$\frac{\partial g_n}{\partial T_t} = \frac{T_n}{[(1-f)^2 + (lnf)^2/3]}\frac{(-g_t)}{\overline{\sigma}^2} \tag{3.112}$$

$$\frac{\partial g_t}{\partial T_n} = \frac{3T_t}{(1-f)^2}\frac{(-g_n)}{\overline{\sigma}^2} \tag{3.113}$$

$$\frac{\partial g_t}{\partial T_t} = \frac{3}{(1-f)^2}\frac{(\overline{\sigma} - T_t g_t)}{\overline{\sigma}^2} \tag{3.114}$$

$$\frac{\partial\overline{\sigma}}{\partial f} = \frac{1}{2\overline{\sigma}}\left[\frac{-T_n^2[-2(1-f) + \frac{2}{3}lnf\frac{1}{f}]}{[(1-f)^2 + (lnf)^2/3]^2} + \frac{6T_t^2}{(1-f)^3}\right] \tag{3.115}$$

$$\frac{\partial g_n}{\partial f} = \frac{-T_n}{\overline{\sigma}^2}\left[\frac{\frac{\partial\overline{\sigma}}{\partial f}[(1-f)^2 + (lnf)^2/3] + \overline{\sigma}[-2(1-f) + \frac{2}{3}lnf\frac{1}{f}]}{[(1-f)^2 + (lnf)^2/3]^2}\right] \tag{3.116}$$

$$\frac{\partial g_n}{\partial \delta_n^p} = \frac{\partial g_n}{\partial f}\frac{\partial f}{\partial \delta_n^p} = \frac{\partial g_n}{\partial f}\frac{(1-f)}{h} \tag{3.117}$$

$$\frac{\partial g_n}{\partial \delta_t^p} = \frac{\partial g_n}{\partial f}\frac{\partial f}{\partial \delta_t^p} = \frac{\partial g_n}{\partial f}\frac{2\sqrt{f}}{l} \tag{3.118}$$

$$\frac{\partial g_t}{\partial f} = \frac{-3T_t}{\overline{\sigma}^2}\frac{\partial\overline{\sigma}}{\partial f}\frac{1}{(1-f)^2} + \frac{3T_t}{\overline{\sigma}}\frac{2}{(1-f)^3} \tag{3.119}$$

$$\frac{\partial g_t}{\partial \delta_n^p} = \frac{\partial g_t}{\partial f}\frac{\partial f}{\partial \delta_n^p} = \frac{\partial g_t}{\partial f}\frac{(1-f)}{h} \tag{3.120}$$

$$\frac{\partial g_t}{\partial \delta_t^p} = \frac{\partial g_t}{\partial f}\frac{\partial f}{\partial \delta_t^p} = \frac{\partial g_t}{\partial f}\frac{2\sqrt{f}}{l} \tag{3.121}$$

$$\frac{\partial\overline{\sigma}}{\partial\delta_n^p} = \frac{\partial\overline{\sigma}}{\partial f}\frac{\partial f}{\partial\delta_n^p} = \frac{\partial\overline{\sigma}}{\partial f}\frac{(1-f)}{h} \tag{3.122}$$

$$\frac{\partial\overline{\sigma}}{\partial\delta_t^p} = \frac{\partial\overline{\sigma}}{\partial f}\frac{\partial f}{\partial\delta_t^p} = \frac{\partial\overline{\sigma}}{\partial f}\frac{2\sqrt{f}}{l} \tag{3.123}$$

The Jacobian, $\dfrac{\partial\Delta T_i}{\partial\Delta\delta_j}$, is needed in finite element framework. As it was noted in section 3.4.1 it can be derived from the fact that $\Delta T_n, \Delta T_t, \Delta\delta_n^p, \Delta\delta_t^p, \Delta\mu$ are functions of $\Delta\delta_n$ and $\Delta\delta_t$. Following, take derivative of equations (3.96), (3.97), (3.98), (3.99) and (3.100) with respect to $\Delta\delta_n$ and $\Delta\delta_t$. Applying chain rule,

$$G_n = \Delta\delta_n^p - \Delta\mu\frac{\partial\overline{\sigma}}{\partial T_n} = 0 \quad \text{where} \quad \frac{\partial\overline{\sigma}}{\partial T_n} = g_n = g_n(\delta_n^p, \delta_t^p, T_n, T_t)$$

$$\begin{aligned}\frac{\partial G_n}{\partial\Delta\delta_n} =& \frac{\partial\Delta\delta_n^p}{\partial\Delta\delta_n} - \frac{\partial\Delta\mu}{\partial\Delta\delta_n}g_n - \Delta\mu\frac{\partial g_n}{\partial\Delta\delta_n^p}\frac{\partial\Delta\delta_n^p}{\partial\Delta\delta_n} - \Delta\mu\frac{\partial g_n}{\partial\Delta\delta_t^p}\frac{\partial\Delta\delta_t^p}{\partial\Delta\delta_n} \\ & - \Delta\mu\frac{\partial g_n}{\partial\Delta T_n}\frac{\partial\Delta T_n}{\partial\Delta\delta_n} - \Delta\mu\frac{\partial g_n}{\partial\Delta T_t}\frac{\partial\Delta T_t}{\partial\Delta\delta_n} = 0\end{aligned} \tag{3.124}$$

$$\begin{aligned}\frac{\partial G_n}{\partial\Delta\delta_t} =& \frac{\partial\Delta\delta_n^p}{\partial\Delta\delta_t} - \frac{\partial\Delta\mu}{\partial\Delta\delta_t}g_n - \Delta\mu\frac{\partial g_n}{\partial\Delta\delta_n^p}\frac{\partial\Delta\delta_n^p}{\partial\Delta\delta_t} - \Delta\mu\frac{\partial g_n}{\partial\Delta\delta_t^p}\frac{\partial\Delta\delta_t^p}{\partial\Delta\delta_t} \\ & - \Delta\mu\frac{\partial g_n}{\partial\Delta T_n}\frac{\partial\Delta T_n}{\partial\Delta\delta_t} - \Delta\mu\frac{\partial g_n}{\partial\Delta T_t}\frac{\partial\Delta T_t}{\partial\Delta\delta_t} = 0\end{aligned} \tag{3.125}$$

$$G_t = \Delta\delta_t^p - \Delta\mu\frac{\partial\overline{\sigma}}{\partial T_t} = 0 \quad \text{where} \quad \frac{\partial\overline{\sigma}}{\partial T_t} = g_t = g_t(\delta_n^p, \delta_t^p, T_n, T_t)$$

$$\begin{aligned}\frac{\partial G_t}{\partial\Delta\delta_n} =& \frac{\partial\Delta\delta_t^p}{\partial\Delta\delta_n} - \frac{\partial\Delta\mu}{\partial\Delta\delta_n}g_t - \Delta\mu\frac{\partial g_t}{\partial\Delta\delta_n^p}\frac{\partial\Delta\delta_n^p}{\partial\Delta\delta_n} - \Delta\mu\frac{\partial g_t}{\partial\Delta\delta_t^p}\frac{\partial\Delta\delta_t^p}{\partial\Delta\delta_n} \\ & - \Delta\mu\frac{\partial g_t}{\partial\Delta T_n}\frac{\partial\Delta T_n}{\partial\Delta\delta_n} - \Delta\mu\frac{\partial g_t}{\partial\Delta T_t}\frac{\partial\Delta T_t}{\partial\Delta\delta_n} = 0\end{aligned} \tag{3.126}$$

$$\begin{aligned}\frac{\partial G_t}{\partial\Delta\delta_t} =& \frac{\partial\Delta\delta_t^p}{\partial\Delta\delta_t} - \frac{\partial\Delta\mu}{\partial\Delta\delta_t}g_t - \Delta\mu\frac{\partial g_t}{\partial\Delta\delta_n^p}\frac{\partial\Delta\delta_n^p}{\partial\Delta\delta_t} - \Delta\mu\frac{\partial g_t}{\partial\Delta\delta_t^p}\frac{\partial\Delta\delta_t^p}{\partial\Delta\delta_t} \\ & - \Delta\mu\frac{\partial g_t}{\partial\Delta T_n}\frac{\partial\Delta T_n}{\partial\Delta\delta_t} - \Delta\mu\frac{\partial g_t}{\partial\Delta T_t}\frac{\partial\Delta T_t}{\partial\Delta\delta_t} = 0\end{aligned} \tag{3.127}$$

$$H_n = \Delta T_n - E_n(\Delta\delta_n - \Delta\delta_n^p) = 0$$

$$\frac{\partial H_n}{\partial \Delta\delta_n} = \frac{\partial \Delta T_n}{\partial \Delta\delta_n} - E_n + E_n \frac{\partial \Delta\delta_n^p}{\partial \Delta\delta_n} = 0 \tag{3.128}$$

$$\frac{\partial H_n}{\partial \Delta\delta_t} = \frac{\partial \Delta T_n}{\partial \Delta\delta_t} + E_n \frac{\partial \Delta\delta_n^p}{\partial \Delta\delta_t} = 0 \tag{3.129}$$

$$H_t = \Delta T_t - E_t(\Delta\delta_t - \Delta\delta_t^p) = 0$$

$$\frac{\partial H_t}{\partial \Delta\delta_n} = \frac{\partial \Delta T_t}{\partial \Delta\delta_n} + E_t \frac{\partial \Delta\delta_t^p}{\partial \Delta\delta_n} = 0 \tag{3.130}$$

$$\frac{\partial H_t}{\partial \Delta\delta_t} = \frac{\partial \Delta T_t}{\partial \Delta\delta_t} - E_t + E_t \frac{\partial \Delta\delta_t^p}{\partial \Delta\delta_t} = 0 \tag{3.131}$$

$$F = \overline{\sigma} - \sigma_y = 0 \quad \text{where} \quad \overline{\sigma} = \overline{\sigma}(\delta_n^p, \delta_t^p, T_n, T_t)$$

$$\frac{\partial F}{\partial \Delta\delta_n} = \frac{\partial \overline{\sigma}}{\partial \Delta\delta_n^p}\frac{\partial \Delta\delta_n^p}{\partial \Delta\delta_n} + \frac{\partial \overline{\sigma}}{\partial \Delta\delta_t^p}\frac{\partial \Delta\delta_t^p}{\partial \Delta\delta_n} + \frac{\partial \overline{\sigma}}{\partial \Delta T_n}\frac{\partial \Delta T_n}{\partial \Delta\delta_n} + \frac{\partial \overline{\sigma}}{\partial \Delta T_t}\frac{\partial \Delta T_t}{\partial \Delta\delta_n} = 0 \tag{3.132}$$

$$\frac{\partial F}{\partial \Delta\delta_t} = \frac{\partial \overline{\sigma}}{\partial \Delta\delta_n^p}\frac{\partial \Delta\delta_n^p}{\partial \Delta\delta_t} + \frac{\partial \overline{\sigma}}{\partial \Delta\delta_t^p}\frac{\partial \Delta\delta_t^p}{\partial \Delta\delta_t} + \frac{\partial \overline{\sigma}}{\partial \Delta T_n}\frac{\partial \Delta T_n}{\partial \Delta\delta_t} + \frac{\partial \overline{\sigma}}{\partial \Delta T_t}\frac{\partial \Delta T_t}{\partial \Delta\delta_t} = 0 \tag{3.133}$$

Equations (3.124)-(3.133) represent a system of linear equations with 10 equations and 10 unknowns;

$$\left(\frac{\partial \Delta\delta_n^p}{\partial \Delta\delta_n}, \frac{\partial \Delta\delta_n^p}{\partial \Delta\delta_t}, \frac{\partial \Delta\delta_t^p}{\partial \Delta\delta_n}, \frac{\partial \Delta\delta_t^p}{\partial \Delta\delta_t}, \frac{\partial \Delta T_n}{\partial \Delta\delta_n}, \frac{\partial \Delta T_n}{\partial \Delta\delta_t}, \frac{\partial \Delta T_t}{\partial \Delta\delta_n}, \frac{\partial \Delta T_t}{\partial \Delta\delta_t}, \frac{\partial \Delta\mu}{\partial \Delta\delta_n}, \frac{\partial \Delta\mu}{\partial \Delta\delta_t}\right)$$

It can be solved by using simple Gauss elimination or by taking the inverse of a 10 by 10 matrix. In the implementation LAPACK (Linear Algebra Package) library's DGESV subroutine is used to solve the system. It is highly efficient, and it is included in the Intel Fortran Compiler libraries. DGESV uses LU decomposition to solve the system. The matrix form of equations is given below. Solving it, the required unknowns $\frac{\partial \Delta T_n}{\partial \Delta\delta_n}, \frac{\partial \Delta T_n}{\partial \Delta\delta_t}, \frac{\partial \Delta T_t}{\partial \Delta\delta_n}, \frac{\partial \Delta T_t}{\partial \Delta\delta_t}$ are obtained for the Jacobian. For the variables in these system of equations, the last obtained values from iteration equation (3.101) are used.

$$[A][B] = [C], \;\; [B] = [A]^{-1}[C], \quad \text{Jacobian}, \quad [J] = \begin{bmatrix} \dfrac{\partial \Delta T_t}{\partial \Delta \delta_t} & \dfrac{\partial \Delta T_t}{\partial \Delta \delta_n} \\ \dfrac{\partial \Delta T_n}{\partial \Delta \delta_t} & \dfrac{\partial \Delta T_n}{\partial \Delta \delta_n} \end{bmatrix}$$

$$\text{Unknowns}, \quad [B] = \begin{bmatrix} \dfrac{\partial \Delta \delta_n^p}{\partial \Delta \delta_n} \\ \dfrac{\partial \Delta \delta_n^p}{\partial \Delta \delta_t} \\ \dfrac{\partial \Delta \delta_t^p}{\partial \Delta \delta_n} \\ \dfrac{\partial \Delta \delta_t^p}{\partial \Delta \delta_t} \\ \dfrac{\partial \Delta T_n}{\partial \Delta \delta_n} \\ \dfrac{\partial \Delta T_n}{\partial \Delta \delta_t} \\ \dfrac{\partial \Delta T_t}{\partial \Delta \delta_n} \\ \dfrac{\partial \Delta T_t}{\partial \Delta \delta_t} \\ \dfrac{\partial \Delta \mu}{\partial \Delta \delta_n} \\ \dfrac{\partial \Delta \mu}{\partial \Delta \delta_t} \end{bmatrix}, \quad \text{RHS}, \quad [C] = \begin{bmatrix} 0 \\ 0 \\ 0 \\ 0 \\ E_n \\ 0 \\ 0 \\ E_t \\ 0 \\ 0 \end{bmatrix}$$

$$
[\mathrm{A}]=\begin{bmatrix}
1-\Delta\mu\frac{\partial g_n}{\partial\Delta\delta_n^p} & 0 & -\Delta\mu\frac{\partial g_n}{\partial\Delta\delta_t^p} & 0 & -\Delta\mu\frac{\partial g_n}{\partial\Delta T_n} & 0 & -\Delta\mu\frac{\partial g_n}{\partial\Delta T_t} & 0 & -g_n & 0 \\
0 & 1-\Delta\mu\frac{\partial g_n}{\partial\Delta\delta_n^p} & 0 & -\Delta\mu\frac{\partial g_n}{\partial\Delta\delta_t^p} & 0 & -\Delta\mu\frac{\partial g_n}{\partial\Delta T_n} & 0 & -\Delta\mu\frac{\partial g_n}{\partial\Delta T_t} & 0 & -g_n \\
-\Delta\mu\frac{\partial g_t}{\partial\Delta\delta_n^p} & 0 & 1-\Delta\mu\frac{\partial g_t}{\partial\Delta\delta_t^p} & 0 & -\Delta\mu\frac{\partial g_t}{\partial\Delta T_n} & 0 & -\Delta\mu\frac{\partial g_t}{\partial\Delta T_t} & 0 & -g_t & 0 \\
0 & -\Delta\mu\frac{\partial g_t}{\partial\Delta\delta_n^p} & 0 & 1-\Delta\mu\frac{\partial g_t}{\partial\Delta\delta_t^p} & 0 & -\Delta\mu\frac{\partial g_t}{\partial\Delta T_n} & 0 & -\Delta\mu\frac{\partial g_t}{\partial\Delta T_t} & 0 & -g_t \\
E_n & 0 & 0 & 0 & 1 & 0 & 0 & 0 & 0 & 0 \\
0 & E_n & 0 & 0 & 0 & 1 & 0 & 0 & 0 & 0 \\
0 & 0 & E_t & 0 & 0 & 0 & 1 & 0 & 0 & 0 \\
0 & 0 & 0 & E_t & 0 & 0 & 0 & 1 & 0 & 0 \\
\frac{\partial\overline{\sigma}}{\partial\Delta\delta_n^p} & 0 & \frac{\partial\overline{\sigma}}{\partial\Delta\delta_t^p} & 0 & g_n & 0 & g_t & 0 & 0 & 0 \\
0 & \frac{\partial\overline{\sigma}}{\partial\Delta\delta_n^p} & 0 & \frac{\partial\overline{\sigma}}{\partial\Delta\delta_t^p} & 0 & g_n & 0 & g_t & 0 & 0
\end{bmatrix}
$$

The implementation of mixed-mode UEL is very lengthy. Every combination of contact, unloading/reloading, elastic/plastic loading is considered separately. Therefore, algorithm for mixed-mode will be explained mostly with words.

–Contact cases, $\delta_n \leqslant 0$

$T_n = E_n\delta_n,\ D_{nn} = E_n,\ D_{nt} = 0$

if $|\delta_t| \geqslant \delta_{t,max}$ *and* $f < 1$ *(T_t loading)* **then**

  if $\overline{\sigma} < \sigma_y$ *(Elastic) where* $\overline{\sigma} = \overline{\sigma}(T_t, \delta_t^p)$ **then**

    $T_t = E_t(|\delta_t| - \delta_t^p)sign(\delta_t),\ D_{tt} = E_t,\ D_{tn} = 0$

  else if $\overline{\sigma} \geqslant \sigma_y$ *(Plastic)* **then**

    Iterate using mode-II plasticity formulation. Find $\Delta\delta_t^p, \Delta T_t, \Delta\mu$

    $D_{tt} =$ Found using variables from last iteration, $D_{tn} = 0$

  end

else if $|\delta_t| < \delta_{t,max}$ *and* $f < 1$ *(T_t unloading)* **then**

  $T_t = E_t(\delta_{t,max} - \delta_t^p)\frac{|\delta_t|}{\delta_{t,max}}sign(\delta_t),\ \ D_{tt} = E_t(\delta_{t,max} - \delta_t^p)\frac{1}{\delta_{t,max}},\ \ D_{tn} = 0$

else if $f \geqslant 1$ *(Failure)* **then**

  $T_t = 0, D_{tt} = 0, D_{tn} = 0$

end

–Separation cases, $\delta_n > 0$

if $|\delta_t| \geqslant \delta_{t,max}$ *and* $\delta_n \geqslant \delta_{n,max}$ *and* $f < 1$ *(T_t, T_n loading)* **then**

  if $\overline{\sigma} < \sigma_y$ *(Elastic) where* $\overline{\sigma} = \overline{\sigma}(T_t, T_n, \delta_t^p, \delta_n^p)$ **then**

    $T_t = E_t(|\delta_t| - \delta_t^p)sign(\delta_t),\ D_{tt} = E_t,\ D_{tn} = 0$

    $T_n = E_n(\delta_n - \delta_n^p),\ D_{nn} = E_n,\ D_{nt} = 0$

  else if $\overline{\sigma} \geqslant \sigma_y$ *(Plastic)* **then**

    Iterate using mixed-mode plasticity formulation.

    Find $\Delta\delta_t^p, \Delta\delta_n^p, \Delta T_t, \Delta T_n, \Delta\mu$

    $D_{tt,tn,nt,nn} =$ Found using variables from last iteration

  end

else if $|\delta_t| < \delta_{t,max}$ *and* $\delta_n \geqslant \delta_{n,max}$ *and* $f < 1$ *(T_t unloading, T_n loading)* **then**

  $T_t = E_t(\delta_{t,max} - \delta_t^p)\frac{|\delta_t|}{\delta_{t,max}}sign(\delta_t),\ D_{tt} = E_t(\delta_{t,max} - \delta_t^p)\frac{1}{\delta_{t,max}},\ D_{tn} = 0$

  if $\overline{\sigma} < \sigma_y$ *(Elastic) where* $\overline{\sigma} = \overline{\sigma}(T_t, T_n, \delta_n^p)$ **then**

    $T_n = E_n(\delta_n - \delta_n^p),\ D_{nn} = E_n,\ D_{nt} = 0$

  else if $\overline{\sigma} \geqslant \sigma_y$ *(Plastic)* **then**

    Iterate using mode-I plasticity formulation. Find $\Delta\delta_n^p, \Delta T_n, \Delta\mu$

    $D_{nn} =$ Found using variables from last iteration, $D_{nt} = 0$

  end

else if $|\delta_t| \geqslant \delta_{t,max}$ *and* $\delta_n < \delta_{n,max}$ *and* $f < 1$ *(T_t loading, T_n unloading)* **then**

$T_n = E_n(\delta_{n,max} - \delta_n^p)\frac{\delta_n}{\delta_{n,max}},\ D_{nn} = E_n(\delta_{n,max} - \delta_n^p)\frac{1}{\delta_{n,max}},\ D_{nt} = 0$

if $\overline{\sigma} < \sigma_y$ *(Elastic) where* $\overline{\sigma} = \overline{\sigma}(T_t, T_n, \delta_t^p)$ **then**

$T_t = E_t(|\delta_t| - \delta_t^p)sign(\delta_t),\ D_{tt} = E_t,\ D_{tn} = 0$

else if $\overline{\sigma} \geqslant \sigma_y$ *(Plastic)* **then**

Iterate using mode-II plasticity formulation. Find $\Delta\delta_t^p, \Delta T_t, \Delta\mu$

$D_{tt} =$ Found using variables from last iteration, $D_{tn} = 0$

end

else if $|\delta_t| < \delta_{t,max}$ *and* $\delta_n < \delta_{n,max}$ *and* $f < 1$ *(T_t, T_n unloading)* **then**

$T_t = E_t(\delta_{t,max} - \delta_t^p)\frac{|\delta_t|}{\delta_{t,max}}sign(\delta_t),\ D_{tt} = E_t(\delta_{t,max} - \delta_t^p)\frac{1}{\delta_{t,max}},\ D_{tn} = 0$

$T_n = E_n(\delta_{n,max} - \delta_n^p)\frac{\delta_n}{\delta_{n,max}},\ D_{nt} = 0,\ D_{nn} = E_n(\delta_{n,max} - \delta_n^p)\frac{1}{\delta_{n,max}}$

else if $f \geqslant 1$ *(Failure)* **then**

$T_t = 0, T_n = 0, D_{tt} = 0, D_{tn} = 0, D_{nt} = 0, D_{nn} = 0$

end

Algorithm 3: Evaluation of tractions and derivatives of tractions for mixed-mode implementation.

In Figs. 3.10 and 3.11 traction-separation results are presented, where the one element FE model (Figs. 3.4 and 3.6) used to test the uncoupled and incremental implementation is employed again with the mixed-mode implementation using different elastic slopes. It is observed that the results are the same if the elastic slope is high enough. However, the error grows with decreasing elastic slope and results in divergence if the slope is too small.

We want to analyze the mixed mode behavior, for example, obtain traction surfaces as a function of normal and tangential separation, or find the change in fracture energy based on mode mixity. Unlike potential based cohesive zone models, there is not an explicit expression for the tractions, so traction surfaces cannot be readily plotted. Instead, there is a system of non-linear equations that can be solved with a numerical iteration scheme. Because of this nature, the micromechanics based cohesive zone model is intrinsically path-dependant. Meaning, the same traction will not be obtained at a given normal and tangential separation if different paths are taken to get to those separations. Note that this path dependency can be physically motivated. Bosch et al. [79] point out that different amounts of energy would be dissipated in an

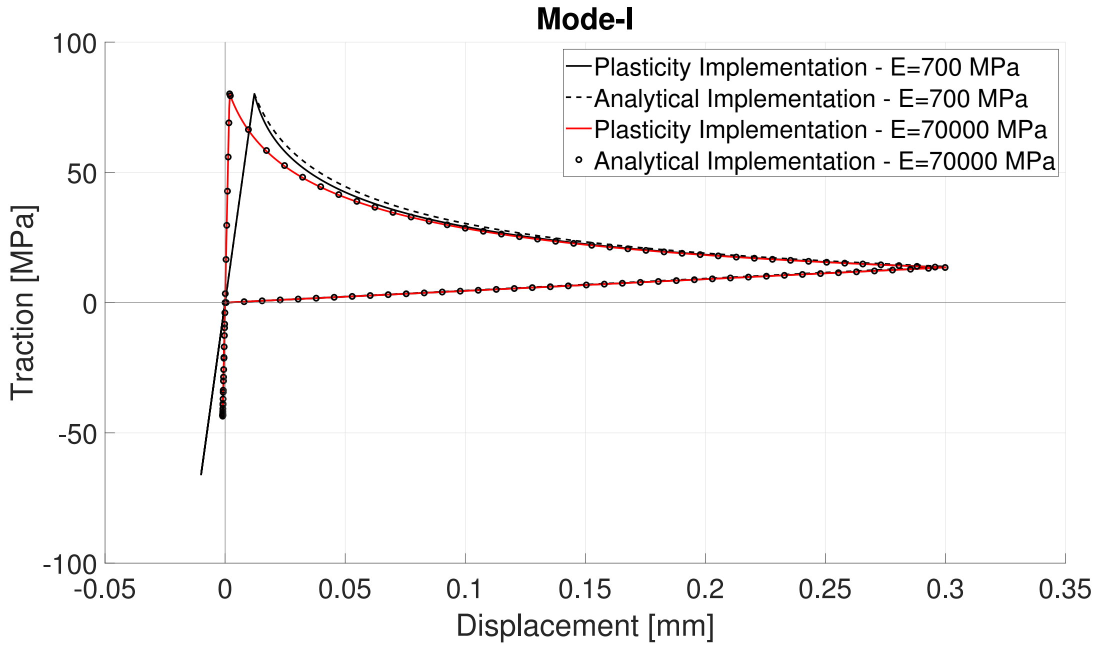

Figure 3.10: Traction versus displacement response to mode-I loading/unloading using mixed-mode implementation.

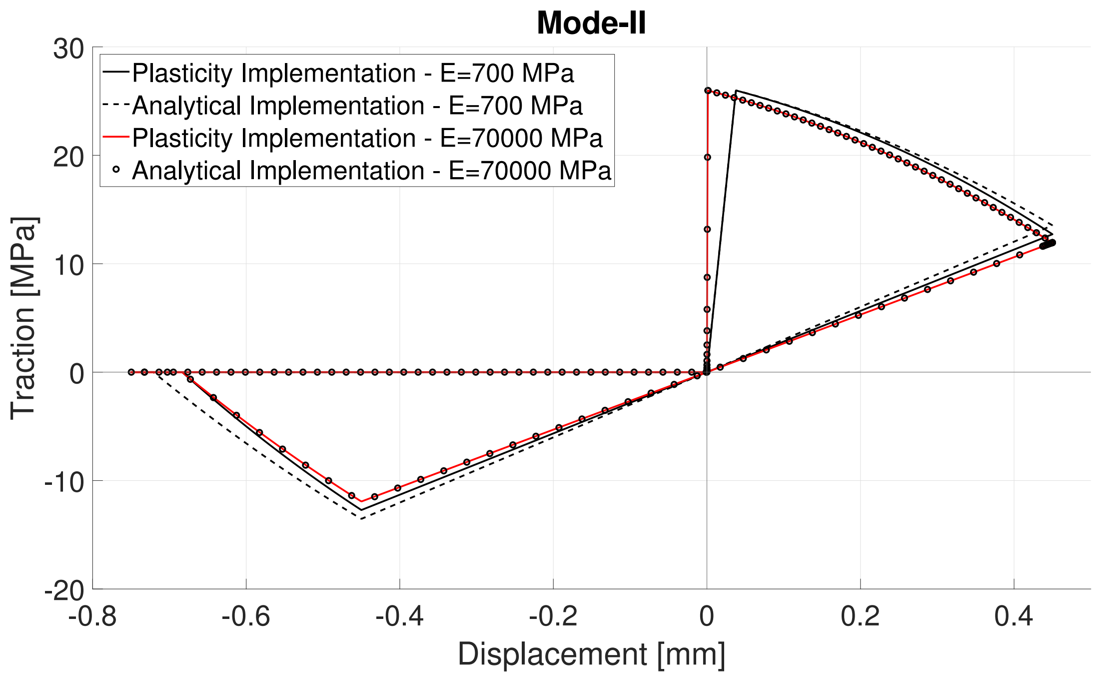

Figure 3.11: Traction versus displacement response to mode-II loading/unloading using mixed-mode implementation.

idealized rough interface depending on path, and an irreversible damage process of the interface is expected to be path-dependent. Hence, there is not a single traction surface for this model. However, it is possible to get an idea by trying proportional loading cases. Let $\alpha = tan^{-1}\left(\frac{\delta_n}{\delta_t}\right)$ be the proportionality ratio. If $\alpha = 0^o$, loading is Mode-II, or if $\alpha = 90^o$, it is Mode-I loading. Values in between correspond to mixed-mode loading with different mixity ratios (See Fig. 3.12). A MATLAB script

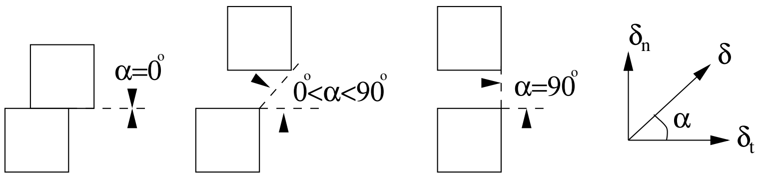

Figure 3.12: Proportional loading of cohesive element where α is proportionality ratio.

is used to solve mixed-mode numerical scheme at a single material point. Separation is applied such that the proportionality ratio changes from 0^o to 90^o, and resulting traction surfaces are plotted in Fig. 3.13 for normal traction and Fig. 3.14 for tangential traction. Effect of mixed-mode can be observed, where the decrease in tractions depend strongly on the proportionality ratio.

Moreover, the work of fracture is calculated using these traction surface data. Work of fracture can be expressed as,

$$W_f = W_n + W_t \tag{3.134}$$

where W_n is work due to normal separation and W_t is work due to tangential separation. Hence,

$$W_f = \int_0^{\delta} T_n(\delta\text{sin}\alpha, \delta\text{cos}\alpha)\text{sin}\alpha d\delta + \int_0^{\delta} T_t(\delta\text{sin}\alpha, \delta\text{cos}\alpha)\text{cos}\alpha d\delta \tag{3.135}$$

In Fig. 3.15 change of normal work, tangential work and total work with respect to proportionality ratio is presented. With the given MBCZM parameters, mode-II work is less than mode-I work. This can be altered by changing the parameters. For example, h_0 changes W_n without affecting W_t. Similarly, l has the opposite effect. This is demonstrated in Fig. 3.16.

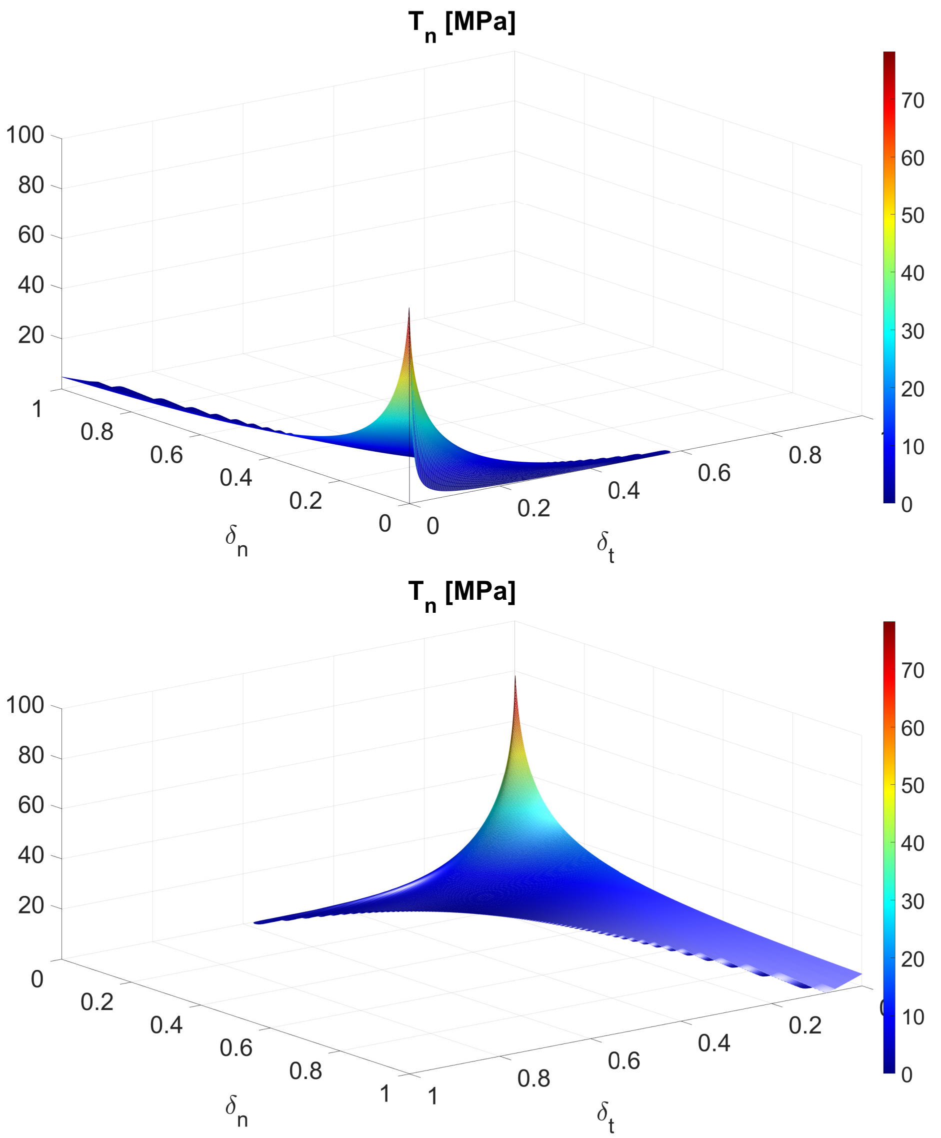

Figure 3.13: Normal traction surface for proportional loading from different view angles. MBCZM model parameters are: σ_y=50 MPa, h_0=0.1 mm, f_0=0.1, l=1 mm, En=700 GPa, Et=70 GPa

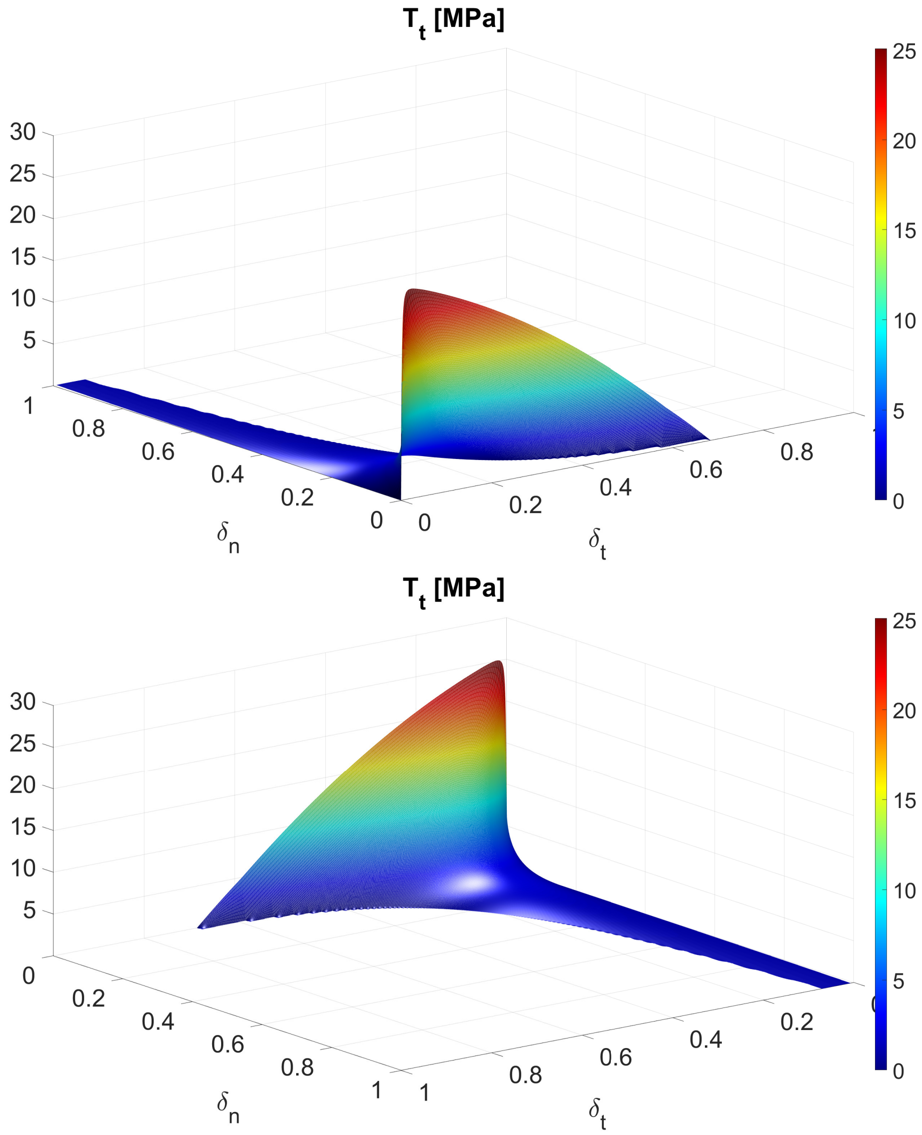

Figure 3.14: Tangential traction surface for proportional loading from different view angles. MBCZM model parameters are: σ_y=50 MPa, h_0=0.1 mm, f_0=0.1, l=1 mm, En=700 GPa, Et=70 GPa

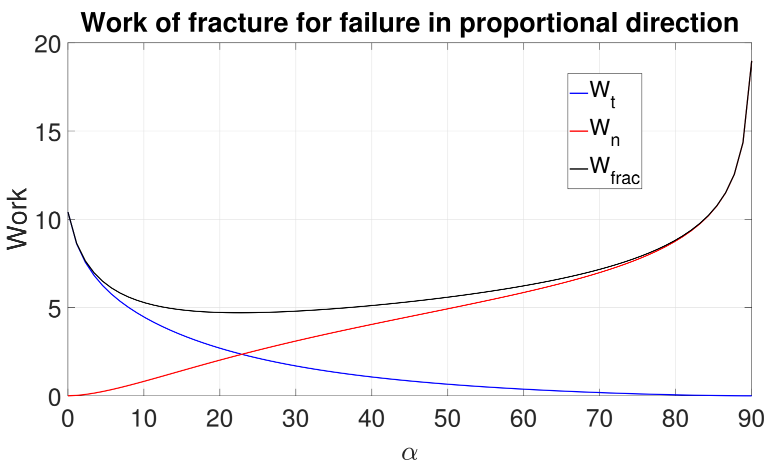

Figure 3.15: Work of fracture for proportional loading. MBCZM model parameters are: σ_y=50 MPa, h_0=0.1 mm, f_0=0.1, l=1 mm, En=700 GPa, Et=70 GPa

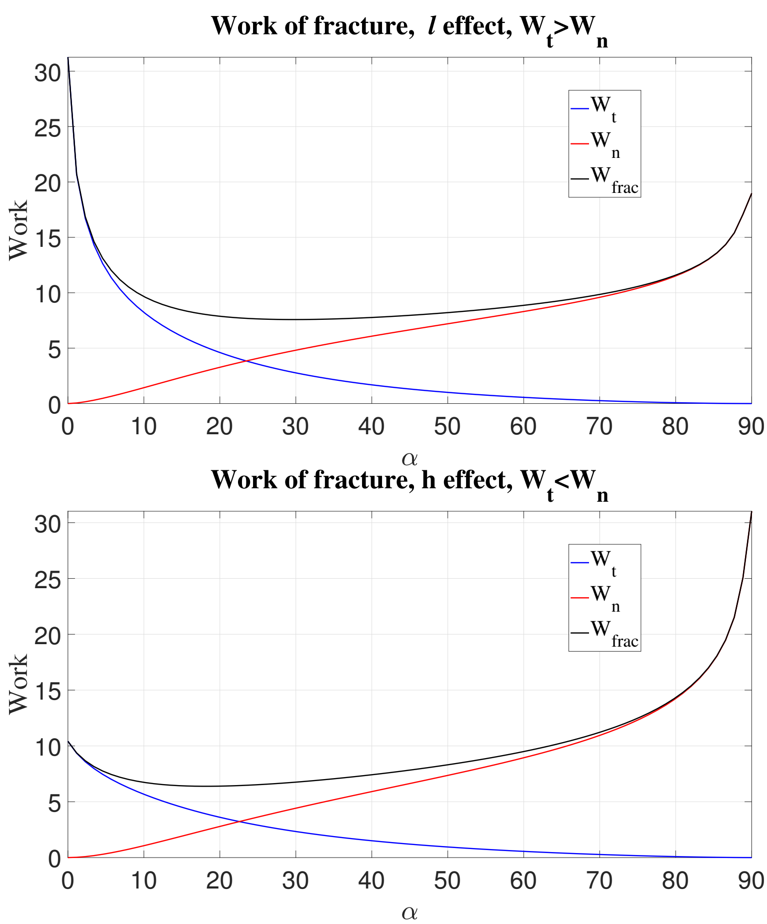

Figure 3.16: Effect of h and l is shown on work of fracture. $h_0 = 0.1mm, l = 3mm$ (top), $h_0 = 0.2mm, l = 1mm$ (bottom)

CHAPTER 4

DUCTILE FRACTURE MODELLING USING MBCZM

In this chapter, numerical simulations are done for mode-I, mode-II, and mixed-mode specimens using the MBCZM implemented as a UEL subroutine in Abaqus software. For the mode-I CT specimen example, the analytical implementation scheme given in Chapter 3 is used. For mode-I, mode-II, mixed-mode SEN specimen examples, mixed-mode implementation scheme is used. Some of the results presented in this chapter for the CT specimen have already been discussed in Yalçinkaya et al. [3].

It is important to note that the dimension of cohesive parameters and numerical models in the subsequent sections are on the order of millimeters. This length scale is not suitable considering that the cohesive zone model was derived based on pore growth where the size is on the order of micrometers. However, this is not a problem because the purpose here is not to make realistic comparisons with experiments, but to understand the behavior and the effect of the parameters present in the MBCZM and test the implementation. The traction separation laws are size-independent since separations are normalized in the model, i.e., they exist as δ_n/h or δ_t/l. Therefore, conclusions obtained about the cohesive zone model with macro specimens are relevant in the micro-sized specimens.

An interesting application of the developed MBCZM is the prediction of micromechanics based intergranular cracking in polycrystalline plasticity, which is more suitable considering the length-scale of the problem and the cohesive zone model. We have conducted an extensive study of this problem by combining a strain gradient crystal plasticity framework (see Yalcinkaya et al. [98], Klusemann and Yalcinkaya [99], Klusemann et al. [100]) with the MBCZM relations, which shows clearly the influence of the microstructural parameters on the toughness of the material. The work has recently been submitted for a journal publication (see Yalcinkaya et al. [101]), and the fundamental observations are presented in the next chapter.

4.1 Material

In this section, the developed model's performance is tested through numerical simulations conducted in Abaqus software for the SS316 austenitic steel presented in Fig. 4.1. For the bulk response, isotropic elasticity and von Mises (J2) plasticity are used, while cohesive zone elements are inserted ahead of the notch. A curve fit of the experimental true stress-strain data is used for hardening. The material parameters for bulk material and cohesive zone model are given below. Note that various sets from the given cohesive parameters are chosen in the simulations.

$$For\ the\ bulk\ material:$$

$$E = 210[GPa], \quad \nu = 0.3, \quad \text{Plastic data in Fig. 4.1}$$

$$For\ the\ cohesive\ zone:$$

$$\begin{aligned} &f_0 = 0.05 - 0.1 - 0.2 && h_0 = 0.05 - 0.1 - 0.2\ [mm] \\ &l = 0.25 - 0.5 - 1 - 2\ [mm] && \sigma_y = 100 - 300 - 500\ [MPa] \\ &E_n = 70 - 700\ [GPa] && E_t = 70\ [GPa] \end{aligned}$$

4.2 CT Specimen for Mode-I Ductile Failure Analysis

The specimen is prepared according to ASTM-E1820 standards [102], which is used for fracture toughness calculations experimentally, see Fig. 4.2. It has dimension $W = 100$mm. Since the width of the specimen, $W/2$, is sufficiently large, plane strain elements are used for the bulk, and cohesive elements are inserted ahead of the initial crack. Boundary conditions and mesh of the FE model are given in Fig. 4.2 where red crosses are cohesive elements. The bottom hole is not allowed to move while the top hole is given an upwards displacement, allowing the crack to open up. In

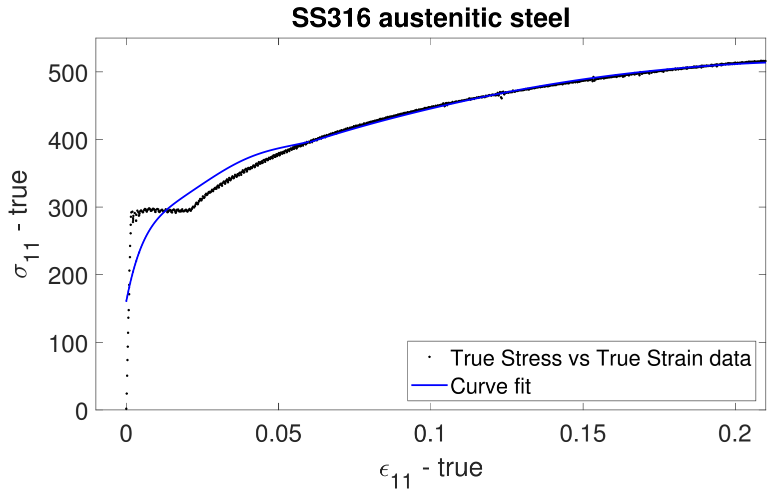

Figure 4.1: True stress-strain data for SS316LN steel.

the FE model, there is a reference point at the center of each hole, which is coupled to the hole surface, and the boundary conditions are applied at this reference point. The mesh shown in Fig. 4.2 contains 52163 nodes, 51135 CPE4 quadrilateral elements, 90 cohesive elements, and the approximate global element size is $0.5mm$. In order to check if the results are mesh dependant, a finer mesh with an approximate global element size equal to 0.3 is used, and it is concluded that mesh size is adequately small.

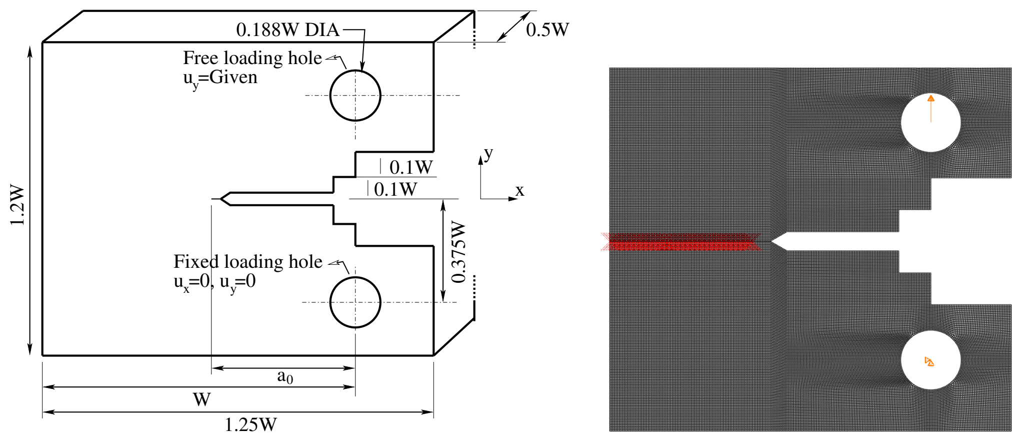

Figure 4.2: ASTM-E1820 CT Specimen and the FE model with $W = 100mm$.

4.2.1 Mode-I Loading

In Fig. 4.3 the effect of the initial porosity ahead of the crack tip is illustrated in the CT specimen. Stress contours are shown just before the crack starts to propagate, which corresponds to the moment at which the specimen carries the highest load, the peak points in Fig. 4.4. It can be seen that for higher initial pore fraction values, the specimen's stress carrying capacity reduces, and the maximum stress magnitude drops. This is also related to the fact that the crack propagation occurs earlier for the higher initial porosity values.

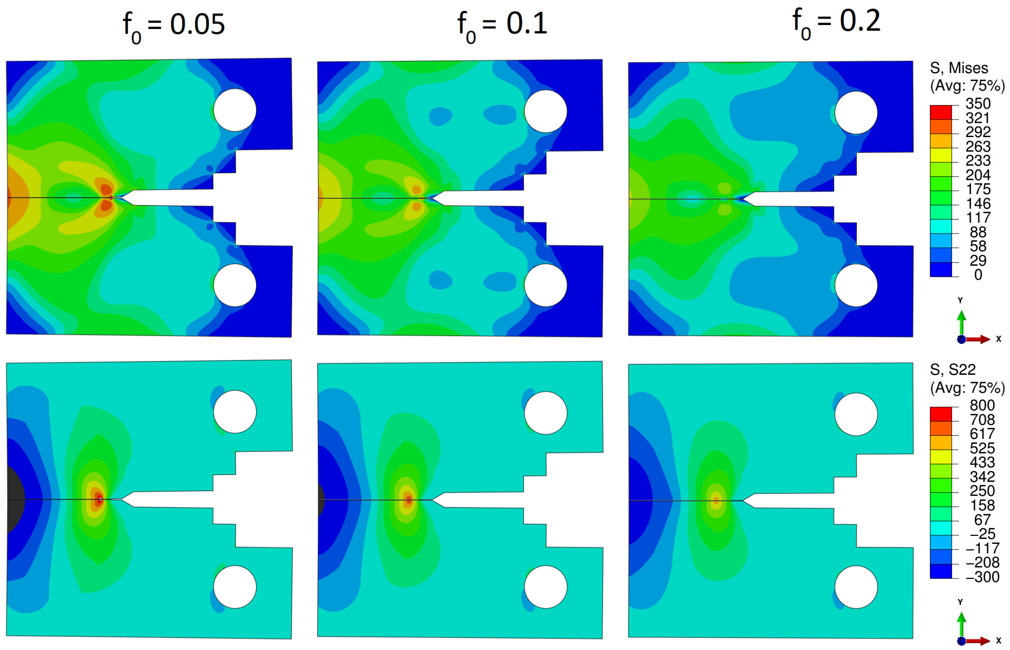

Figure 4.3: Stress contours for different initial pore fractions are shown, where the top row is the von Mises stress and the bottom row is the normal stress in the y-direction.

Similar conclusions can be obtained from the load-displacement curve presented in Fig. 4.4. The maximum stress gets smaller for higher porosity cases, and softening is observed at an earlier global strain level. Additionally, the toughness of the specimen reduces with higher initial pore fraction. Note that a finer mesh result is also shown in the same figure, and results are almost the same. In cohesive zone modelling, when cohesive elements are not small enough, a numerical instability can be observed that results in an oscillating force-displacement curve. This was observed during simulations, but it is not included here.

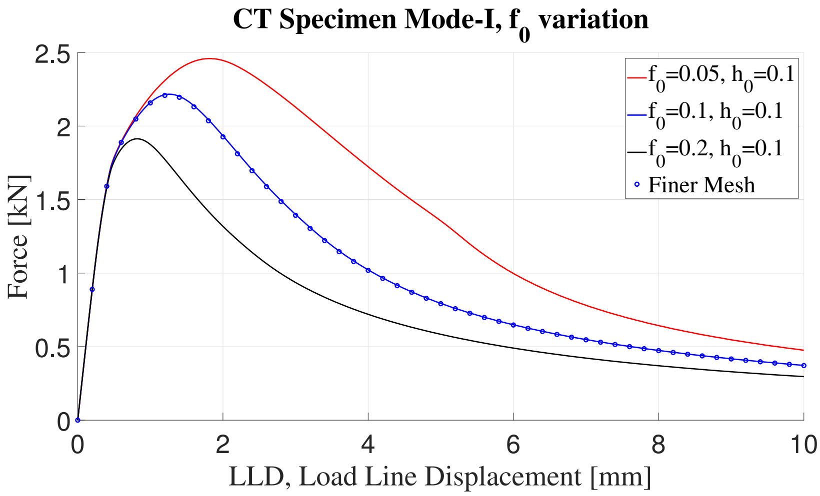

Figure 4.4: Force-LLD response for constant h_0, and changing f_0.

The effect of f_0 on ductility can be observed in Fig. 4.5, where distributions are shown at the same time increment. For the same global displacement, the crack propagates more for higher pore fraction, which can also be seen in Fig. 4.4. Therefore, when the initial pore fraction is smaller, the material is more ductile, and it can sustain more damage. Similarly, in Fig. 4.6, the equivalent plastic strain distribution is shown, and it is higher for lower initial pore fraction, which is a sign of ductility as well.

The effect of initial pore height, h_0, in the RVE is presented in Fig. 4.7 where the rate of softening is changed. For the low pore height, the speed at which traction carrying capacity drops is increased (see Fig. 2.3b or d). Remember the relation, $df/(1-f) = dh/h$, to see the effect of initial pore height. The smaller the height, the faster the pore fraction grows. Therefore, the failure occurs at an earlier time leading to lower toughness, which is similar to the effect of higher pore fraction. Physically, this is related to the pore shape effect. If h_0 is small, pore is crack-like and grows faster under normal loading.

There are several methods to quantify the resistance of a structure to crack growth. For example, in Linear Elastic Fracture Mechanics (LEFM), the stress intensity factor, K, or energy release rate, G, and their material-specific critical values can be used. In LEFM the plastic deformation is confined to a small zone ahead the crack tip. Therefore, the phenomenon is widely known as small scale yielding (SSY). And the stress intensity factor, K, can be used. However in the current work, the problems

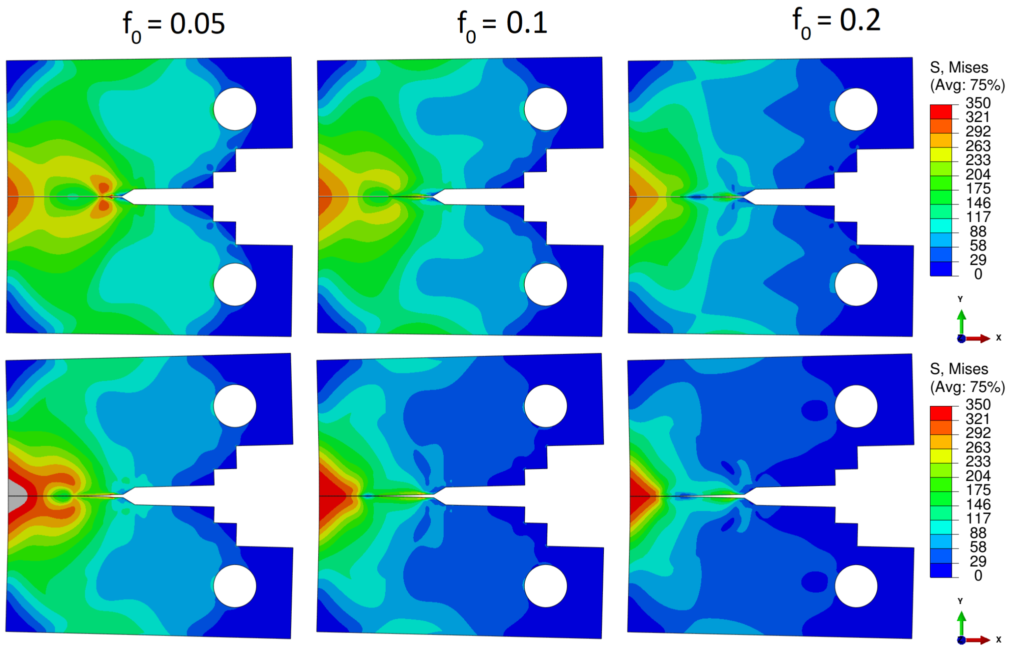

Figure 4.5: Stress distributions at the same time increment for different initial pore fractions. Load line displacement is 2 mm (top) and 4 mm (bottom).

include plasticity spread in a wide area of the specimen and this is called large scale yielding (LSY) phenomenon. In such cases path independent J-integral is introduced [103]. Path independence is lost if significant energy is spent to plastically deform material at the crack tip, as is the case in ductile fracture. A common observation is that J integral grows as the crack propagates, and when plotted versus crack extension, it can quantify resistance to crack growth [104]. This is the so-called crack growth resistance curve, R-curve or J-R curve. It is commonly used to characterize fracture toughness in ductile materials and represents fracture resistance behavior. Hence, it will be used here.

J-integral and crack extension Δa need to be calculated numerically to obtain the J-R curve. J-integral can easily be calculated in Abaqus by specifying its path, but calculating Δa is not straightforward with cohesive elements. In a cohesive zone model, crack propagation, and the fracture process zone is represented with a finite cohesive zone, and in this zone the crack tip location is not clear (Fig. 1.1). Li and Chandra [87] makes a discussion about this issue and identifies three points on the traction-separation law. Point A where traction becomes zero and complete material

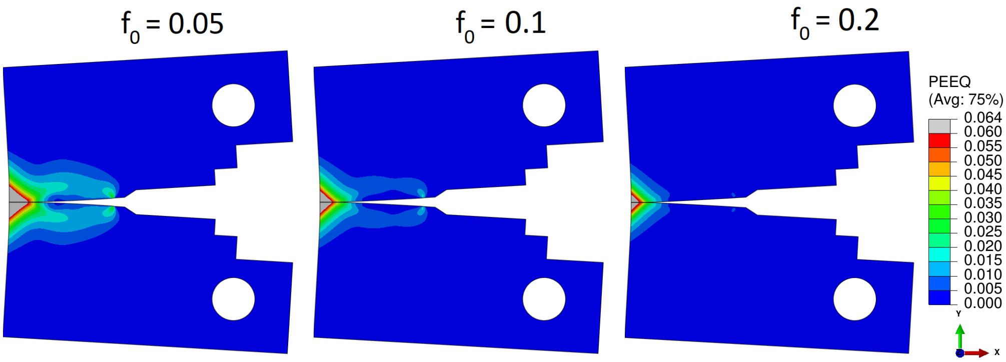

Figure 4.6: Equivalent plastic strain distributions for different initial pore fractions.

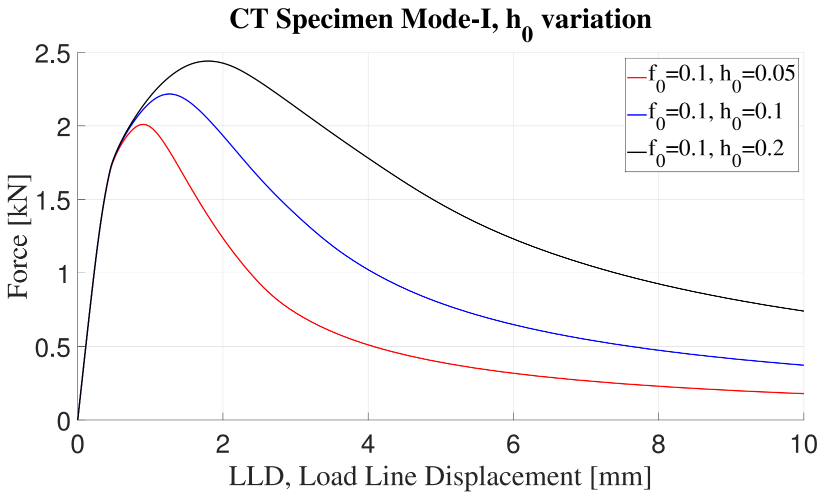

Figure 4.7: Force-LLD response for constant f_0, and changing h_0.

separation is achieved, point C where separation initiates, or point B where maximum traction is reached, Fig. 4.8. The region from point C to B is named as the forward region, and the region from B to A is named as wake region. They state that selecting point C implies absorbtion of entire cohesive energy by CZM, which excludes various plastic processes, e.g., cavitations damage, occurring in the immediate vicinity ahead of the crack tip in the wake region. On the other hand, selecting point A implies all of the energy required for the decohesion is absorbed by the fully separated crack with no active wake behind the crack tip. However, Ritchie [105, 106] showed that the micromechanical processes are active and consume energy both in the forward and wake regions of the crack. Therefore, they conclude that crack tip should be located at point B based on physical reasoning, so that will be followed.

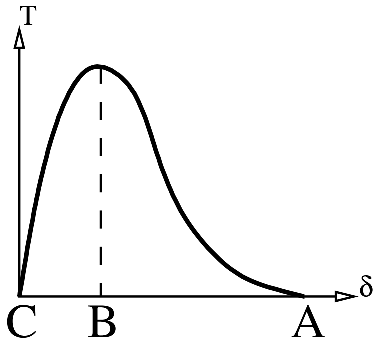

Figure 4.8: Potential points on TSL for crack tip.

With the crack tip selected, a Python script is written to calculate crack extension from Abaqus results. The separation at point B can be found by using,

$$\delta_{n,cr} = \frac{T_{n,max}}{E_n}.$$

In the script, the separation between each coincident node of a cohesive element is checked at every iteration. If this separation exceeds $\delta_{n,cr}$, then it is assumed that the crack tip has extended beyond this node couple. Then, separation in the neighboring coincident node couple is calculated where $\delta_{n,cr}$ is not exceeded yet. Linear interpolation is used to determine the crack tip location between these two node couples, and crack extension is calculated.

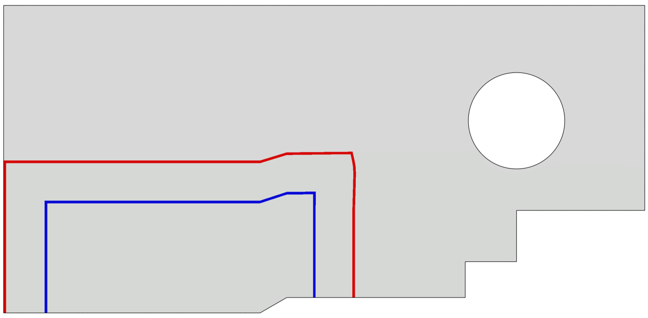

Figure 4.9: Paths used to calculate J integral. Innermost (blue) and outermost (red) paths are shown in the figure.

As mentioned before, J integral is path dependant in ductile fracture, and its path should be selected carefully. It should enclose any plastic deformation due to crack formation, the plastic zone at the crack tip. Since crack is propagating, this zone also moves and extends. Fig. 4.9 shows the innermost and outermost paths chosen in

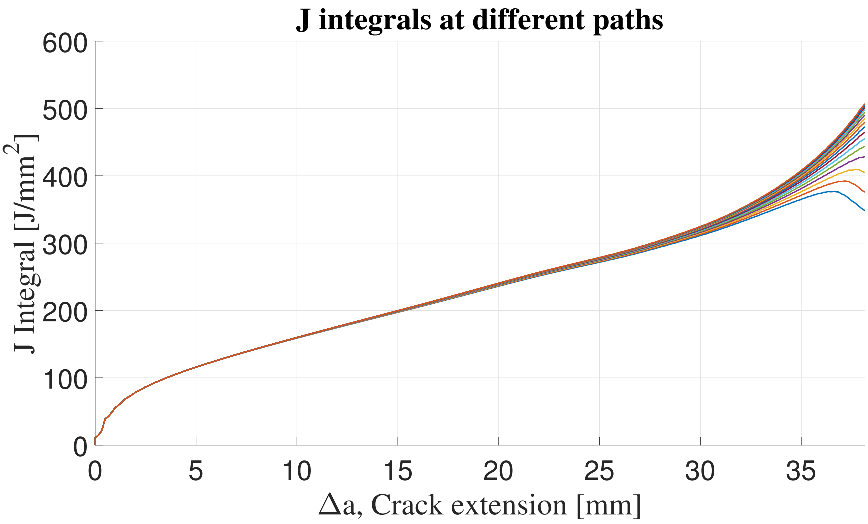

Figure 4.10: Path dependence of J integral for elasto-plastic models. $\sigma_y = 500$ MPa, $f_0 = 0.1$, $h_0 = 0.1$ mm.

Abaqus for J integral calculation with symmetry, and there are 14 paths in between, 16 in total.

Fig. 4.10 shows the resulting J integrals versus crack extension, where path dependence can be seen. J integral stops increasing when the crack grows outside of the region enclosed by J integral path. For this reason, the outermost path will be used to draw J-R curves.

Fig. 4.11 shows the change in resistance curve with initial porosity, f_0. Note that Δa has a maximum limit in plots according to ASTM-E1820 standards, and the J integral is only the initial region of J integral in Fig. 4.10. It can be seen that when f_0 is smaller, resistance to crack is higher, and this resistance increases faster. Initially, the energy required to grow the crack increases rapidly. Then as the crack propagates, the increase reaches a steady state.

In Fig. 4.12, h_0 is varied while f_0 is constant. Similar to force-displacement curves, h_0 has an opposite effect. However, there is a difference compared to Fig. 4.11 at the very beginning. The crack starts to grow at the same J value independent of h_0, while f_0 affects this critical J. This is because of the fact that crack starts to grow when maximum traction in the traction-separation law of MBCZM is reached, and maximum traction is a function of f_0 and σ_y, but not h_0.

J-R curve variation with σ_y is shown in Fig. 4.13. Similar to f_0, both the J required to initiate crack growth and the subsequent increase in resistance is affected. As it can be seen, σ_y had a much bigger impact on the J-R curve. When $\sigma_y = 100$ MPa, the resistance curve is almost flat, indicating that there is almost no ductile deformation.

Note that the preliminary results of this chapter is published in a conference proceeding (Yalcinkaya et al. [3]). The work is extended here using another CT specimen and by conducting a more through investigation including J-R curve analysis.

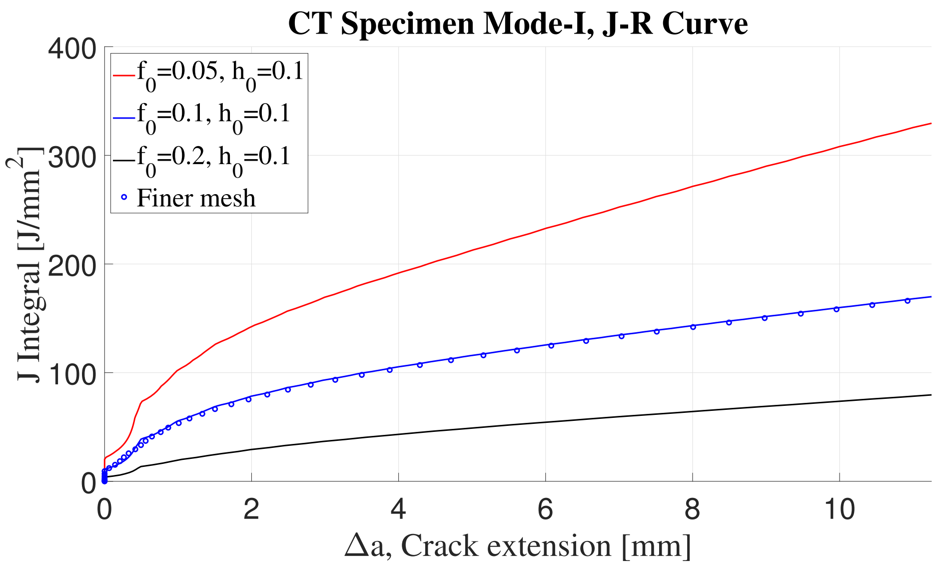

Figure 4.11: J-R curve for constant h_0, and changing f_0.

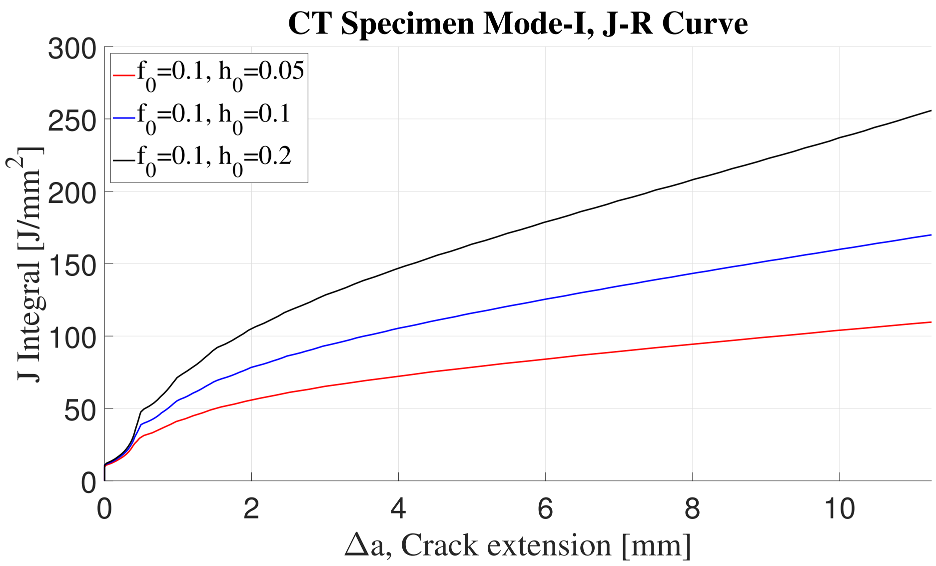

Figure 4.12: J-R curve constant f_0, and changing h_0.

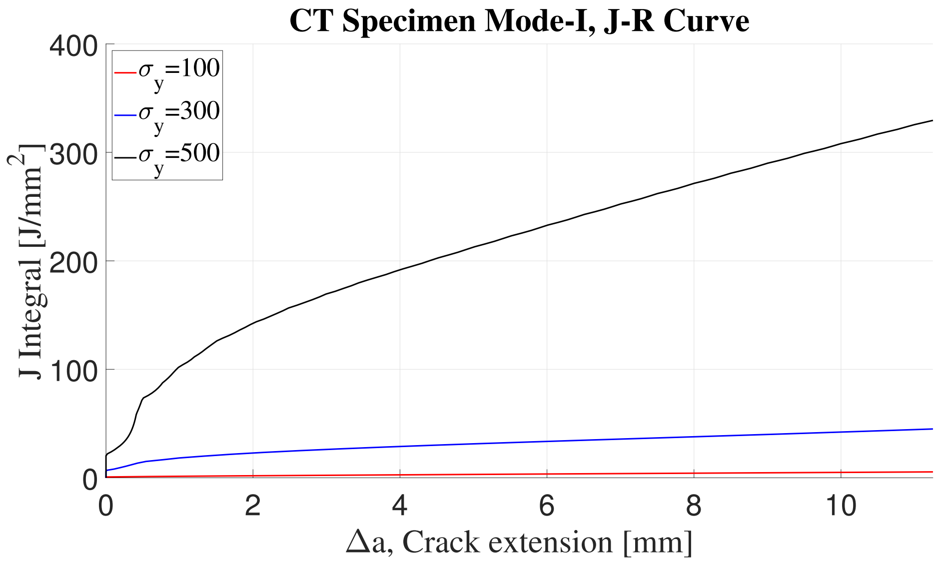

Figure 4.13: J-R curve changing σ_y.

4.3 SEN Specimen for Mixed-Mode Ductile Failure Analysis

In this section, a Single Edge Notch (SEN) specimen is used as a test specimen in FE simulations to illustrate the performance of the developed micromechanics based cohesive zone model under mode-I, mode-II and mixed-mode loading conditions. The specimen's material is the same as the previous CT specimen example, the SS316 austenitic steel presented in Fig. 4.1. A schematic of the dimensions of the SEN specimen is given in Fig. 4.14. The dimensions are as follows: $L = 100mm, h = 20mm, b = 20mm, a_0 = 10mm$. The holes are used to load the specimen in an experimental setup, but they are included in the FE model for the sake of accuracy.

Cohesive elements are placed ahead of the initial crack to simulate crack propagation.

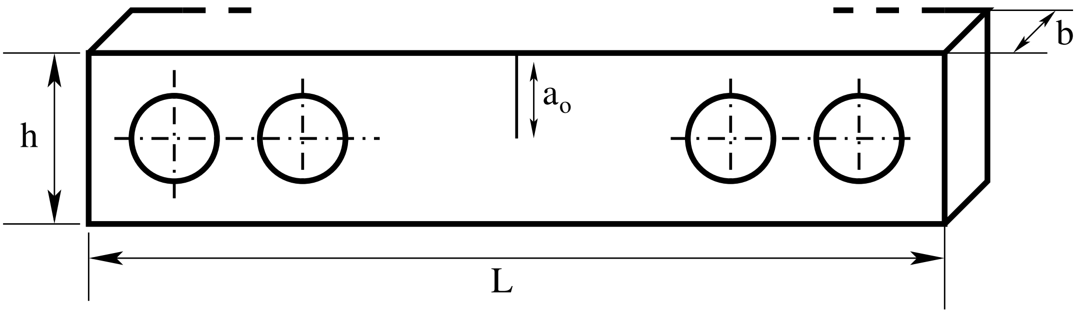

Figure 4.14: Single edge notch (SEN) specimen geometry.

The micromechanics based cohesive zone model developed in the previous chapters is used as the constitutive model of cohesive elements. Differently from the CT specimen, mixed-mode implementation of the MBCZM is used instead of analytical implementation.

In order to load the SEN specimen under mode-II and mixed-mode conditions, a test apparatus developed by Davenport and Smith [4] is employed, see Fig.4.15. It is an extension of the mode-II single punch shear test to the mixed-mode. When elastic-plastic material is subjected to mode-II loading, plastic flow can be observed at the crack tip, which may introduce a mode-I stress component. This effect can be reduced by the constraints of the test apparatus, allowing pure mode-II loading. The apparatus clamps together around the specimen, completely surrounding it. The clamps are tightened so that there is no relative movement between the apparatus and spec-

imen. This configuration makes sure that the crack tip is at the center of the applied load. With this apparatus, a conventional tensile test machine and a simple single edge notch specimen are adequate to apply mode-I, mode-II and mixed-mode loading. This is achieved simply by applying the load through holes, see Fig.4.15: Mode-I -> 1, Mode-II -> 6, or Mixed-Mode -> 2-5. The mode mixity changes depending on which hole is used between 2-5.
In this numerical study, the test setup is modeled as a 2D FE model, see Fig. 4.16.

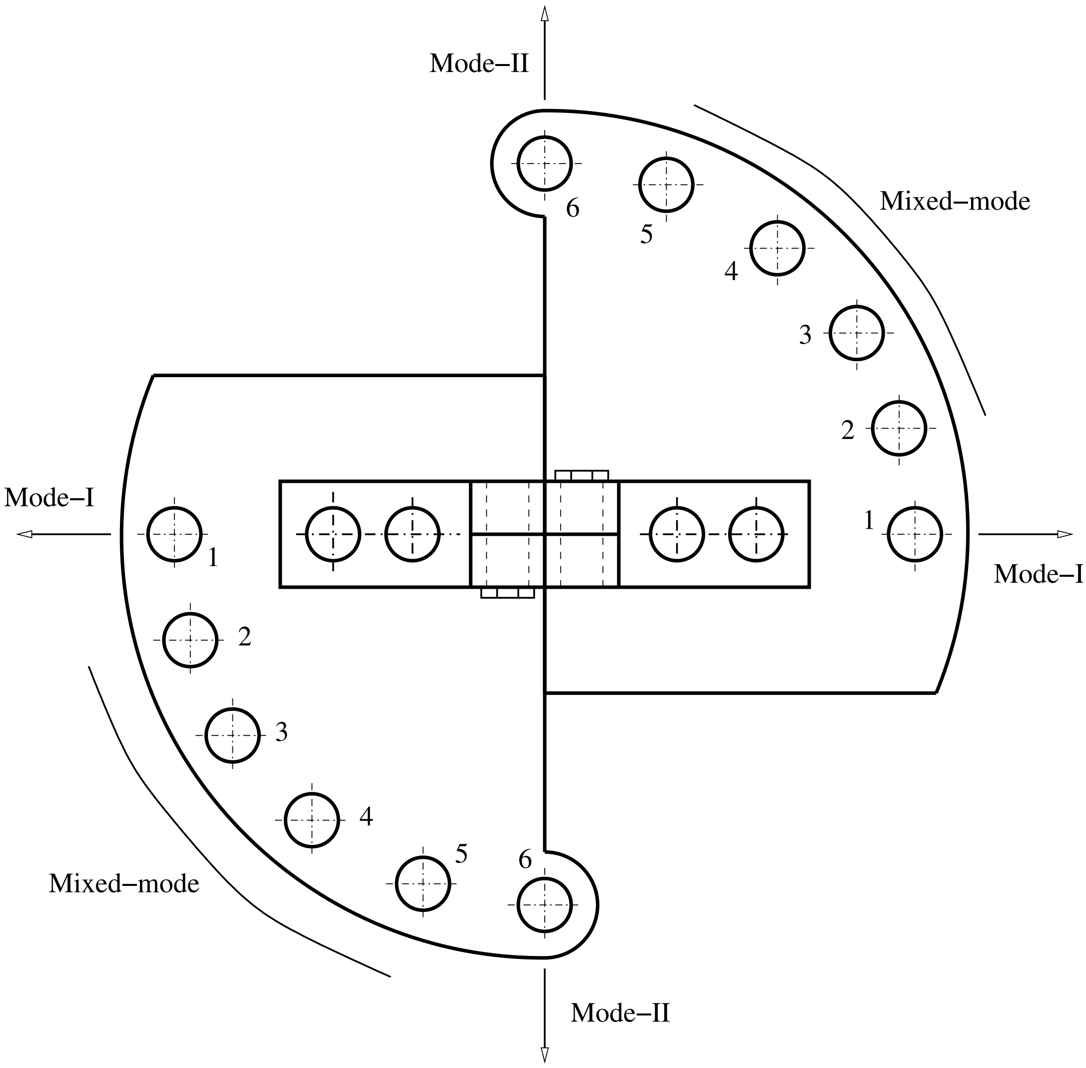

Figure 4.15: Test apparatus used to load SEN specimen with mode-I, mode-II and mixed-mode loading [4].

The outside apparatus is modelled with rigid elements, and for the SEN specimen, plane strain elements are used since the width is sufficiently large. The clamping ef-

fect is achieved by defining a high friction coefficient, $\mu = 1.3.$, between the rigid part and SEN, to prevent any slip (cast iron has a static friction coefficient of 1.1, and for aluminum its between 1.05-1.35 [107]). There are also rigid parts in the SEN specimen's loading holes, whose movement are directly coupled with the rigid part outside, so they must move together.
In Fig. 4.17, the mesh of the SEN specimen is shown. The crack tip's close-up is

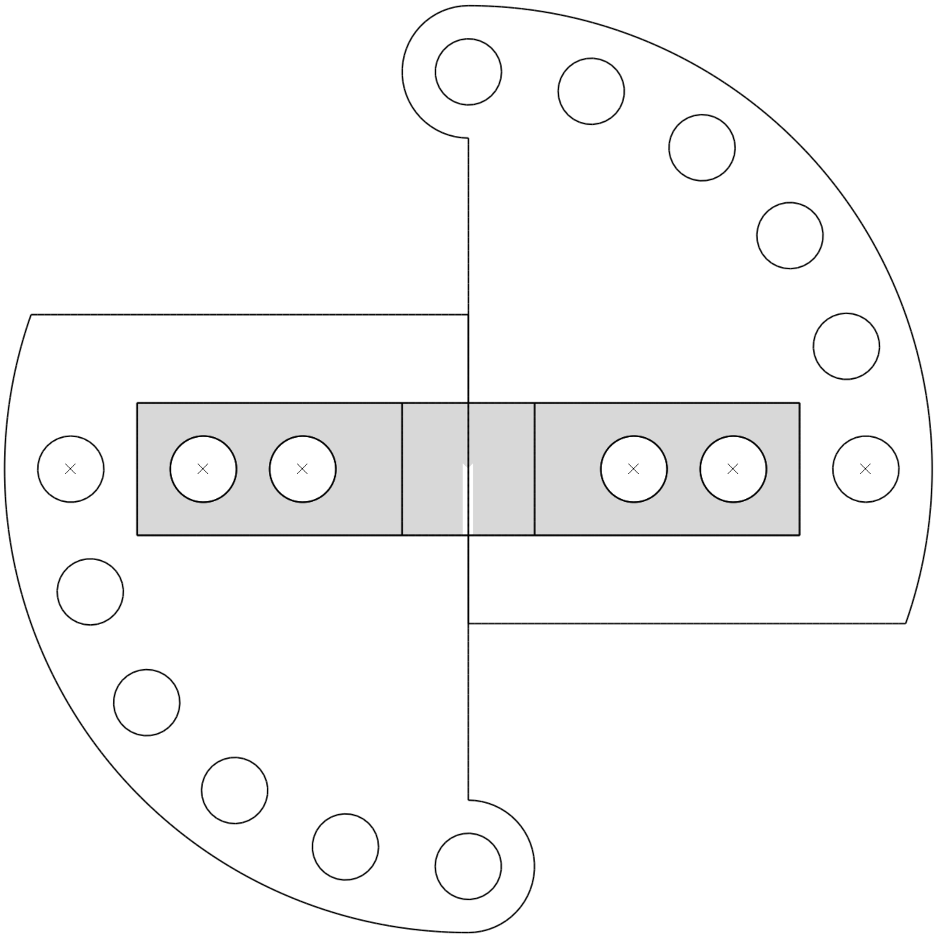

Figure 4.16: FE model of the test apparatus in Fig. 4.15.

shown in the same figure, where red crosses are cohesive elements. There are 47348 nodes and 46180 elements. A finer mesh is used near the crack region, and the approximate global element size is 0.1, while it is 0.5 in the outer region. In order to study mesh dependency, the outer region size is reduced to 0.25, and crack region element size is reduced to 0.075. It is confirmed that there is not an essential difference in results.

In the following subsections results for mode-I and mode-II loadings are presented.

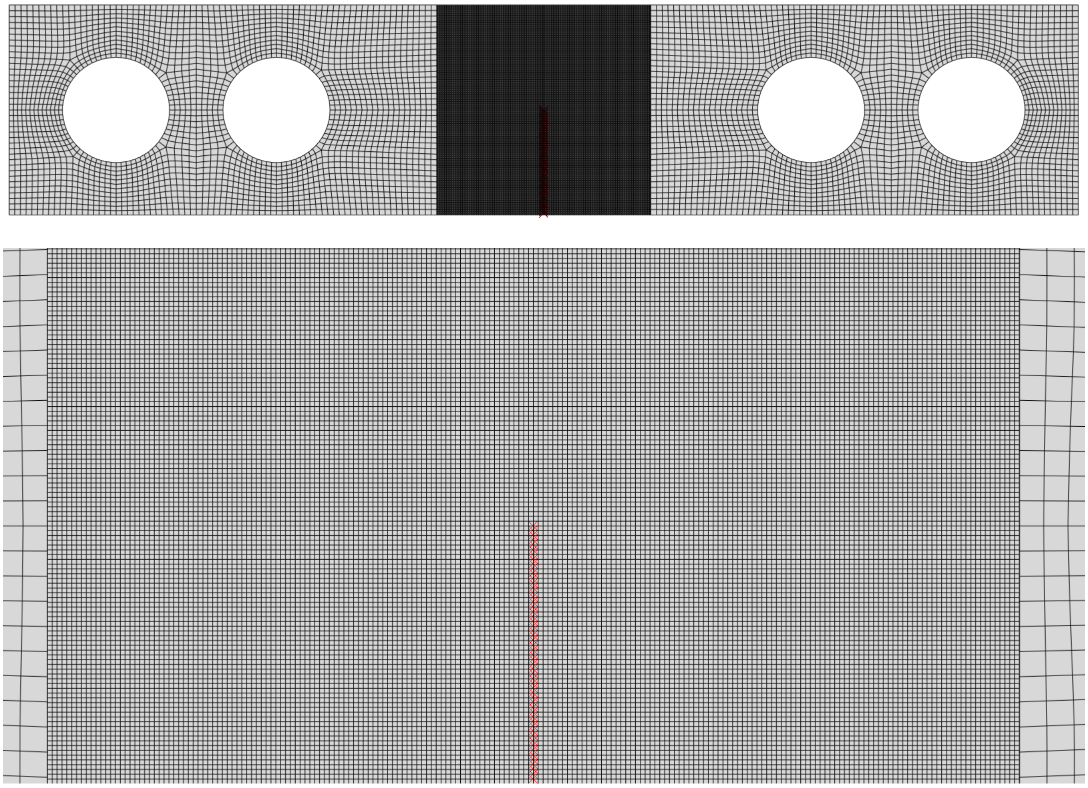

Figure 4.17: Mesh of the SEN specimen and close-up view of crack tip region.

4.3.1 Mode-I Loading

The previously discussed SEN specimen is subjected to mode-I loading by using hole number 1. Similar to the CT specimen, the effect of initial pore fraction f_0 and initial pore height h_0 is investigated. It is also checked if the mode-II related pore spacing parameter, l, has any effect on results.

The observations here are mostly similar to the Mode-I CT specimen example. This example is included for the sake of variety, and it provides a different point of view. In addition, detailed insights are included in the discussion.

In Fig. 4.18 force versus displacement curve is plotted for different initial pore fractions. Force is the total reaction force in the x-axis obtained from hole 1 at one side where the displacement boundary condition was given. Similarly, displacement is the total displacement of holes in the x-axis. In order to check if there is any mesh de-

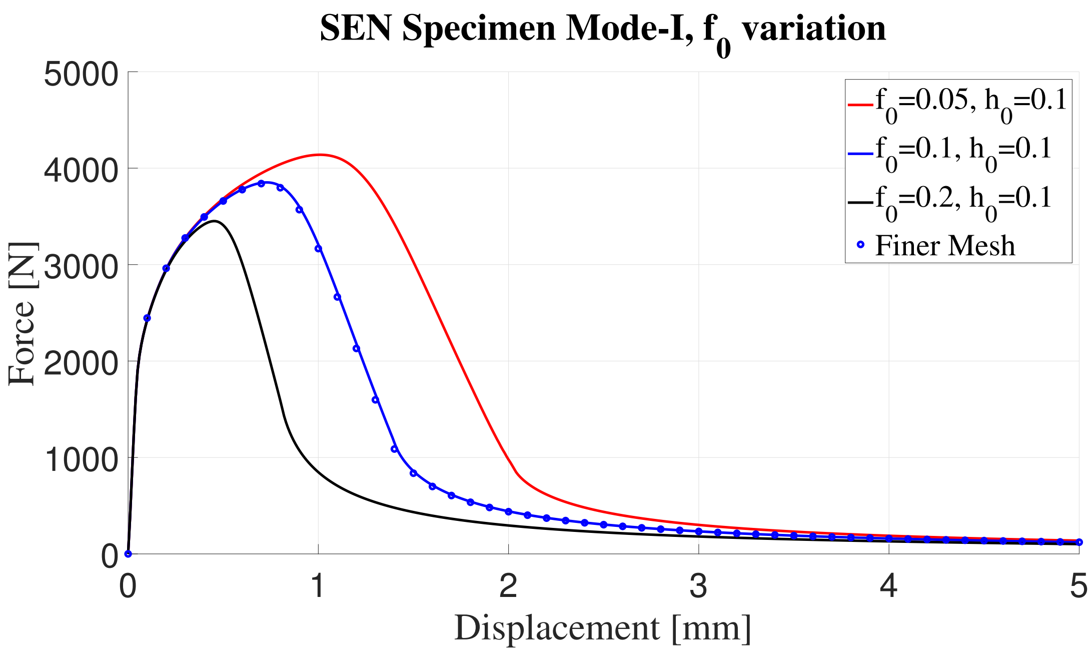

Figure 4.18: Force displacement response under mode-I loading for changing initial pore fraction, f_0.

pendency, a finer mesh is used for the $f_0 = 0.1, h_0 = 0.1$ case to compare. It can be seen that results are almost the same, so the mesh is sufficiently fine.

Next, Fig. 4.18 is analyzed in detail together with contour plots. At first glance, it can be deduced that this is a ductile fracture force-displacement curve. Notice the three main regions in the curves. First, there is a tiny linear elastic region at small displacements. Next, there is a non-linear hardening region until the peak force is reached. Finally, there is a softening and failure region.

In the non-linear hardening region, ductile deformation occurs in the specimen, and the size of this region is bigger if the initial pore fraction f_0 is smaller, meaning ductility is increased. This is supported by Fig. 4.19, where equivalent plastic strain contours are plotted at the final time increment. It is evident from contours, even visible to the naked eye that permanent deformation increases with decreasing initial pore fraction because accumulated plastic strain increases. Why this behavior occurs, why there is a ductile deformation region? It is known that there are cohesive elements ahead of the crack, and their faces separate under loading similar to a crack. However, this separation does not initiate if maximum traction is not reached at a cohesive element. Moreover, this maximum traction is determined by the traction-separation

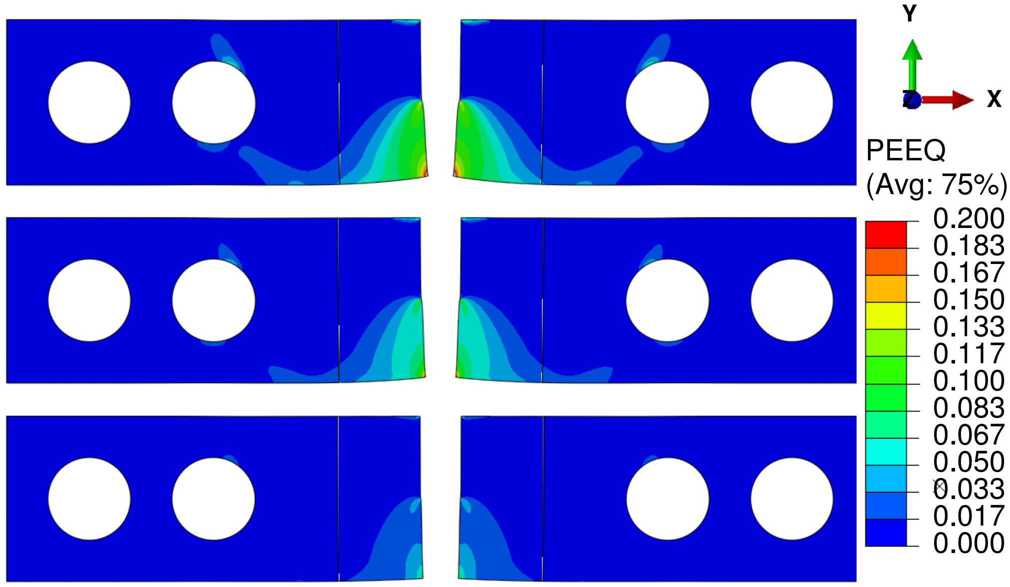

Figure 4.19: Equivalent plastic strain after failure. f_0's are equal to: 0.05 (top), 0.1 (middle), 0.2 (bottom).

law of cohesive element, which is dependant on the initial pore fraction, f_0. If cohesive faces cannot separate, then the deformation is carried by the specimen, and if maximum traction is high enough so that the yield stress of bulk material is exceeded at a point in the specimen, plastic deformation occurs. This behavior is consistent with a physical pore. If the initial pore size is small, then more deformation would be required to grow the pores until coalescence and failure, which in turn results in a more ductile material.

Going back to Fig. 4.18, notice the peak force points. It is clear that the maximum force reached is higher for smaller f_0 values. This means that with smaller initial pore fraction, not only ductility but also the strength of the material increases, which again agrees with the physical pore growth-coalescence mechanism. This observation is supported by Figs. 4.20 and 4.21, where von Mises stress and normal stress in loading direction contours are plotted at the peak force point of Fig. 4.18. It can be observed that there is barely any crack propagation, and the stresses at the crack tip are higher for smaller f_0, which is a sign of strength.

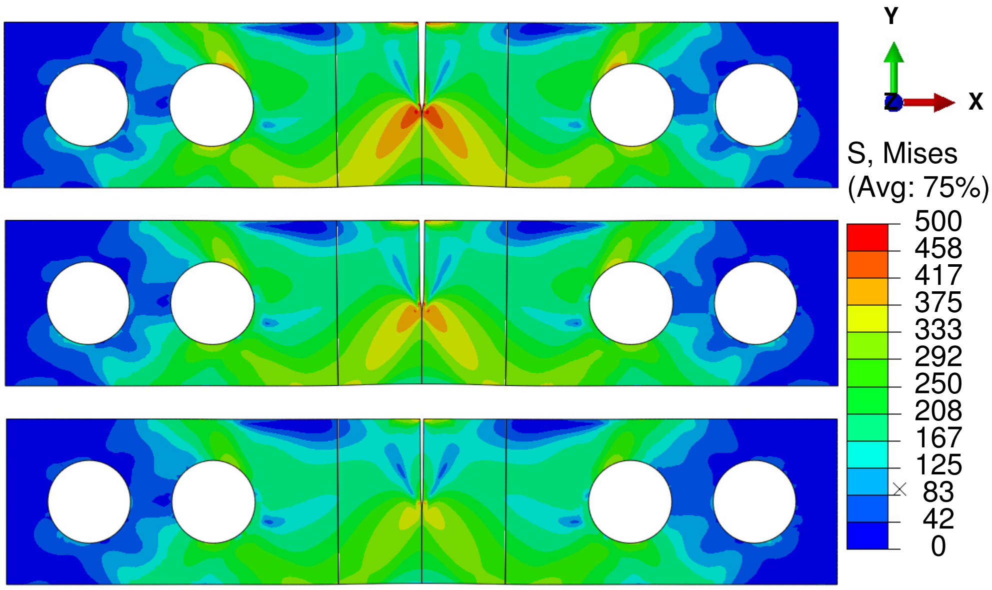

Figure 4.20: Von Mises stress contours just before softening begins. f_0's are equal to: 0.05 (top), 0.1 (middle), 0.2 (bottom).

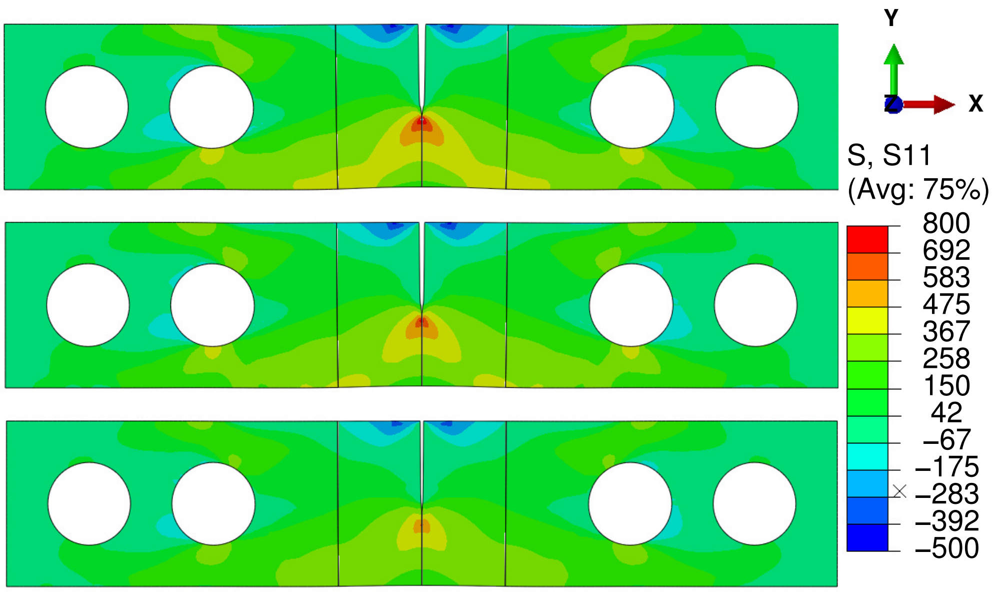

Figure 4.21: S_{xx} stress component, just before softening begins. f_0's are equal to: 0.05 (top), 0.1 (middle), 0.2 (bottom).

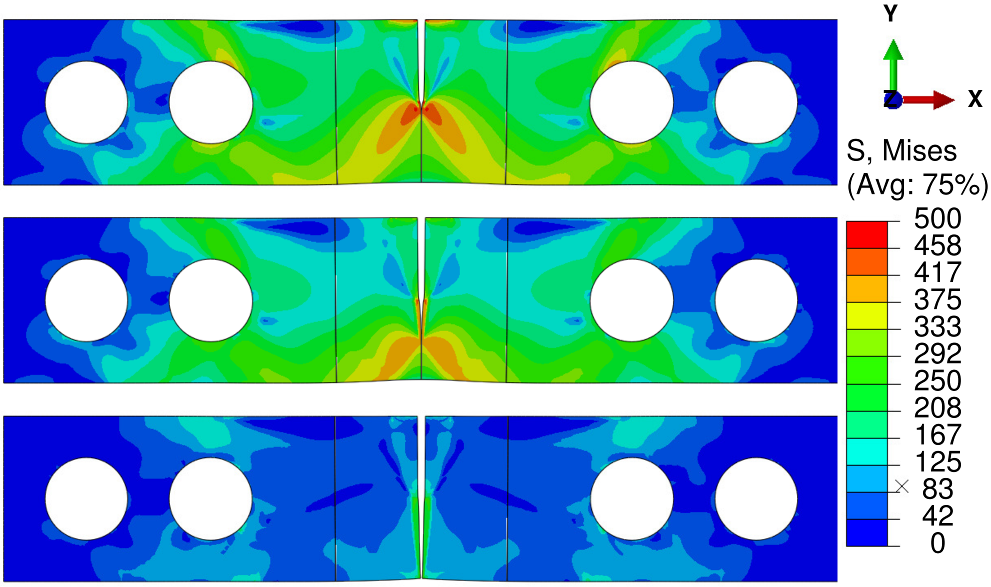

Figure 4.22: Von Mises stress at the same displacement, $1mm$. f_0's are equal to: 0.05 (top), 0.1 (middle), 0.2 (bottom).

Since the strength and ductility of the material increased, it may be said that toughness is increased as a consequence. This can be measured by the area under force-displacement curves in Fig. 4.18. Also, in Fig. 4.22, von Mises stress is plotted at the same displacement value, $1mm$. Notice that the case with $f_0 = 0.05$ is still undergoing plastic deformation and hardening, in $f_0 = 0.1$ case, crack is propagating and there is softening, and finally, in $f_0 = 0.2$ case, the crack fully propagated, and the specimen has lost its stress carrying capacity. This is a sign of increased strength, ductility, and toughness of the material with smaller initial pore fraction.

Next in Fig. 4.23, force versus displacement curve is plotted for different initial pore heights. It can be seen that the change in behavior is very similar to Fig. 4.18. Strength, ductility and toughness increase with higher pore cavity height. The increase in strength is visible in Fig. 4.24 von Mises contour plot, and ductility increase is clear in Fig. 4.25 equivalent plastic strain contours. However, what does initial pore height mean, and why does it have such an effect?

Back in Chapter 2, pore height h is defined as the height of the cylindrical cavity in a cylindrical RVE. Under mode-I loading, this cavity grows both in circumference and

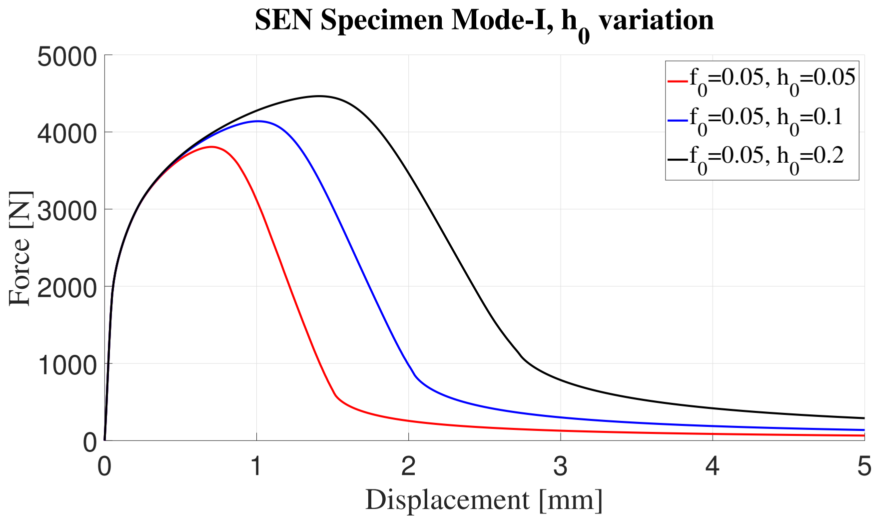

Figure 4.23: Force displacement response under mode-I loading for changing initial pore height, h_0.

in height. Of course, this is an idealization of the real case. In reality, it is generally assumed that physical pores initially have a spherical shape. However, when they grow under plastic deformation, they also change their shape depending on loading mode and triaxiality [108]. They may become more like an ellipsoid shape with a longer major axis and shorter minor axis in 2D. In our model here, pore height h is an idealized way to represent this ellipsoid shape of a growing pore. During derivation, eventually, the evolution equation $df = dh(1-f)/h$ was obtained for mode-I, which translates to accelerated growth of pore fraction f for smaller pore height h. Thinking physically, if the pore height is small, it has a crack like shape, and it would be easier to grow it under mode-I loading. As this initial height increases, it starts to hinder growth in that direction. So, naturally this h_0 parameters has an opposite effect of f_0 parameters since it directly affects pore growth, the evolution of f.

Why does the strength increase while maximum traction is not affected by h_0?. This may be the case for a single cohesive element, but there are multiple cohesive elements in this example, each in a different situation. Even though the maximum traction does not increase, the range of displacement corresponding to high tractions increases depending on h_0, see Fig. 2.3. This, together with the fact that there are multiple elements, result in a change in strength.

In Fig. 4.26, the effect of pore spacing l on mode-I force-displacement curve is in-

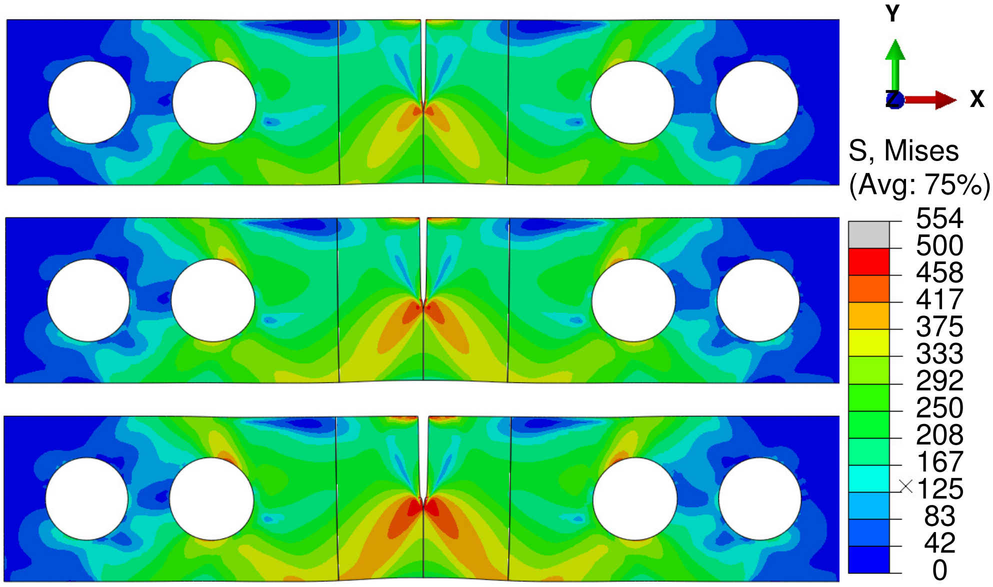

Figure 4.24: Von Mises stress contours just before softening begins. h_0's are equal to: 0.05 (top), 0.1 (middle), 0.2 (bottom).

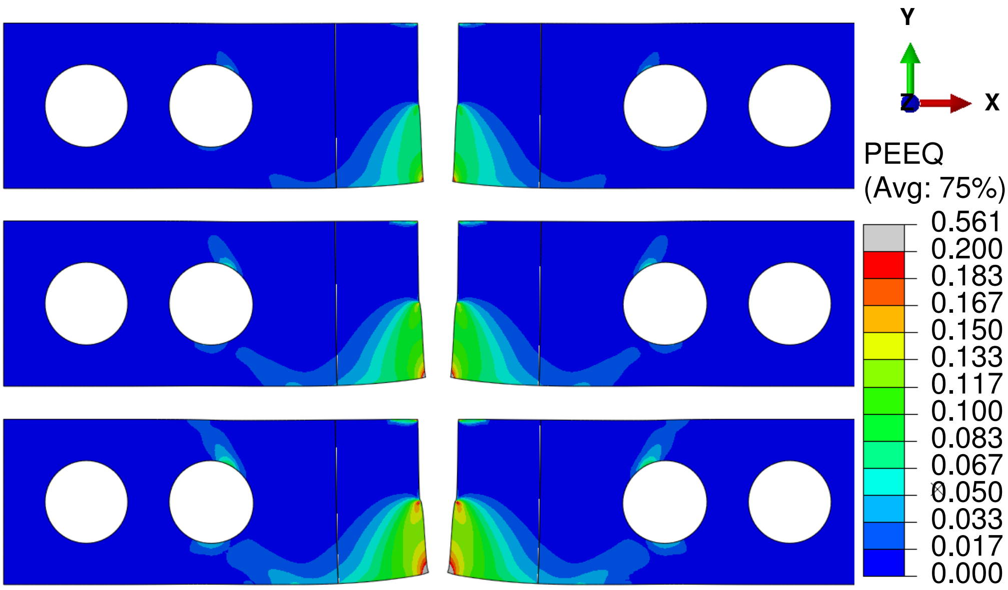

Figure 4.25: Equivalent plastic strain after failure. h_0's are equal to: 0.05 (top), 0.1 (middle), 0.2 (bottom).

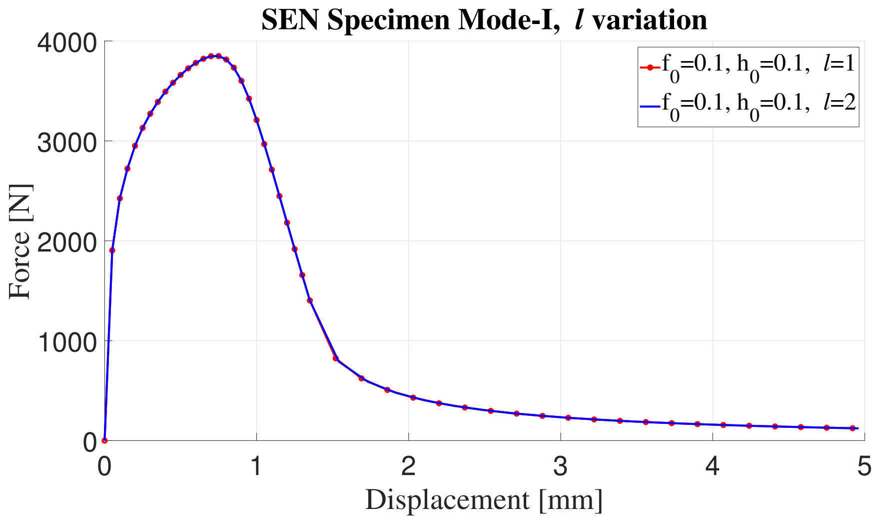

Figure 4.26: Force displacement response under mode-I loading for changing pore spacing, l.

vestigated. It is expected to have no effect on a pure mode-I loading since it is related to mode-II fracture energy. The expectations are met, and this is evidence that the loading is indeed pure mode-I.

Notice that in Figs. 4.18, 4.23 and 4.26, the force does not reach zero, but it goes to zero asymptotically at infinite displacement. This is a shortcoming of the derived model under pure mode-I loading. Full failure cannot be modelled, as evidenced by the normal traction figure 2.3. As it will be seen in the next section, this is not the case under mode-II loading.

In Fig. 4.27, variation of σ_y parameter on force-displacement curve is shown. This σ_y is a parameter in the cohesive zone model, not to be confused with material's yield strength, and it affects maximum tractions. Decreasing σ_y decreases the maximum tractions in CZM, hence reduces the maximum hardening achievable by the material. Therefore, when σ_y is small, the problem becomes a small scale yielding problem since fracture starts without plastic zone spreading throughout the specimen resulting in elastic fracture. From this point of view, it has the opposite effect of a material yield point. For example, when $\sigma_y = 100MPa$, the ductile deformation zone is non-existent in Fig. 4.27. Similarly, there is no plastic deformation in Fig. 4.28, and brittle fracture is observed.

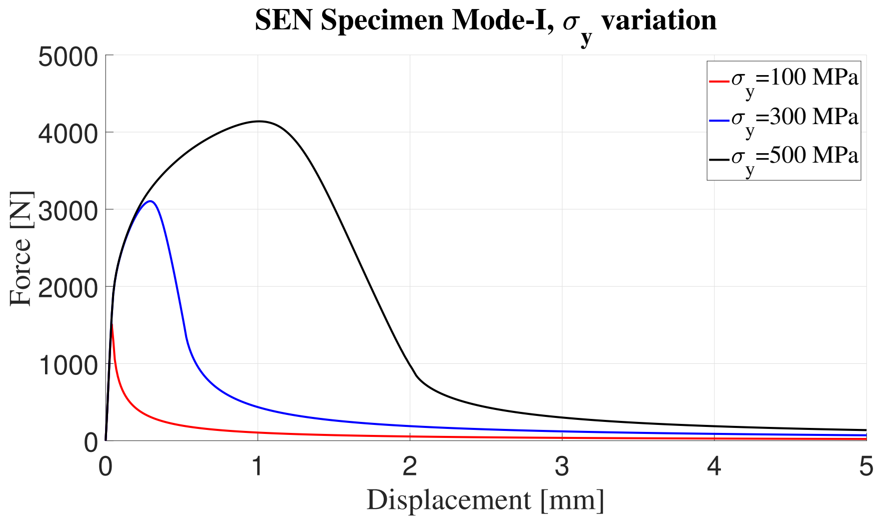

Figure 4.27: Force displacement response under mode-I loading for changing yield stress, σ_y.

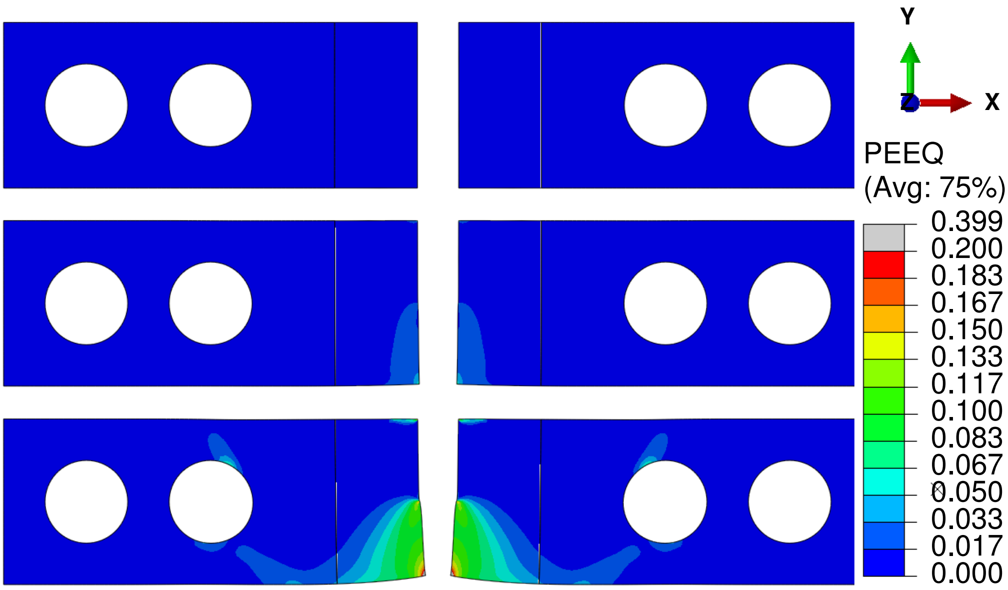

Figure 4.28: Equivalent plastic strain after failure. σ_y's are equal to: 100 MPa (top), 300 MPa (middle), 500 MPa (bottom).

4.3.2 Mode-II Loading

Next, the SEN specimen is subjected to mode-II loading by using hole number 6. Similarly, the effect of initial pore fraction f_0 and pore spacing l is investigated. In addition, it is checked if the mode-I related initial pore height parameter, h_0, has any effect on results.

In Fig. 4.29 force versus displacement curve is plotted for different initial pore fractions. Force is the total reaction force in the y-axis obtained from hole 6 at one side where the displacement boundary condition was given. Similarly, displacement is the total displacement of holes in the y-axis.

Compared to mode-I loading, similar deductions can be made for mode-II loading

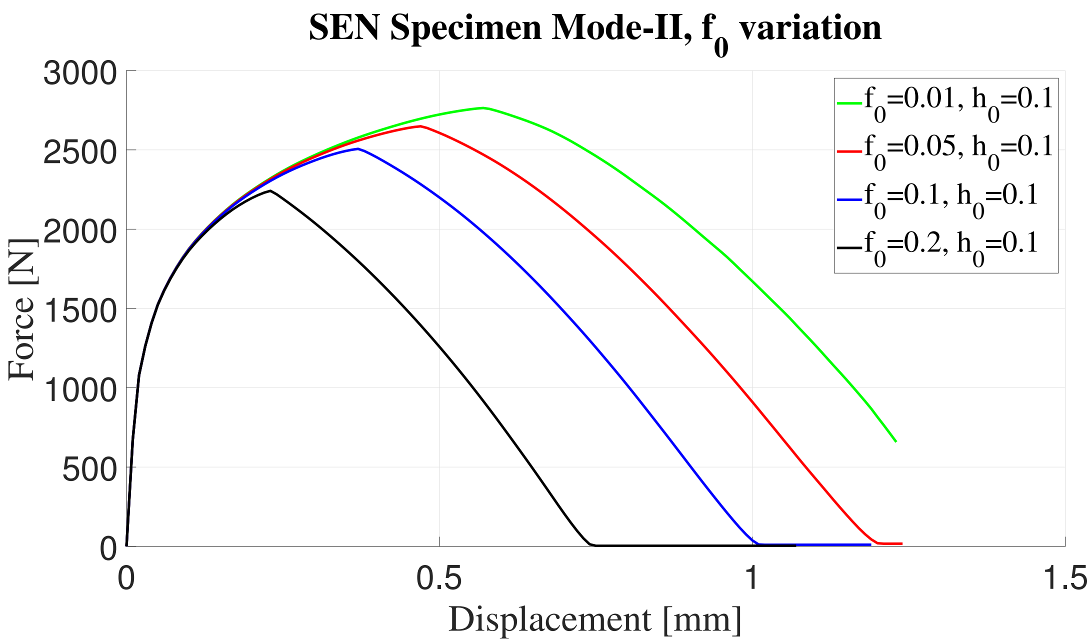

Figure 4.29: Force displacement response under mode-II loading for changing initial pore fraction, f_0.

in terms of strength, ductility, and toughness evolution with changing initial pore fraction, f_0, see Fig 4.29, i.e., they all increase with decreasing initial pore fraction. However, there are some differences. Firstly, unlike pure mode-I, the force can become zero after a finite displacement, and this failure separation is dependant on the initial pore fraction. Secondly, as f_0 gets smaller, its effect on macroscopic behavior is less effective. For example, the change in strength is smaller when f_0 goes from 0.1

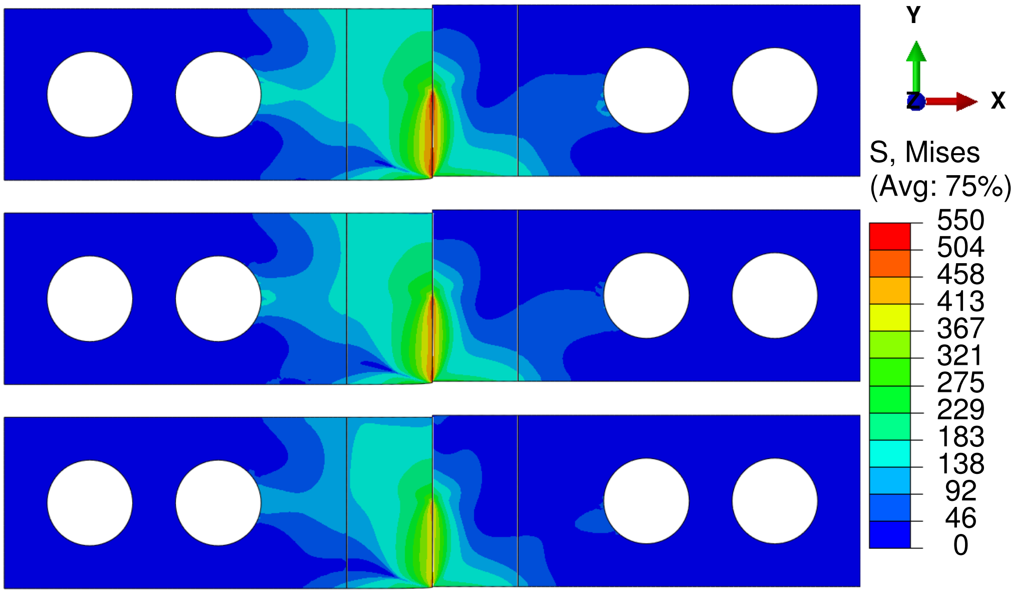

Figure 4.30: Von Mises stress contours just before softening begins.
f_0's are equal to: 0.05 (top), 0.1 (middle), 0.2 (bottom).

to 0.05 compared to going from 0.2 to 0.1, which was not the case for mode-I loading. The reason can be found in traction-separation relations for mode-I and mode-II. Remember maximum traction equations, 3.16, from Chapter 2,

$$T_{n,max} = \sigma_y \left[(1-f_0)^2 + \left(\frac{1}{\sqrt{3}} ln \frac{1}{f_0} \right)^2 \right]^{\frac{1}{2}} \quad \text{and} \quad T_{t,max} = \frac{\sigma_y}{\sqrt{3}} [1-f_0]$$

Notice that if f_0 goes to zero, $T_{n,max}$ becomes infinity, whereas $T_{t,max}$ has a finite value. Therefore, there is a limit to the effect of the initial pore fraction for mode-II loading. Still, with the value given here, the difference in strength is visible with stress contours in Figs. 4.30, 4.31 and 4.32, von Mises stress, normal stress and shear stress respectively. Also, the change in ductility can be seen in Fig. 4.33 with equivalent plastic strain. Note that in Fig. 4.31 there is a stress concentration at the bottom tip of the right half of the SEN specimen. This happens because the right half of the outer mechanism pulls the specimen upwards while the other half pulls it downwards.

In Fig. 4.34, von Mises stress is given at the same displacement, $0.5mm$. All of the cases are in the softening region, $f_0 = 0.2$ barely resist load while $f_0 = 0.1$ and

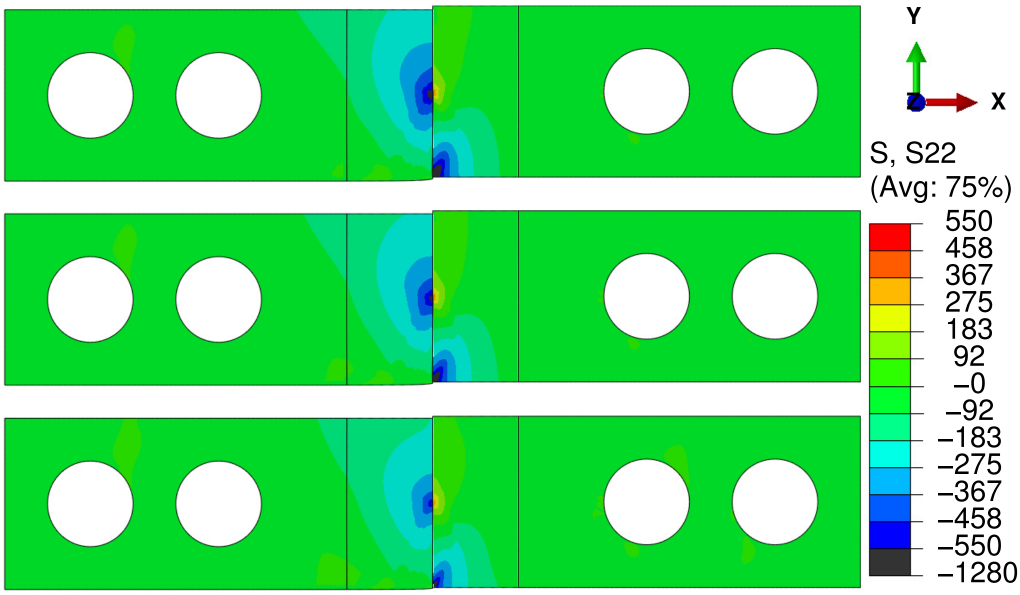

Figure 4.31: S_{yy} stress component, just before softening begins. f_0's are equal to: 0.05 (top), 0.1 (middle), 0.2 (bottom).

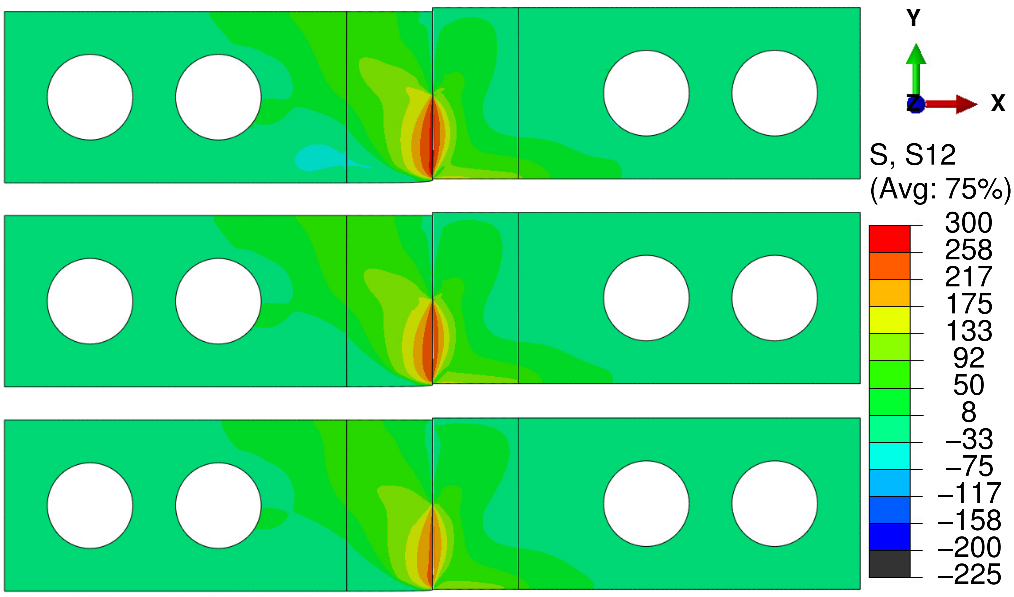

Figure 4.32: S_{xy}, stress component, just before softening begins. f_0's are equal to: 0.05 (top), 0.1 (middle), 0.2 (bottom).

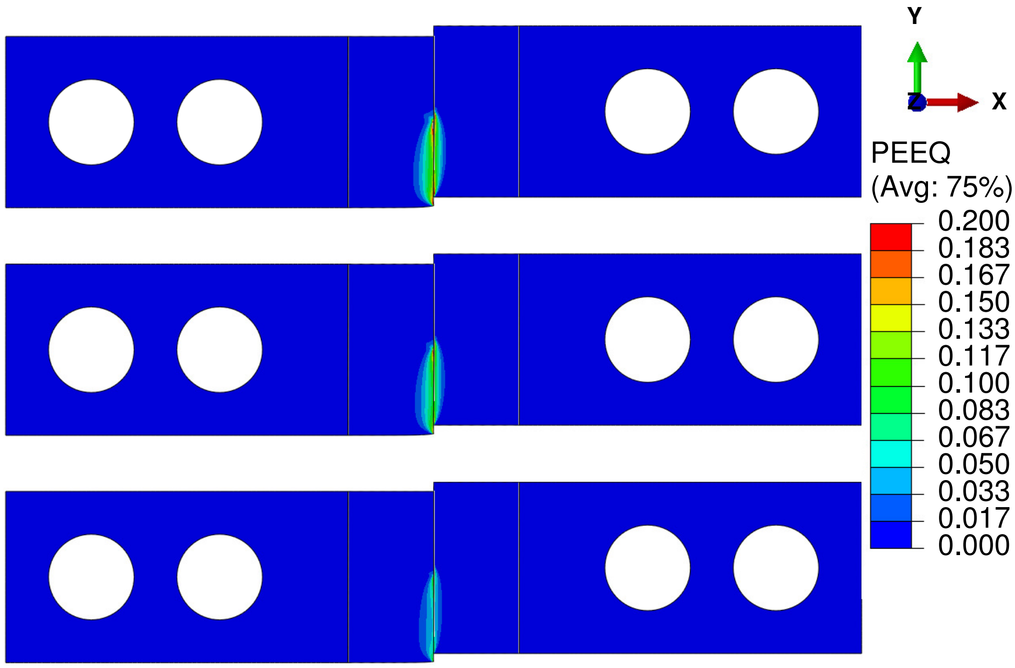

Figure 4.33: Equivalent plastic strain after failure. f_0's are equal to: 0.05 (top), 0.1 (middle), 0.2 (bottom).

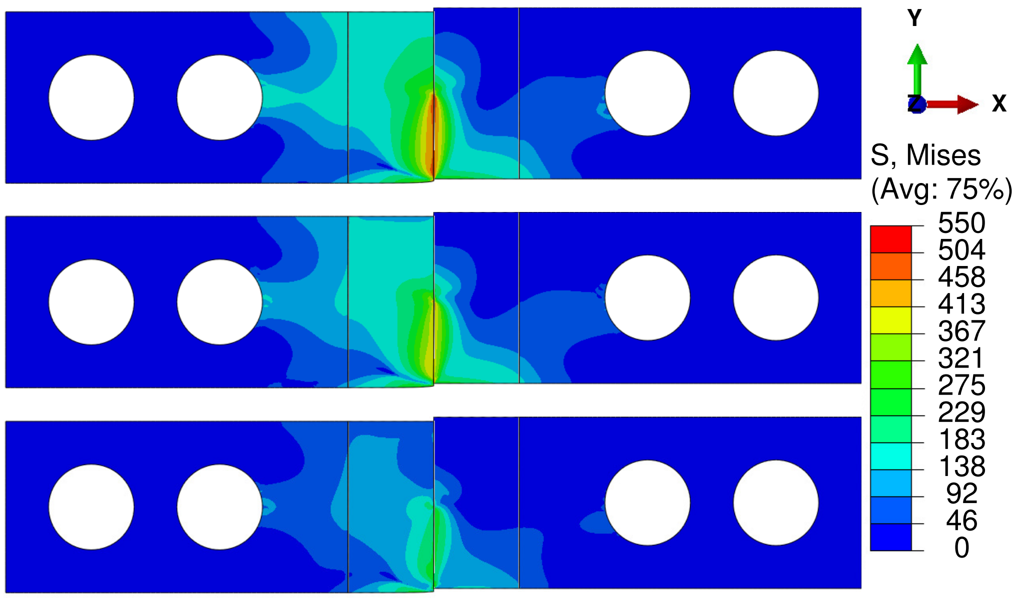

Figure 4.34: Von Mises stress at the same displacement, $0.5mm$. f_0's are equal to: 0.05 (top), 0.1 (middle), 0.2 (bottom).

$f_0 = 0.05$ cases still carry some load, where the latter does so more. At this point, crack is propagating to cause full fracture eventually.

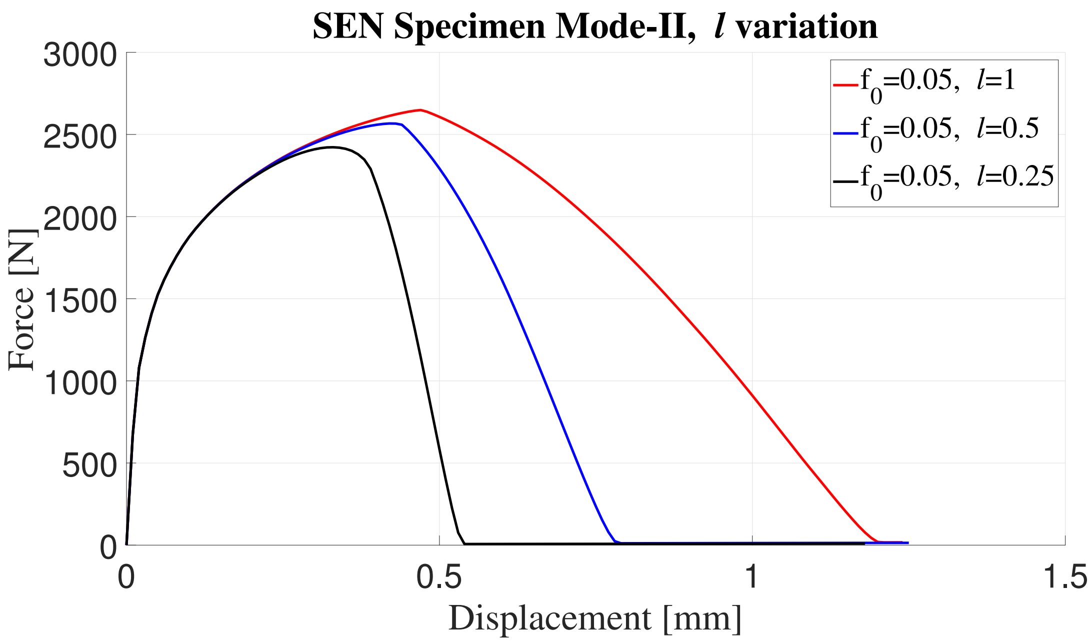

Figure 4.35: Force displacement response under mode-II loading for changing pore spacing, l.

In Fig. 4.35, the effect of pore spacing, l, is checked. This parameter is effective only on mode-II traction-separation law. It does not affect maximum traction, but it affects final failure separation. Hence, it naturally affects mode-II fracture energy, the area under the traction-separation curve. This effect is translated into macroscopic force-displacement behavior. Similar to the effect of h_0 on the mode-I case, l affects the specimen's strength even though it does not change maximum traction. Again, this is due to the fact that the interactions are more complex with multiple cohesive elements, and the range of separation where tractions are high is bigger if l is bigger, see Fig. 2.6 in Chapter 2. The increase in toughness observed with bigger l may be imagined physically. So in a real material, ductile fracture happens by the nucleation, growth and coalescence of pores. If the distance between different pores is increased, which is like increasing pore spacing l, then it would take more plastic deformation for coalescence to occur. Hence, strength, ductility and toughness increase. Figs. 4.35 and 4.36 support this discussion. However, as can be seen in the force-displacement curve and plastic strain contours in Fig. 4.37, the effect of l on ductility is not as

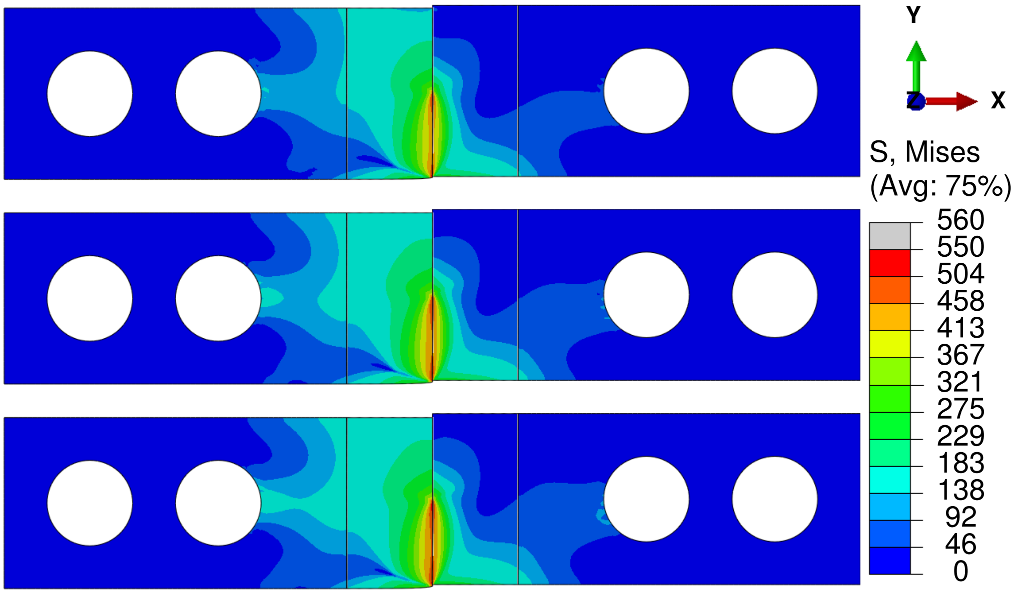

Figure 4.36: Von Mises stress contours just before softening begins.
l's are equal to: 0.25 (top), 0.5 (middle), 1 (bottom).

strong as f_0. Like h_0 for mode-I, l parameter heavily affects the softening region's shape and controls mode-II fracture energy.

Finally, in Fig. 4.38, the effect of initial pore height h_0 on mode-II loading is shown. Remember that normally, this parameter only affects mode-I traction-separation law. The small change in the force-displacement curve's softening region suggests that there is a small mode-I loading included. The plastically deformed region may be subject to some mode-I loading due to the rotation of elements. However, this effect is minimal, as evidenced by Fig. 4.38, and the example is very close to a pure mode-II. This also indicates that mixed-mode formulation is working as intended.

In Fig. 4.39, variation of σ_y parameter on force displacement curve is shown. The observations in mode-I apply to mode-II. When $\sigma_y = 100MPa$, brittle failure is observed, see Fig. 4.40.

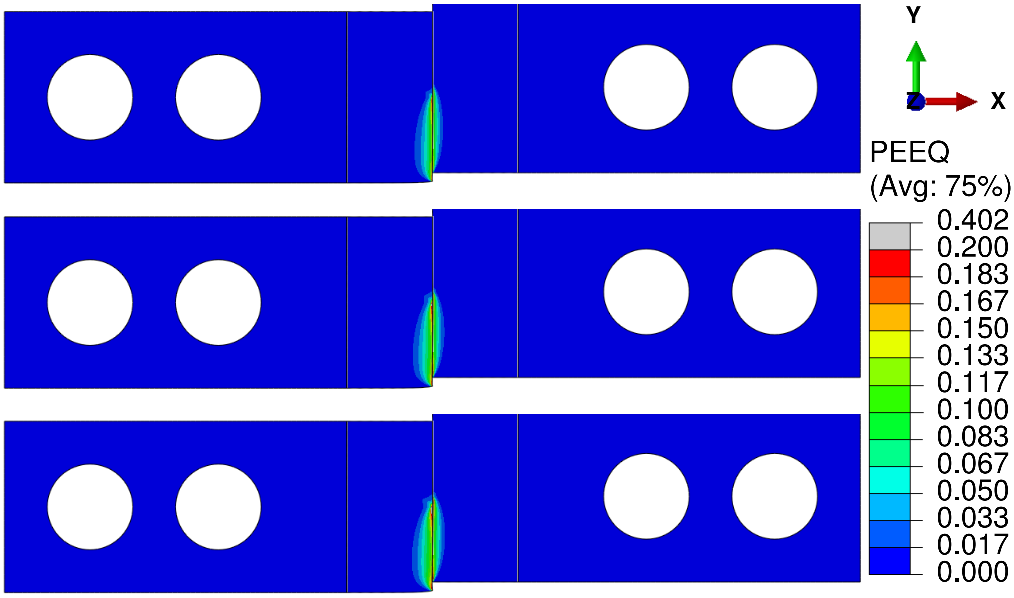

Figure 4.37: Equivalent plastic strain after failure. l's are equal to: 0.25 (top), 0.5 (middle), 1 (bottom).

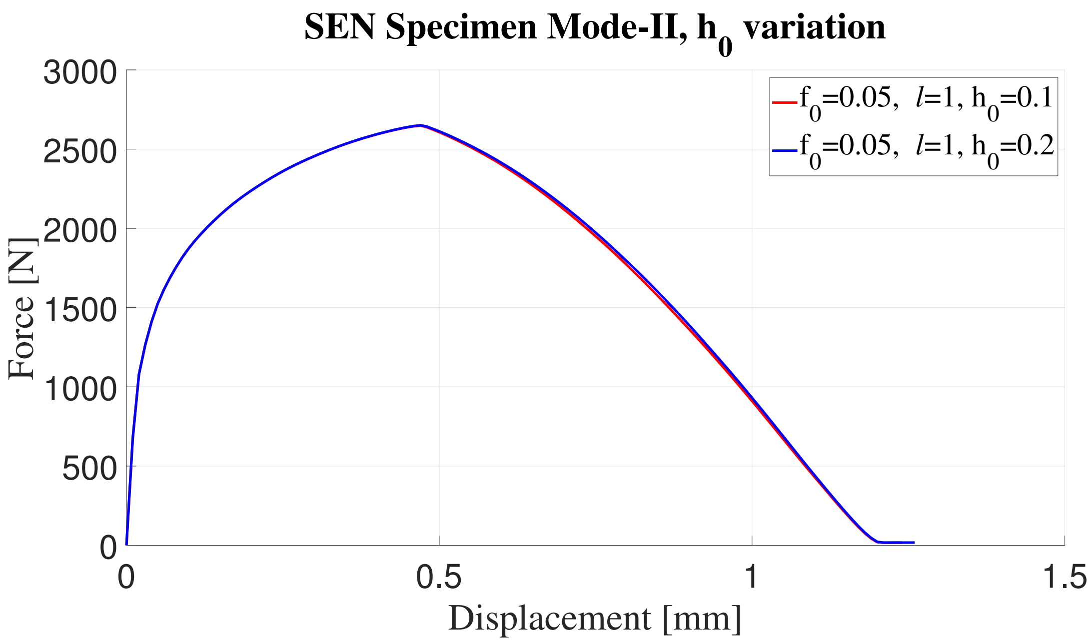

Figure 4.38: Force displacement response under mode-II loading for changing initial pore fraction, h_0.

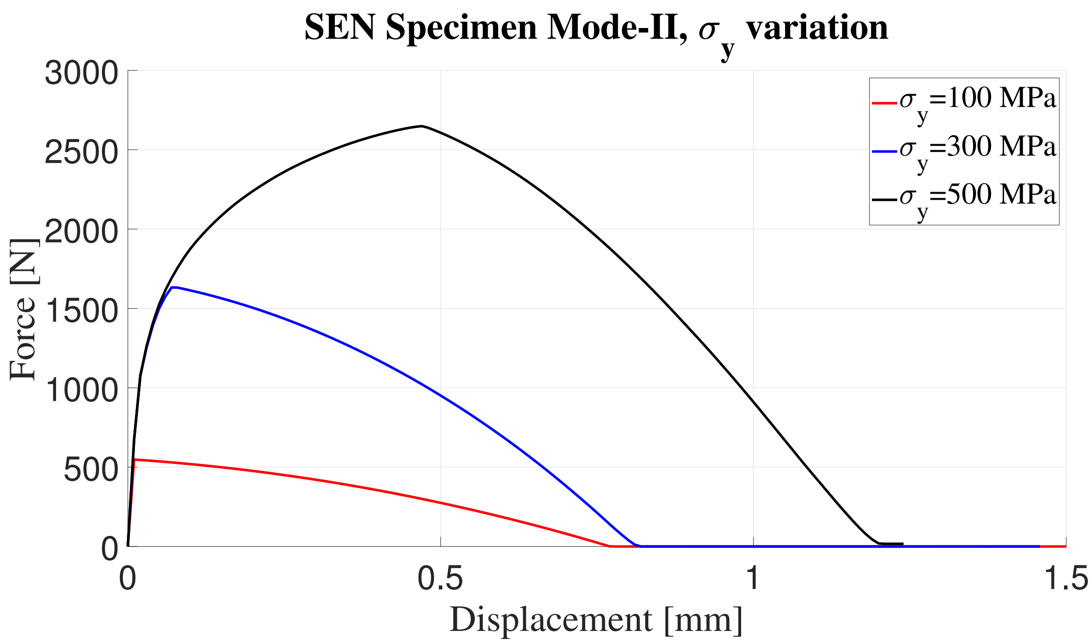

Figure 4.39: Force displacement response under mode-II loading for changing yield stress, σ_y.

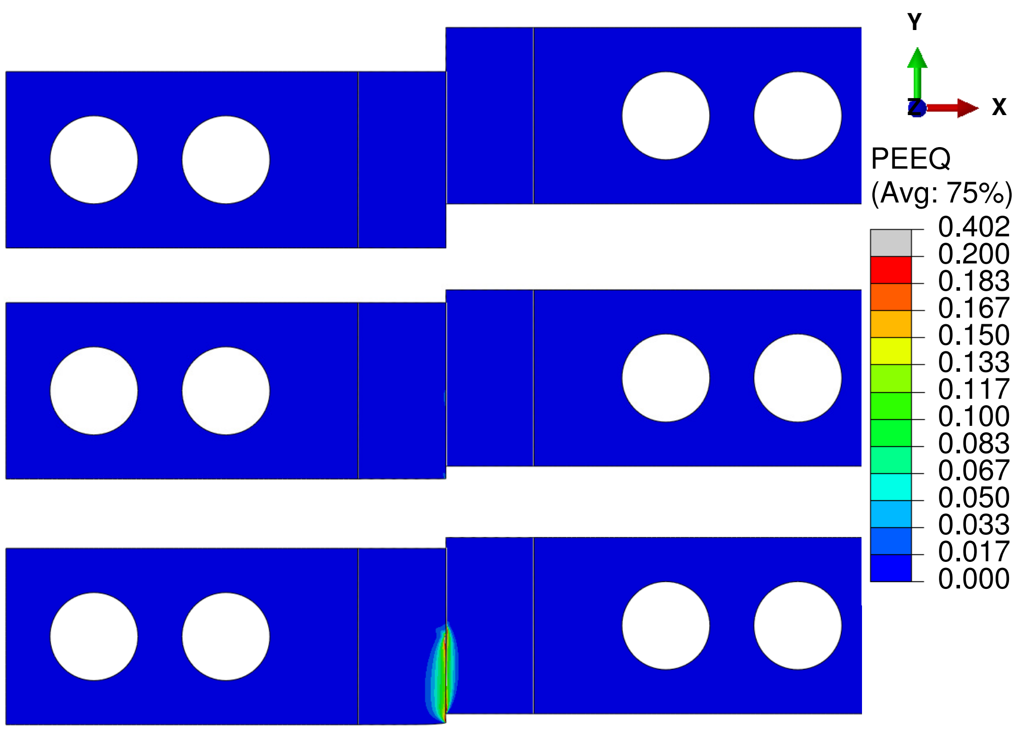

Figure 4.40: Equivalent plastic strain after failure. σ_y's are equal to: 100 MPa (top), 300 MPa (middle), 500 MPa (bottom).

4.3.3 Mixed-Mode Loading

SEN specimen is loaded with mixed-mode by using holes 2 through 5. Please refer to Fig. 4.15 to check the meaning of hole numbers. As a reminder, the mechanism with holes surrounding the SEN specimen allows us to simulate mode-I, mode-II, or mixed-mode loading by changing loading direction. Let U_x be the displacement boundary condition which is normal to crack path, U_y is the displacement boundary condition tangential to crack path, and $\alpha = \tan^{-1}(U_y/U_x)$ is the ratio of these displacements, also named as proportionality ratio in Chapter 3, see below. Table 4.1 gives the boundary condition applied at each hole. They are equal to, $U_x = 5\sin\alpha$ and $U_y = 5\cos\alpha$, where $U = \sqrt{U_x^2 + U_y^2} = 5$.

Similar to previous sections, the effect of f_0, h_0 and l is investigated by changing

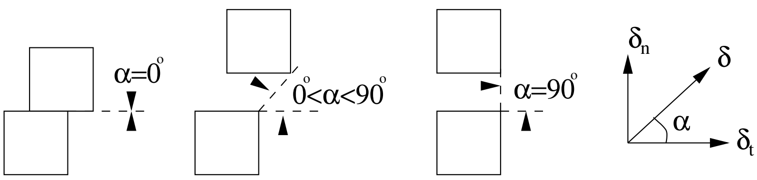

Figure 4.41: Proportional loading of cohesive element where α is proportionality ratio.

	Hole 1 Mode-I	Hole 2	Hole 3	Hole 4	Hole 5	Hole 6 Mode-II
$\alpha[^o]$	90	72	54	36	18	0
$U_x[mm]$	5.0	4.7553	4.0451	2.9389	1.5451	0.0
$U_y[mm]$	0.0	1.5451	2.9389	4.0451	4.7553	5.0

Table 4.1: Displacement boundary conditions at each hole and the angle of loading direction.

one parameter while keeping others constant. This is repeated for holes 2, 3, 4 and 5, and the effect of mode-mixity is observed in this way.

In Fig. 4.42, f_0 is taken as 0.05 and 0.2 for holes 2 to 5. Dotted lines, $f_0 = 0.2$,

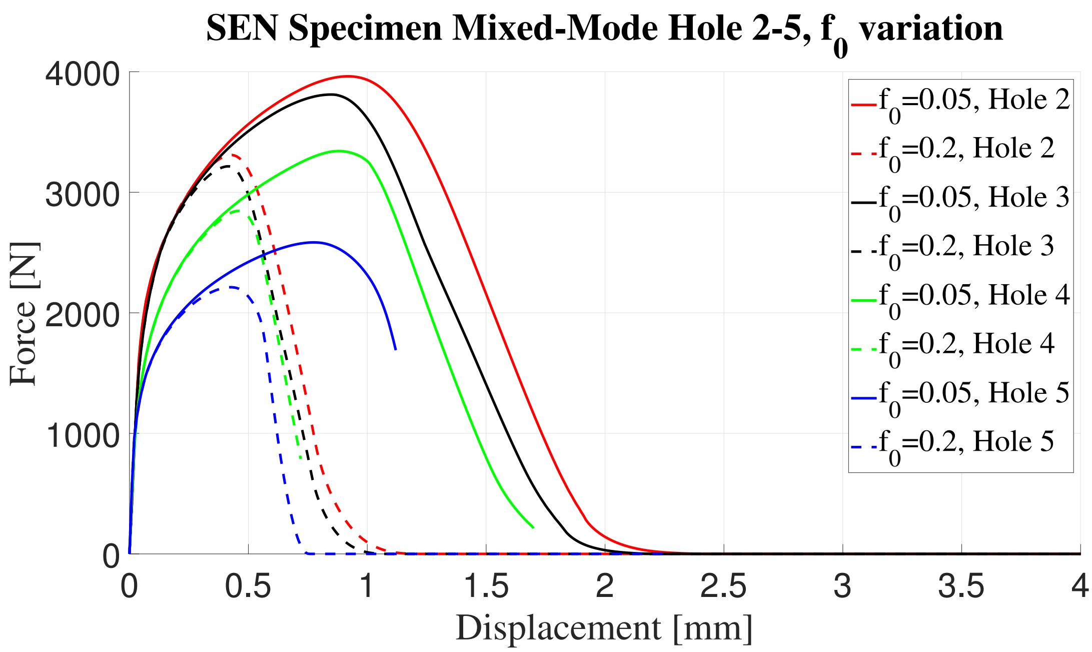

Figure 4.42: Force displacement response under mixed-mode loading for changing initial pore fraction, f_0.

represent low energy, whereas filled lines, $f_0 = 0.05$, represent high energy. As always, smaller f_0 means higher strength and toughness, but these qualities decrease from hole 2 to hole 5 loading cases, i.e., when mode-II becomes more dominant than mode-I. This is expected because with the current material parameters, f_0, h_0, l, σ_y, pure mode-II fracture energy is smaller than pure mode-I fracture energy. This dependency will be discussed later on.

To understand the effect of f_0 with changing mode-mixity in a qualitative manner, the area under the force-displacements curves is calculated. Note that some of the analyses are not fully converged, so full softening could not be observed in some cases. Hence, the area calculated is actually the area until the maximum force is reached. Since softening curves are of similar shape and proportion, this should not pose a problem. The calculated areas represent the trend in fracture energy. The energies are compared between two different f_0 values for each hole, and the percentage increase from the smaller area to the bigger area is shown in Table 4.2. It can be seen that the effect of f_0 fades when mode-II becomes dominant. As it was discussed in pure mode-II section, the reason is the fact that maximum mode-II traction obtainable with decreasing f_0 has a limit, so this is the expected response in mixed-mode.

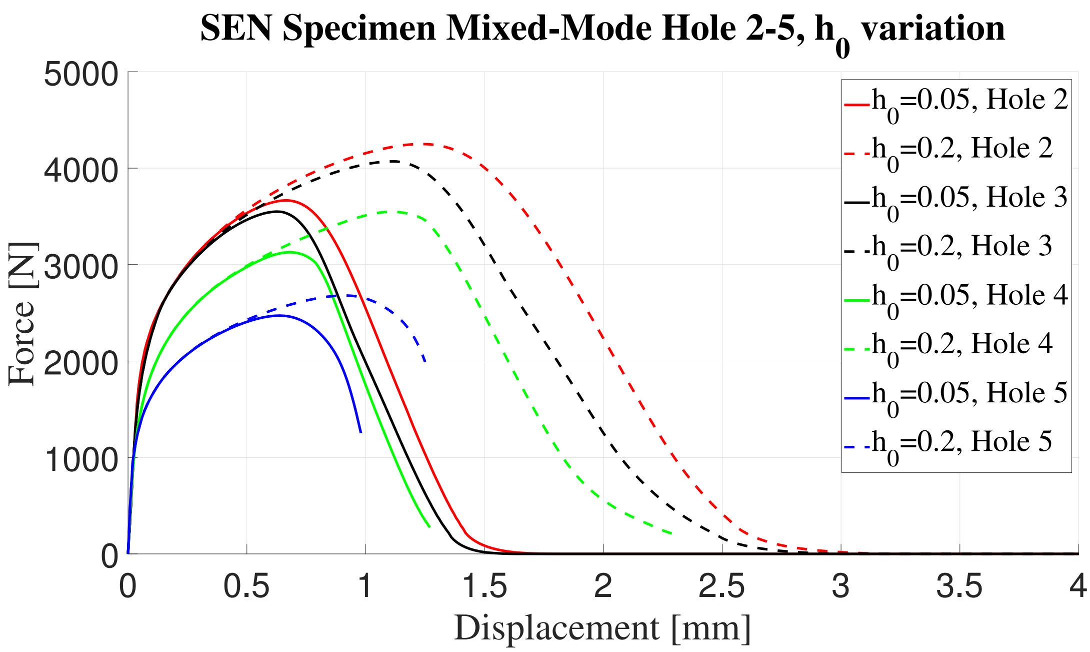

Figure 4.43: Force displacement response under mixed-mode loading for changing initial pore height, h_0.

In Fig. 4.43, same study is repeated for initial pore height, h_0. Increasing the pore height increases strength and toughness. This effect is expected to diminish towards mode-II loading, and indeed this is the case seen in Table 4.2.

Fig. 4.44 shows the change with changing pore spacing, l. Strength and toughness behavior is as expected, but this time the effect is expected to grow when mode-II is dominant since l is mode-II related. This seems to be true in force-displacement curves, and Table 4.2 confirms it.

% energy increase between low-high energy cases	Hole 2	Hole 3	Hole 4	Hole 5
% increase with changing f_0	158.72	142.49	127.10	106.76
% increase with changing h_0	117.25	102.68	85.13	53.97
% increase with changing l	26.95	45.30	59.00	88.82

Table 4.2: Changes in fracture energy with loadings at different holes for changing parameters.

These results indicate that mixed-mode implementation is working as intended. The

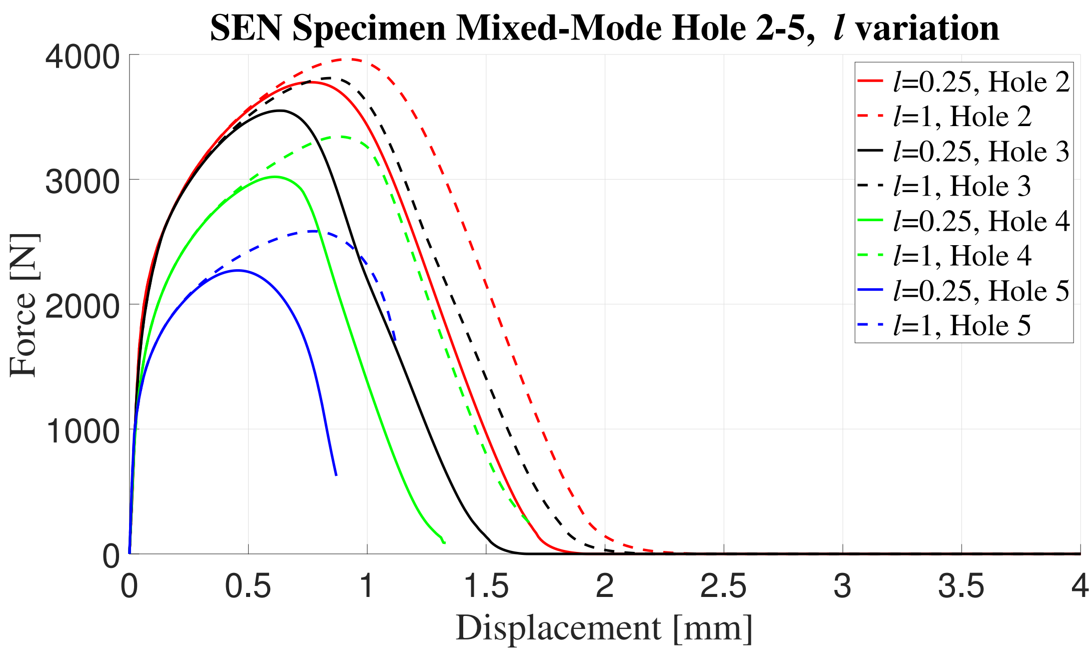

Figure 4.44: Force displacement response under mixed-mode loading for changing pore spacing, l.

response obtained with changing material parameters for different mode-mixity ratios correlates with the derived model. It was stated that in the previous examples that mode-I fracture energy is higher than mode-II fracture energy. Next, it is investigated if the opposite is possible.

In Chapter 3 mixed-mode section, it was shown that work of fracture for pure mode-I could be altered with h_0, for pure mode-II with l, and f_0 affects both mode-I and mode-II (Figs. 3.15, 3.16). Let us select two sets of parameters, one favoring mode-I other favoring mode-II. Using these parameters, traction-separation curves and work of fracture versus proportionality ratio graph will be presented, which is for a single material point. Then they will be compared with macroscopic SEN specimen example. Selected parameter sets are given in Table 4.3, and corresponding traction-separation curves without elastic region is given in Fig. 4.45.

Is the mode-II dominant case in Fig. 4.45 really mode-II dominant? Yes, the dominant part is the area under the curves, i.e., work of fracture. However, maximum tangential traction T_t is smaller than normal traction T_n. Unfortunately, this is a shortcoming of the derived model. Maximum tractions cannot be controlled separately; they are both dependant on σ_y and f_0. Furthermore, in most of the cases, maxi-

	$\sigma_y[MPa]$	h_0	f_0	l
Mode-I dominant	500	0.2	0.2	0.25
Mode-II dominant	500	0.05	0.2	4

Table 4.3: Parameters to obtain mode-I or II dominant fracture energies.

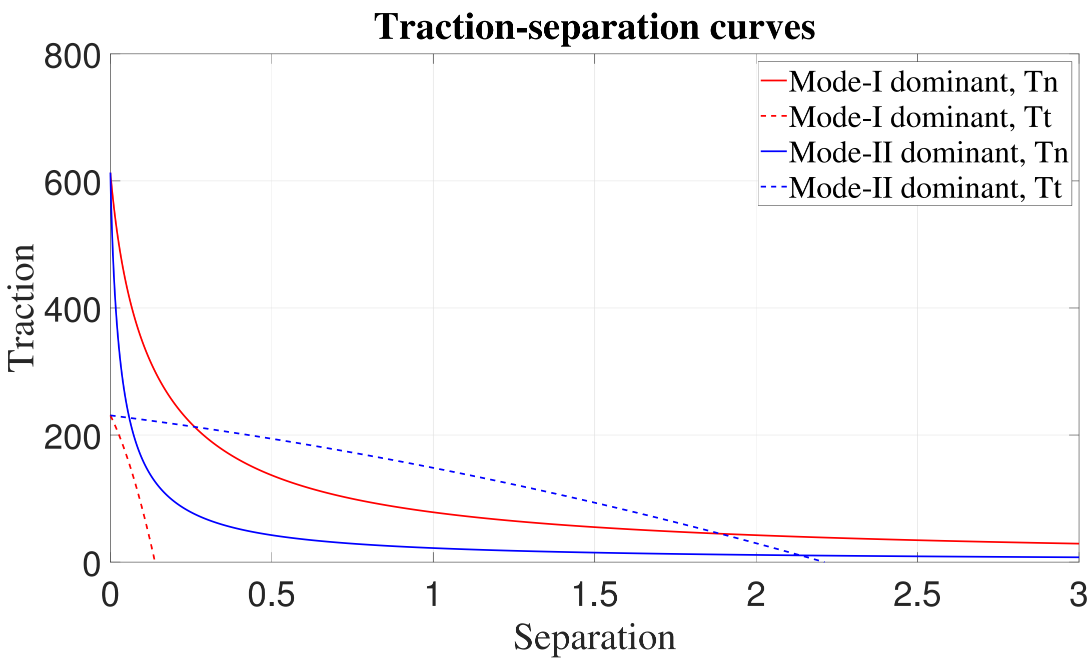

Figure 4.45: Traction separation curves for parameters in Table 4.3.

mum mode-I traction is higher than mode-II traction. Again, remember the maximum traction equations,

$$T_{n,max} = \sigma_y \left[(1-f_0)^2 + \left(\frac{1}{\sqrt{3}} ln \frac{1}{f_0} \right)^2 \right]^{\frac{1}{2}} \quad \text{and} \quad T_{t,max} = \frac{\sigma_y}{\sqrt{3}} [1-f_0]$$

Let us check how these maximum tractions change with σ_y and f_0. Looking at Figs. 4.46 and 4.47, when f_0 is constant and σ_y is changed, T_n is always bigger than T_t. And, when σ_y is constant and f_0 is changed, T_n is bigger most of the time until $f_0 \approx 0.6$. After that T_t is bigger, but tractions are very small already. Moreover, selecting an initial pore fraction bigger than 0.6 does not make much sense physically. So, instead of maximum tractions, the focus was on work of fracture to make a mode dominant.

Using the parameter set in Table 4.3, calculations are conducted for a single material

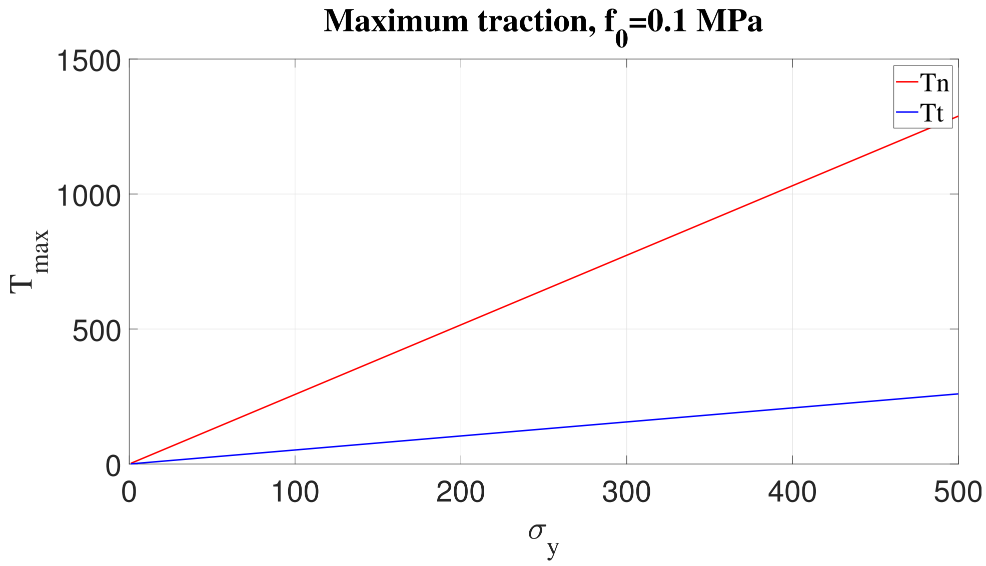

Figure 4.46: Maximum traction depending on σ_y.

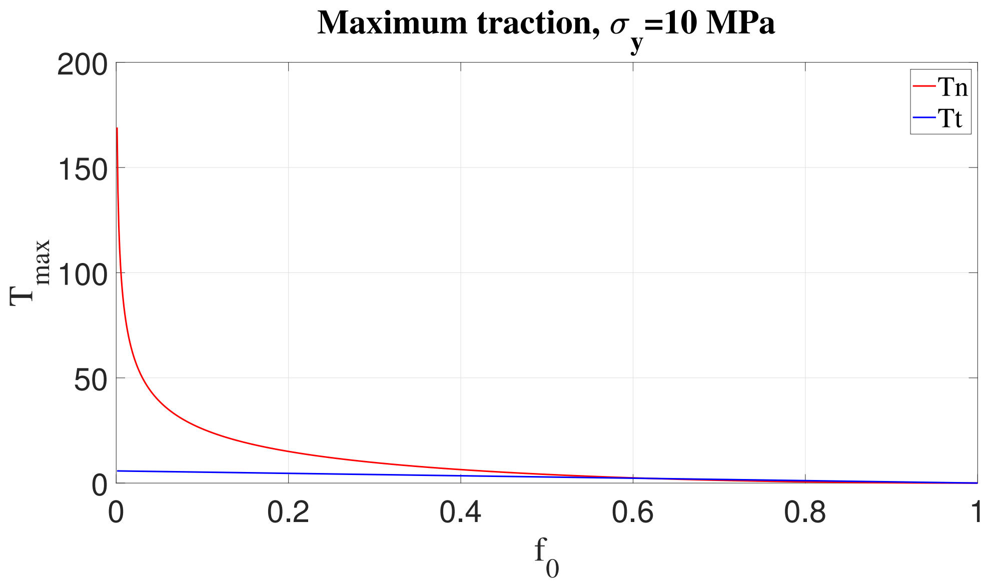

Figure 4.47: Maximum traction depending on f_0.

point in MATLAB. The work of fracture graphs for proportional loading is shown in Fig. 4.48. Next, these parameters are used in the SEN specimen model using holes 2 to 5.

When the mode-I dominant parameter set is used, Fig. 4.49 is obtained. As in Fig. 4.48, mode-I dominant case, total energy seems to decrease from mode-I to mode-II loading. The areas under curves are calculated again for the SEN specimen to compare with a single material point case. Naturally, the SEN specimen's energy

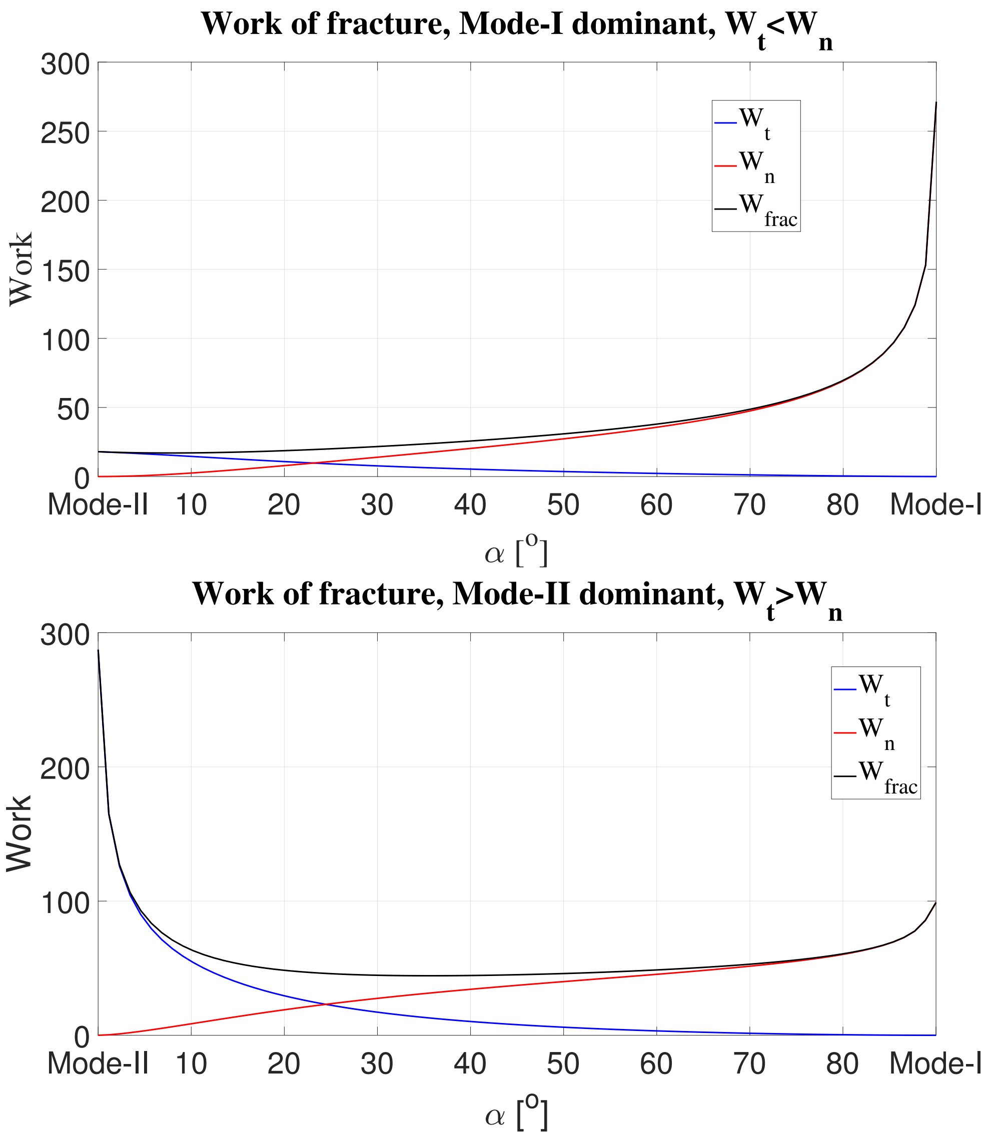

Figure 4.48: Work of fracture depending on loading angle α, for mode-I dominant set (top) and mode-II dominant set (bottom).

magnitudes are a lot higher, so the energies are normalized with maximum energy in the corresponding graph. The results are shown in Fig. 4.50. The behavior is quite similar; there is a gradual decrease from mode-I fracture energy to mode-II fracture energy.

If the mode-II dominant parameter set is used, Fig. 4.51 is obtained. Holes 1, 2 and 3 show similar responses, only the pure mode-I case, hole 1, is asymptotic. When mode-II displacement starts to become dominant, holes 4, 5 and 6, behavior starts to change. Strength and energy decrease until pure mode-II, hole 6, case. Some of the

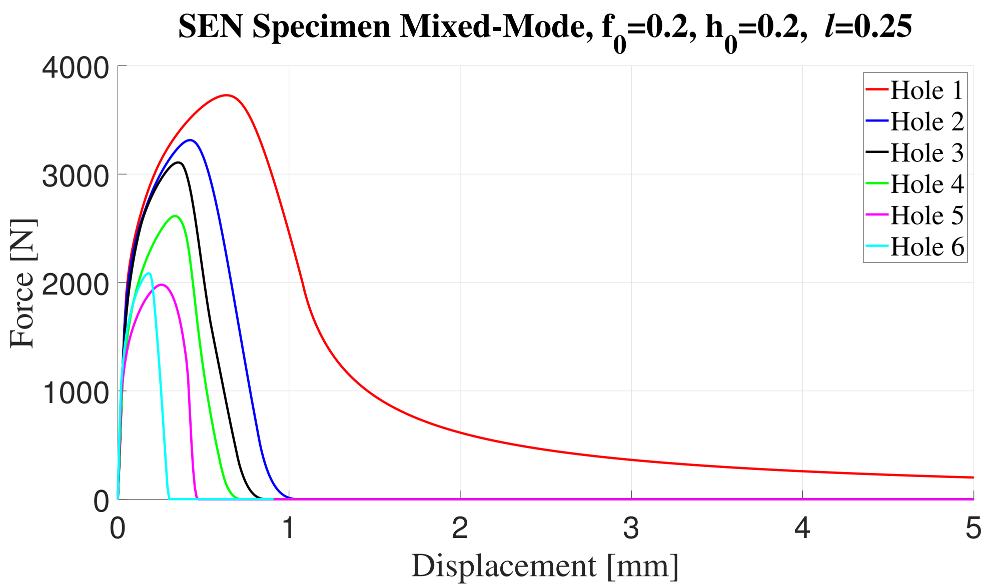

Figure 4.49: Force displacement response for loading through different holes.

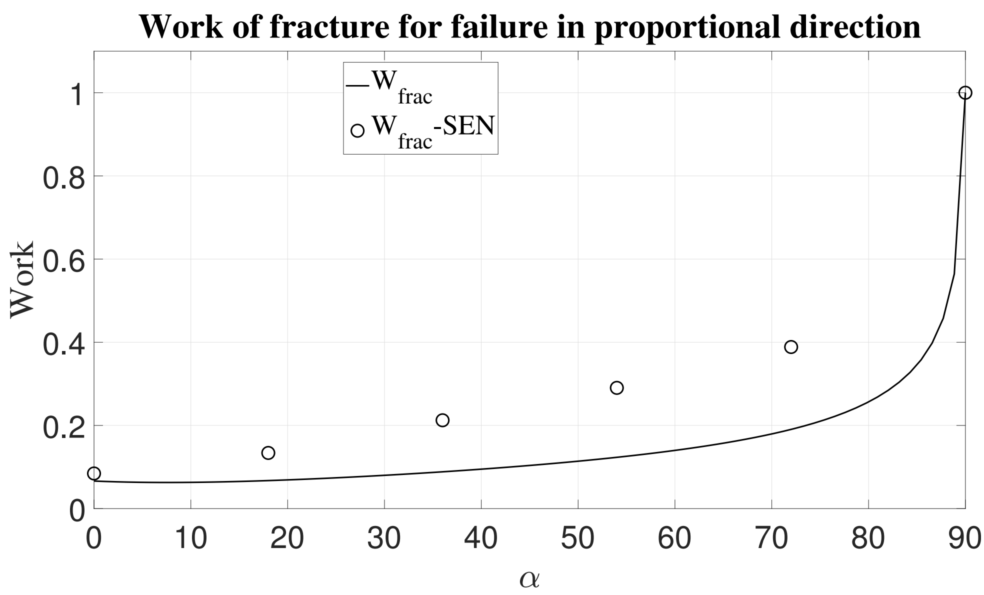

Figure 4.50: Comparison of fracture energy for SEN specimen and single material point tests.

analyses did not complete; still areas under the curves can be calculated with certain assumptions. Softening behavior is quite linear for mode-II dominated cases. Therefore the last data point in the curves can be used to predict the remaining portions with reasonable accuracy. When the fracture energies are calculated this way and normalized with the maximum energy, Fig. 4.52 is obtained. Mode-II fracture energy

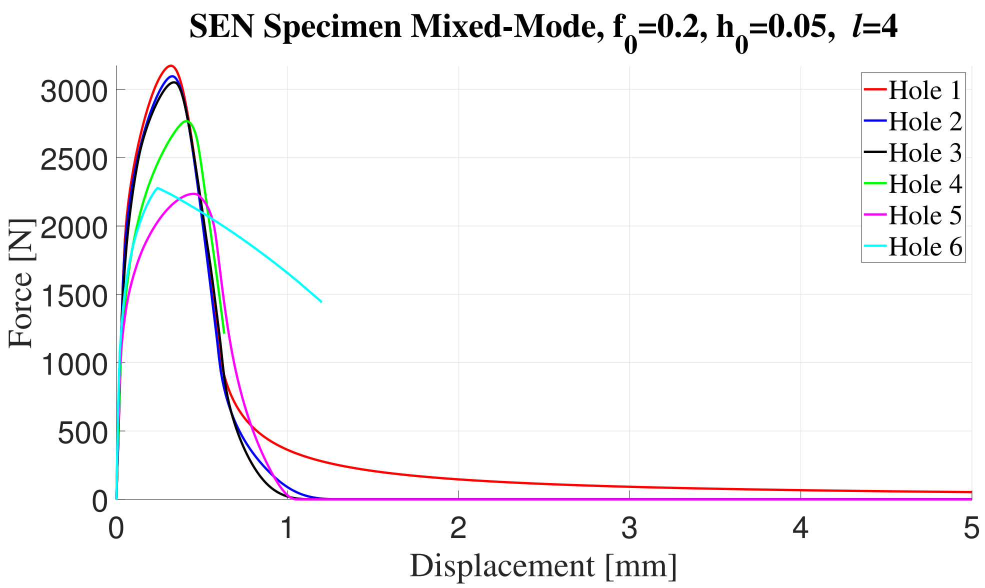

Figure 4.51: Force displacement response for loading through different holes.

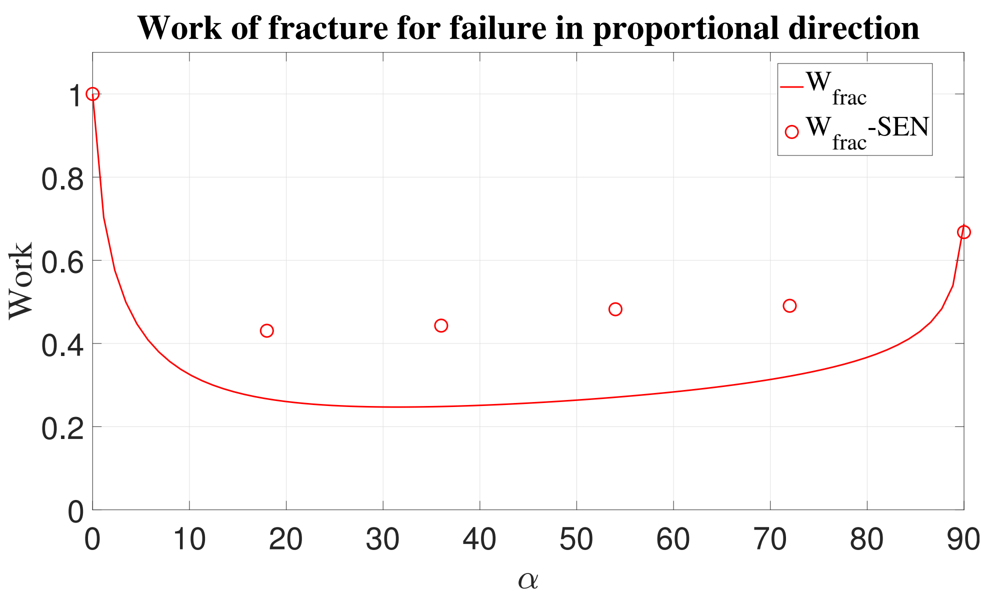

Figure 4.52: Comparison of fracture energy for SEN specimen and single material point tests.

is higher than mode-I fracture energy as expected, and the trend of SEN specimen examples is similar to single material point tests.

Previous examples are intended to show that the mixed-mode implementation is working by showing the correlations with the derived model. The behavior of the model shows logical connections to the physical phenomenon in the context of ductile fracture. However, the implementation has some downsides due to the nature of CZ elements employed in ductile fracture analysis. For example, it cannot predict the crack path at the moment. This is a problem of the cohesive zone models, intrinsic cohesive zone models in particular. Since the cohesive elements are pre-inserted, crack path should be known beforehand. Extrinsic cohesive zone models bypass this by inserting elements during analysis to wherever necessary, but still crack path is limited by mesh. This capability is very relevant in ductile fracture since the crack path is likely to change depending on loading or deficiencies. Indeed, in our mixed-mode loading SEN specimen example, the crack may follow a diagonal path, instead of a vertical one, when holes 2 to 5 are used. Sutton et al. showed crack growth path of 2024-T3 aluminum for various loading angles using Arcan test specimen [109]. Experiments showed that the crack followed an almost straight path for mode-I/II loading, while it followed an angled path for mixed-mode loading where the path angle depends on loading angle.

To show if this is the case, a simple strategy is followed with our pre-inserted intrinsic cohesive elements. In addition to the vertical path, cohesive elements are placed on a diagonal angled path, see Fig. 4.53. The first five cohesive elements at the crack tip for both paths are deleted because there is only one bulk element at the intersection of paths, and this reduces accuracy. Note that this was tried with as many as 19 paths initially with no logical results. Predicting the crack path with pre-inserted cohesive elements was found to be very challenging. The main drawback was the fact that cracks can initiate anywhere when there are cohesive elements everywhere. Therefore, such a simplified setting is preferred to illustrate the mix-mode failure analysis.

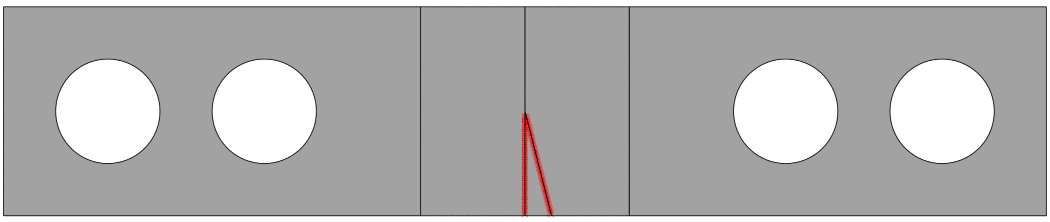

Figure 4.53: 2 potential crack paths, one vertical and one diagonal.

With the two potential crack paths, depending on the loading direction imposed through certain holes, the diagonal crack path is expected to be followed, i.e., holes 2 to 5. In pure mode-I and mode-II loadings, the crack should still propagate at the vertical path. So, this idea is tested by loading the SEN specimen at each hole. Fig. 4.54 shows the comparison of force-displacement responses with the original single vertical path model. The figure is quite crowded, but notice that the curves' shapes are very similar for holes 1, 6, and 5, where hole 1 is pure mode-I and hole 6 is pure mode-II loading. Forces are reduced in 2 path examples, possibly due to less number of cohesive elements. On the other hand, for holes 2, 3 and 4, the shape of 2 path curves is different compared to single path. As it can be guessed, in these mixed-mode loading cases, crack propagated in the diagonal direction. Hole 5 loading is very close to a mode-II loading, and the crack followed the vertical path in that case. Von Mises stress distribution is shown in Fig. 4.55 at the maximum force point. There

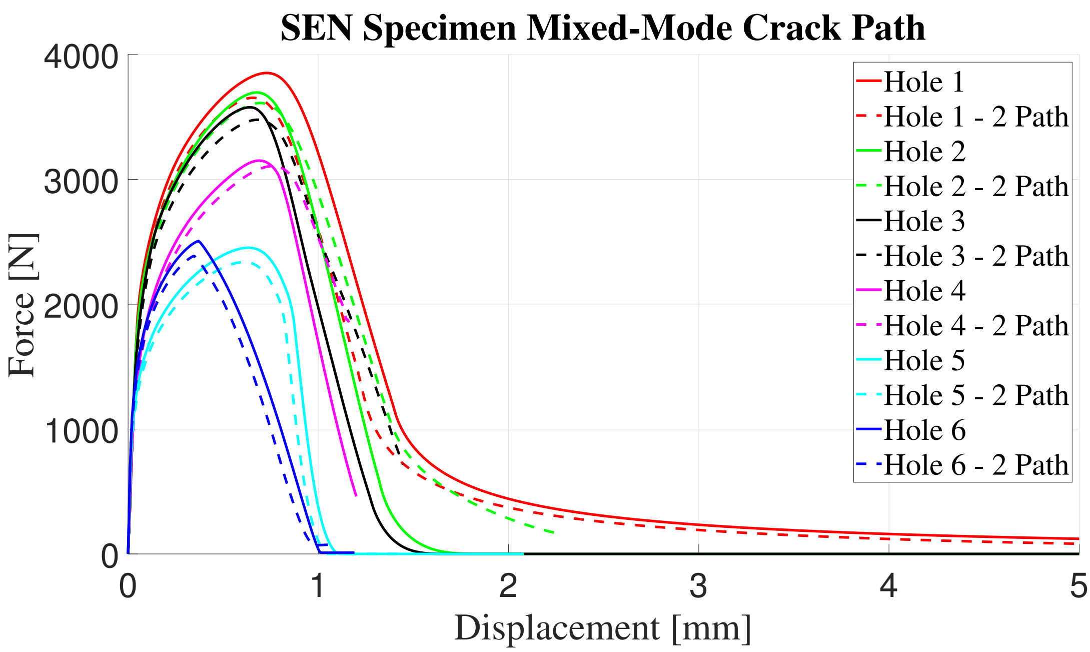

Figure 4.54: Force displacement response for loading through different holes. Straight lines represent 1 crack path model, and dotted lines are for 2 crack paths model.

is a clear change in stress concentration direction depending on the loading direction. When the concentration is symmetric (hole 1) or has a vertical shape (holes 5 and 6), crack follows the vertical path. When stress concentration has an angled shape (holes 2, 3 and 4), crack follows the diagonal path. In Fig. 4.56, stress contours at 1mm total displacement is shown. In this figure, crack paths can be seen clearly.

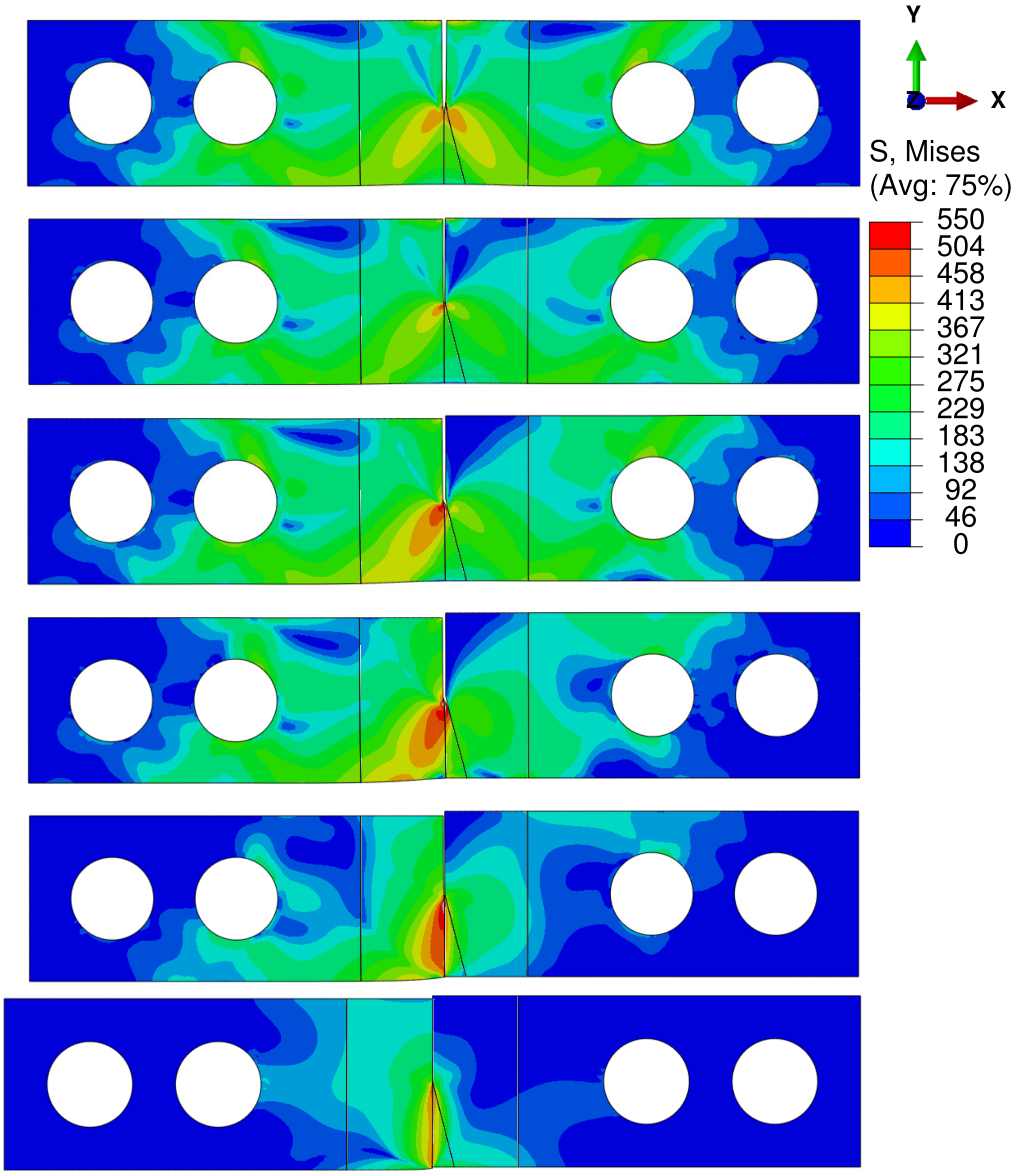

Figure 4.55: Von Mises stress just before softening for different loading holes in SEN specimen. From top to bottom holes 1 to 6 are used.

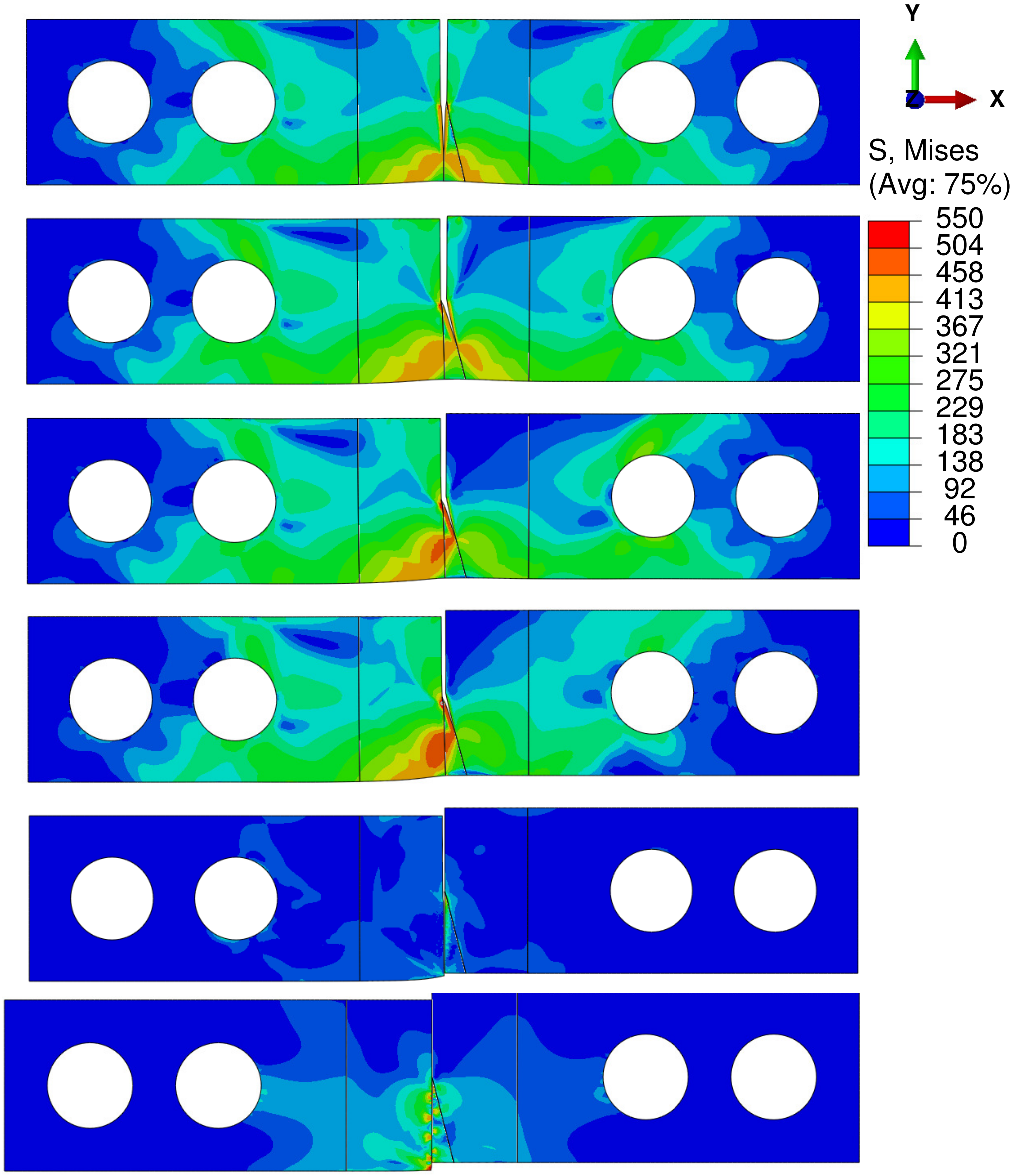

Figure 4.56: Von Mises stress at total displacement 1mm for different loading holes in SEN specimen. From top to bottom holes 1 to 6 are used.

All in all, the current the chapter illustrates that the developed micromechanical model performs well in the case of mode I, mode II and mixed-mode ductile fracture simulations using implemented UEL subroutines. The influence of microstructural parameters such as initial porosity, cavity height, cavity spacing on the ductile failure is discussed in such a context first time in the open literature. As mentioned previously, it is not a straightforward task to employ cohesive zone elements in mixed-mode crack propagation studies. However in the simplified setting, the examples clearly show the expected crack propagation phenomenon. In the next chapter, the performance of the model is tested for intergranular cracking in a polycrystalline plasticity context.

CHAPTER 5

MICROMECHANICAL APPLICATIONS

In the previous chapter, behavior and implementation of the derived micromechanics based cohesive zone model was tested with commonly used ductile fracture specimens in the literature. However, the length scale of these specimens are on the order of millimeters. In this chapter, staying at the true to length scale of the derivation, an application of MBCZM in a micro-sized polycrystal specimen is presented. The initial modeling idea of this behavior is discussed in Yalçinka et al. [110] and the results presented here are taken from an article that has been submitted recently for publication [101].

In metallic materials, as the size gets smaller, deformation homogeneity is lost. A heterogeneous plastic strain evolution is obtained due to increased effect of grains and grain boundaries. Thus, classical J2 plasticity theory cannot be used in this length scale. Instead, crystal plasticity theories are employed which take into account the influence of anisotropic plasticity evolution in the grains. In such a modeling approach, the plastic strains are obtained through a tensorial summation of the plastic slips at each slip system, which evolve differently due to the orientation of the crystal. Therefore, the grains deform differently and due to the orientation mismatch a stress concentration occurs at the grain boundaries, which might be a serious problem for metallic materials depending on the microstructure around the grain boundaries. While in local crystal plasticity modeling approaches a sharp change develops at the grain boundaries, the nonlocal crystal plasticity modeling handles the localization and stress concentration in a more physical way. Moreover due to the incorporated length scale parameter these models can predict the size dependent plasticity behavior as well. In this context a strain gradient (non-local) crystal plasticity (SGCP) model (see e.g. Yalcinkaya et al. [111] [98]) is combined with the developed MBCZM for the prediction of intergranular cracking occurring due to the stress arise at the grain boundaries. SGCP is used for bulk plasticity behavior in the grains while MBCZM is employed at the grain boundaries.

5.1 Intergranular Ductile Fracture in High Strength Aerospace Alloys

High strength aerospace aluminum alloys, e.g. 7xxxx series., suffer from loss of fracture toughness due to the heat treatment leading to intergranular ductile fracture. An important failure mechanism in these materials is encountered when the grain boundaries are weakened by a specific state of precipitation around them but they remain strong enough that the failure in the vicinity of the grain boundaries is ductile. This mechanism is known as intergranular ductile fracture that is very well known in aerospace aluminum alloys.

While after a fast quench there is no precipitation observed in these materials, they appear during a subsequent aging treatment around the grain boundaries, which are rather small in over-aged condition. After a slower quench the precipitates are present largely at the grain boundaries which get bigger with slower quench rates (see the observations in e.g. Dumont et al. [112]). These precipitates are accompanied with the precipitate free zones (PFZ) around the grain boundaries (see e.g. Unwin et al. [113]; Pardoen et al. [114]). The PFZ is naturally rather soft and deforms first plastically. In this situation the elastic or harder grains impose a strong constraint on the PFZ involving large stress triaxiality. It is very well known now that the higher triaxiality values give larger void growth rate leading to rapid coalescence of voids and the initiation of related intergranular cracking. Another possibility is that the stress in the grains can reach the yield stress before the onset of coalescence in the PFZ; the stress triaxiality then drops in the PFZ then the transgranular fracture mechanism might occur as well. The competition between these two failure mechanisms were studied in the literature a very simplified definition of microstructure with various parameters that gave certain conclusions about the loading and the microstructure on the initiation of the cracks. However a realistic model with physics based plasticity and fracture mechanics models considering the effect of different microstructural parameters of the intergranular failure behavior of these materials have never been addressed before and it is the main objective of this chapter. Qualitative conclusions are obtained from the numerical analysis of micron sized specimens, and some of them are presented here.

5.1.1 The Numerical Model of the Polycrystalline Specimen

Simulations are run in Abaqus software for a cylinderical specimen with 25µm length and 25µm diameter presented in Fig. 5.1. It consists of 100 grains randomly distributed using Voronoi tesselation, and each grain is randomly oriented. For bulk of grains strain gradient crystal plasticity model is used while cohesive zone elements are inserted at intergranular faces. In Fig. 5.1, the specimen and the boundary conditions are shown, where γ represent the crystallographic slip value that can be specified in SGCP framework, and u is the displacement. At the fixed surface displacements $u_{1,2,3}$ are zero, while at the free surface $u_{1,2}$ are zero and u_3 has a finite value. Slip value γ is zero at both surfaces. No boundary condition is given at the lateral surface.

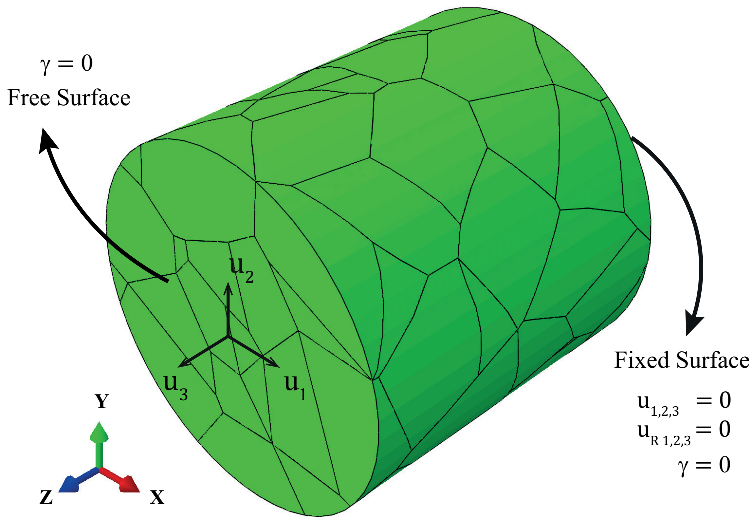

Figure 5.1: The representation of the boundary value problem with 100 grains.

The previously developed cohesive zone elements are implemented currently in a 2D setting. In the current example, 3D dimensional potential based cohesive zone elements (see e.g. Park et al. [82], Cerrone et al. [115]) are employed in a mixed-mode environment whose TSL are obtained from the micromechanical analysis presented in Chapter 3. To realize this, traction-seperation relations obtained in Chapter 3, equations (3.13-3.14), are fitted with Park-Paulino-Roesler (PPR) CZM, which are characterized by the following variables. ϕ_n, ϕ_t, normal and tangential fracture energies, σ_{max}, τ_{max} normal and tangential cohesive strengths, α, β, shape parameters, λ_n, λ_t normal and tangential initial slope indicators. Corresponding parameters in PPR are obtained for given f_0, h_0, and l parameters in MBCZM. In the fits, it is made sure that the two important parameters of a TSL are as close as possible. Namely, maximum traction and fracture energy, i.e. the area under the curves as shown in Fig. 5.2. The found parameters are given in Table 5.1. In this way, the effect of micromechanical parameters is investigated with a polycrystal specimen.

Table 5.1: Corresponding parameters in PPR model for given h_0, f_0 and $l = 1\mu m$.

f_0 for a constant $h_0 = 0.1\mu m$	Φ_n [N/m]	Φ_t [N/m]	σ_{max} [MPa]	τ_{max} [MPa]	α	β	λ_t	λ_n
$f_0 = 0.01$	100.0	52.9	453.9	91.5	37.0	1.7	0.005	0.102
$f_0 = 0.05$	80.0	41.8	315.7	87.8	26.9	1.9	0.005	0.092
$f_0 = 0.1$	73.3	34.3	256.9	83.1	23.1	1.8	0.005	0.059

5.1.2 The effect of initial porosity f_0 at the grain boundaries

In this section the numerical response of the MBCZM is illustrated very shortly through a couple of examples. Please refer to the submitted article for the detailed description of the numerical example and the formulation of the bulk crystal plasticity model [101]. The purpose here is to give an example on the employment of the developed micromechanics based cohesive zone model in predicting the fracture initiation and propagation at grain scale in micron sized specimens, hence the section is kept quite short.

The initial example addresses the influence of porosity at the grain boundaries on both macroscopic constitutive response and spatial stress and strain evolution. In order to illustrate porosity effect on the fracture at the grain boundaries three different initial porosity ratios are considered, i.e. $f_0 = 0.01, f_0 = 0.05, f_0 = 0.1$ for a constant pore

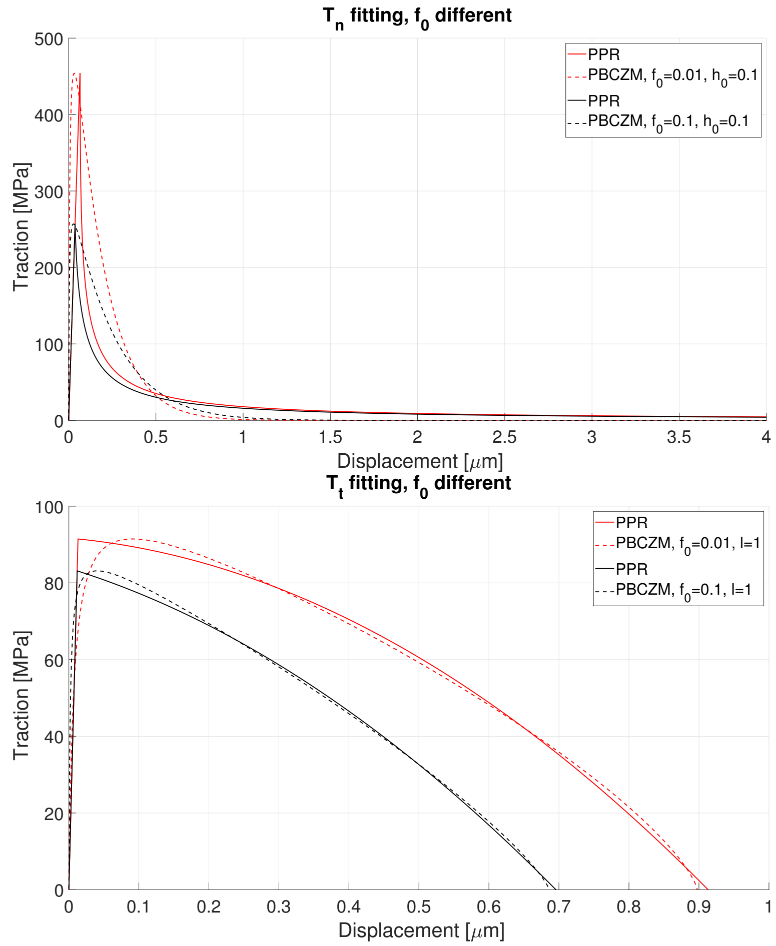

Figure 5.2: Comparison of PPR and MBCZM traction-separation laws after fitting for mode-I (top) and mode-II (bottom).

height $h_0 = 0.1$. The stress-strain response of the specimen deformed under uniaxial tension is presented in Fig. 5.3. At the hardening stage three specimens behave identical behavior, however, as expected, the ones with higher porosity start softening earlier due to their lower cohesive strengths. There is considerable reduction in the toughness of the material with increasing grain boundary cavity ratio. Then contour plots of stress and strain are illustrated at peak engineering stress, and at 5% global strain state in Fig. 5.4 and 5.5 respectively. Fig. 5.4 shows that at peak stress state, the case with lowest porosity reaches to highest stress at the grain boundaries and highest strain in the grains. When the cracked specimens are analyzed in Fig. 5.5, the crack initiation locations for high porosity grain boundary microstructure ($f_0 = 0.05$ and $f_0 = 0.1$) are identical. However, surprisingly, it is different for the lowest porosity case, which means even though the initial cavity is distributed homogeneously at all grain boundaries the crack initiation location might depend on the level of the porosity. Therefore the interaction between the orientation mismatch and the cavity ratio influence both toughness and the crack path in the specimen. Moreover it is important to note that, at the same deformation state with 5% global strain while the specimens with $f_0 = 0.05$ and $f_0 = 0.1$ are almost stress free as shown in Fig. 5.5(a,b,c) the one with $f_0 = 0.01$ has not failed and still caries load, which would show the effect of initial pore fraction on ductility.

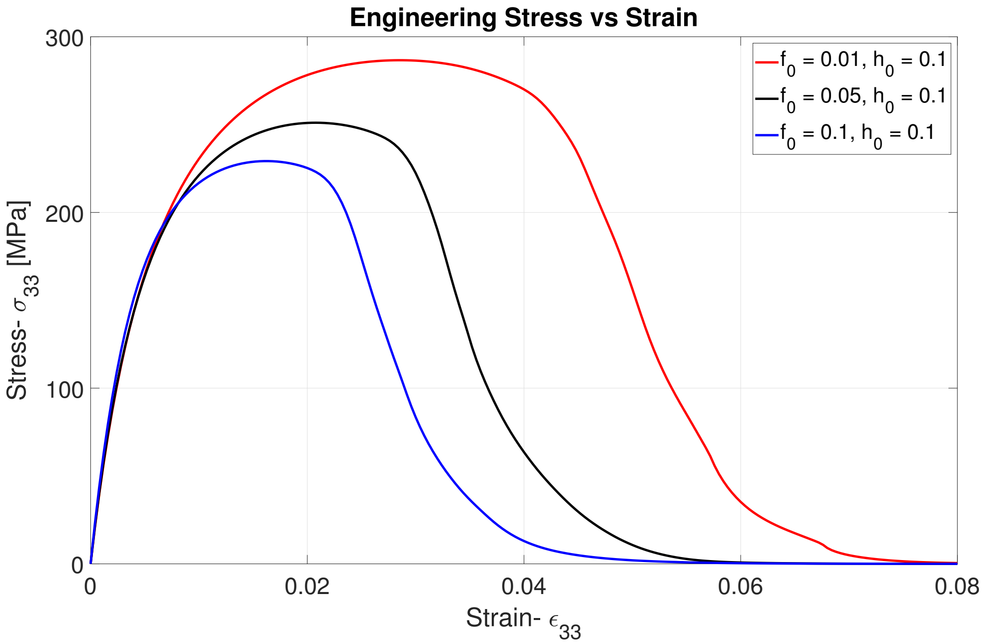

Figure 5.3: Engineering stress vs. strain response of a polycrystalline cylindrical specimen with 25µm diameter and 25µm length including 100 grains deformed under tensile loading for variable initial pore fraction, f_0 and constant initial pore height, h_0.

5.1.3 Grain orientation distribution

The next example studies the influence of grain orientations on both the macroscopic and microscopic behavior of micron sized samples under uniaxial loading. Five different random orientation sets are assigned to the grains of the sample with 100 grains, and the engineering stress-strain responses are plotted in Fig. 5.6 (top). There is no substantial difference in the hardening region due to the high number of grains in

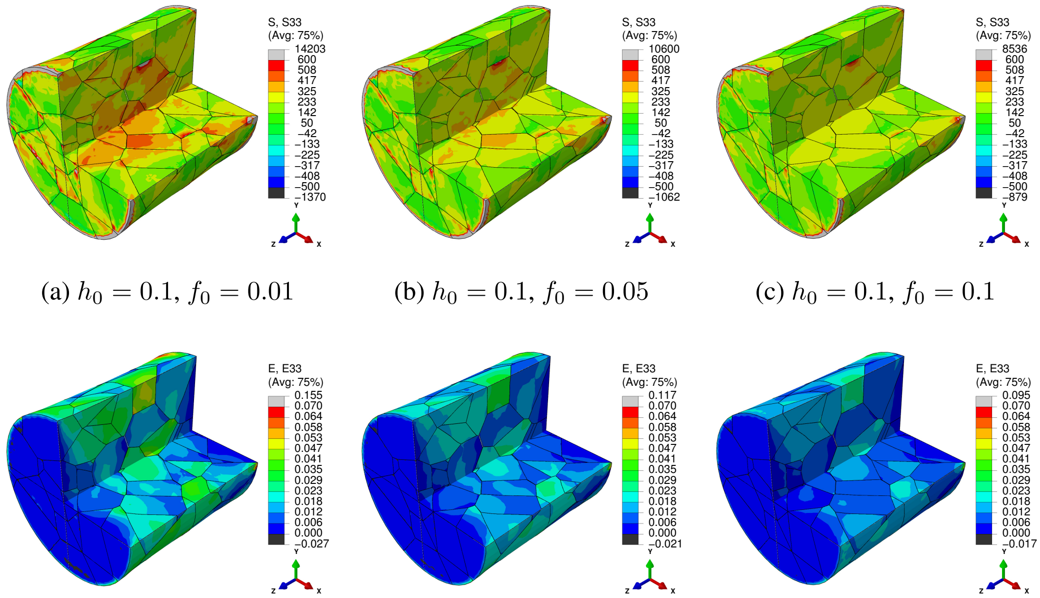

(a) $h_0 = 0.1$, $f_0 = 0.01$ (b) $h_0 = 0.1$, $f_0 = 0.05$ (c) $h_0 = 0.1$, $f_0 = 0.1$

(d) $h_0 = 0.1$, $f_0 = 0.01$ (e) $h_0 = 0.1$, $f_0 = 0.05$ (f) $h_0 = 0.1$, $f_0 = 0.1$

Figure 5.4: Contour plots for the stress (σ_{zz}) (a, b, c) and strain (ε_{zz}) (d, e, f) at the peak engineering stress increment in for different initial pore fractions, f_0 = 0.01 (a, d), f_0 = 0.05 (b, e), f_0 = 0.1 (c, f).

the specimen, which means the orientation influence of individual grains is almost negligible and the extrinsic size effect does not exist. However the influence of different orientation sets is more visible at the peak stress and in the softening region. The reason behind this difference can well be explained by the strain contour plots presented in Fig. 5.7 at 8% global strain level where a complete failure is obtained in each case. The figures show that the crack path is different for different orientation sets which is illustrated for sets 1, 4 and 5. This is an expected result since the stress concentrations at the grain boundaries are purely orientation mismatch dependent, which is distinct for different orientation distribution, inducing different traction levels at the same locations for the same specimen. The influence of the grain orientation on the micro crack formation and propagation has recently been discussed by the authors through phenomenological traction separation relations as well (see Yalcinkaya et al. [116]). It has been shown that even if the orientation set is identical, different random distribution in specimen results in similar observation where the micro specimen with the same pole figure shows different fracture characteristics.

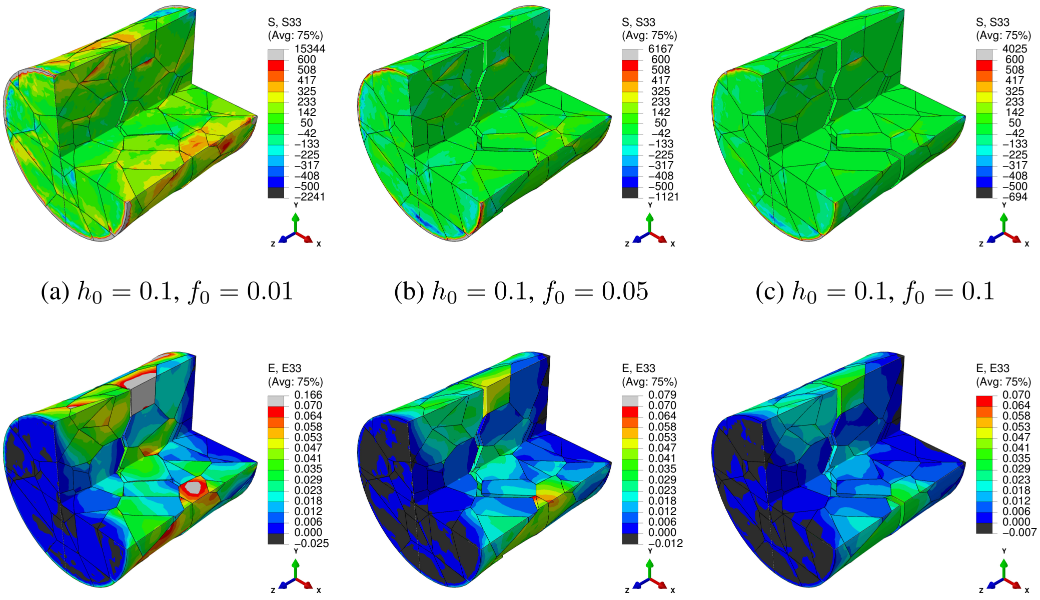

(a) $h_0 = 0.1$, $f_0 = 0.01$ (b) $h_0 = 0.1$, $f_0 = 0.05$ (c) $h_0 = 0.1$, $f_0 = 0.1$

(d) $h_0 = 0.1$, $f_0 = 0.01$ (e) $h_0 = 0.1$, $f_0 = 0.05$ (f) $h_0 = 0.1$, $f_0 = 0.1$

Figure 5.5: Contour plots for the stress (σ_{zz}) (a, b, c) and strain (ε_{zz}) (d, e, f) at 5% global strain for different initial pore fractions, f_0 = 0.01 (a, d), f_0 = 0.05 (b, e), f_0 = 0.1 (c, f).

For comparison reason, another case with 10 grains is analyzed again under same loading conditions for 5 different orientation sets and the results are presented in Fig. 5.6 (bottom). The macroscopic response shows a strong extrinsic size effect where the orientation of individual grains dominate both hardening and softening regimes in the constitutive response. Moreover the crack paths of the specimens with 10 grains are also presented in the same figure which shows a strong orientation dependence as well, which is also a valid observation for the material toughness.

The section presents a clear example on the employment of the cohesive zone model developed and implemented in the current study, for a microplasticity related fracture phenomenon that influence the service performance of certain aerospace alloys. Even though such micromechanics models are quite demanding and difficult to implement, they could give important conclusions of the microstructural parameters on the degradation procedure of crucial aerospace materials.

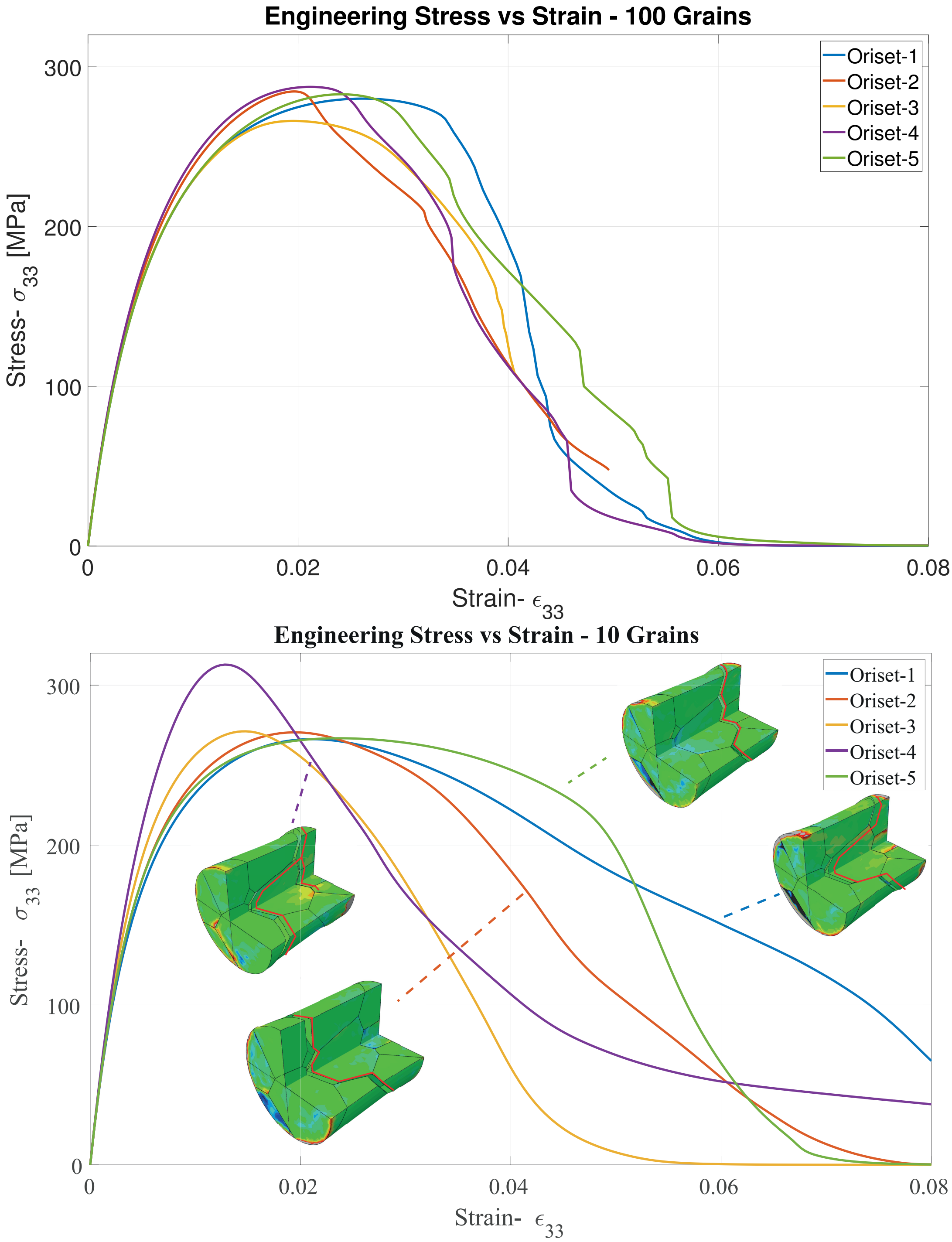

Figure 5.6: Engineering stress vs strain response of a polycrystalline cylindrical specimen with 25μm diameter and 25μm length including 100 grains (top) and 10 grains (bottom), deformed under tensile loading for different sets of randomly generated grain orientations.

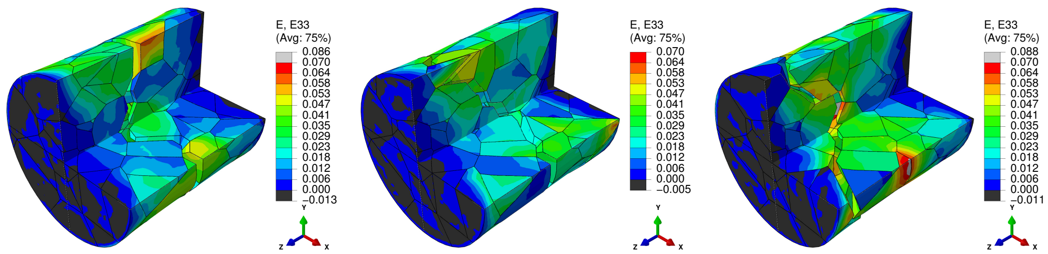

(a) Orientation set 1 (b) Orientation set 4 (c) Orientation set 5

Figure 5.7: Contour plots for the strain (ε_{zz}) at 8% global strain level for different orientation sets: set 1 (a), set 4 (b), and set 5 (c).

CHAPTER 6

CONCLUSION

In this thesis, micromechanically motivated traction-separation relations based on the growth of pores are derived to predict ductile fracture in metallic materials through cohesive zone modelling for mode-I, mode-II and mixed-mode following the initial studies in Yalçinkaya et al. [1] [2] [3]. Tractions are directly a function of pore fraction, and micromechanical parameters like pore shape and spacing govern its evolution together with separations. Due to the nature of the presented cohesive zone model, tractions cannot be expressed explicitly in mixed mode. Instead, tractions, separations, and micromechanical parameters constitute a yield function that should be satisfied in case of crack opening similar to plasticity. Hence, an elastoplastic integration scheme is developed to solve the mixed-mode tractions iteratively. While the derived traction-separation laws are originally extrinsic, an initial linear elastic region is added to make the model intrinsic for the sake of more straightforward implementation. The model is implemented with a 4-noded linear cohesive element as a UEL subroutine in Abaqus software to be used in numerical simulations. The model's capability is tested with FE models of CT and SEN specimens for different modes in the context of ductile fracture. Note that the purpose of the current work is to illustrate the influence of microstructural parameters on the ductile fracture phenomenon. Comparison of the numerical simulations with the experiments is not done yet. Still, promising results are obtained and the work can be extended in the future. The main findings of the study are listed below.

- For the mixed-mode elastoplastic integration scheme, a small elastic slope causes growth in error compared to pure-mode solutions and eventually leads to divergence.

- The model can successfully predict the expected effect of microstructural parameters such as f_0, the initial porosity, h_0 , the initial pore height, l, pore spacing and σ_y, yield stress of the matrix surrounding the pore, on the failure behavior of metallic materials. Where, h_0 is meant to be an idealized representation of pore shape effect. A smaller cavity height means that the pore shape is crack-like, and it can grow faster under mode-I loading.

- Under mixed-mode loading, crack propagation direction may change depending on the loading direction. It was shown that the present mixed-mode model of MBCZM could model the change in the crack path. When both vertical and diagonal path exists in an SEN specimen, the diagonal path is preferred for crack propagation under mixed-mode loading.

- MBCZM is used together with a strain gradient crystal plasticity model in the context of intergranular ductile fracture observed in various high strength aerospace alloys. It was observed that, in addition to strength and toughness, the crack path is affected by initial porosity in a polycrystal model with random grain orientations.

It is clear that the connections between nucleation, growth, and coalescence of microscopic voids leading to ductile failure are simplified in the proposed model. However, as simple as it may be, it can correctly represent the effects of micromechanical parameters such as pore fraction, shape, and spacing on the macroscopic properties like strength, ductility, and toughness. The traction-separation law's main variables are cohesive strength, cohesive energy, and critical separation in most of the cohesive zone models in the literature. Unlike them, tractions are derived as a function of pore fraction, and the main variables are pore related parameters which is considered to be a novel approach. Another difference is that, due to the nature of the model, mixed-mode relations are obtained in a way similar to a plasticity model. A nonlinear yield function containing tractions and micromechanical parameters is solved using an implicit numerical integration scheme.

The thesis presents an initial effort for the inclusion of micromechanical ductile fracture parameters in cohesive zone finite element constitutive relations. It presents unique results for the literature, however it requires further investigation for the extension of the framework to capture the underlaying physics in a better way.

- Cohesive strength is a function of matrix yield stress, σ_y, and initial pore fraction, f_0, and it cannot be specified separately for mode-I and mode-II. Therefore, mode-I strength is higher than mode-II strength in all logical cases, which may not be the case in reality.

- Only the growth of a pore is considered during derivation, while it is accepted that coalescence should occur after a specific porosity. This may be incorporated by acceleration pore evolution after a given porosity.

- A cylindrical void with the same height as the RVE is used for simplicity. A spherical void centered inside the RVE may be considered for a better representation of pore shape.

- Under mode-I loading traction goes to zero asymptotically, therefore a cutout separation can be specified to make traction zero after a certain separation [88], or a coalescence criteria can be introduced to accelerate pore growth.

- While it is technically challenging, an extrinsic implementation is more suitable for MBCZM since it does not have an elastic part originally. Such an implementation would allow users to simulate dynamic crack propagation and changes in crack path in a simpler way but it requires mesh manipulation and insertion of cohesive elements during the analysis.

The current implementation of the cohesive zone elements is restricted to 2D case, yet the extension to 3D is a straightforward task, which will be done in the near future. The current version is ready to be used directly in the ductile fracture predications in polycrystalline plasticity by combining with a 2D strain gradient crystal plasticity framework (see e.g. [117]). Moreover, a porous plasticity model has recently been developed considering the nucleation, growth, and coalescence of pores (see Yalcinkaya et al. [118] for a preliminary study) for the bulk plasticity response which will be used together with the MBCZM presented in this thesis in order to have physically meaningful damage initiation and propagation. Finally it is important to note that the models require validation through experimental studies and microstructural analysis for the identification of the parameters for more realistic simulations.

REFERENCES

[1] T. Yalcinkaya and A. Cocks, "Physics based formulation of a cohesive zone model for ductile fracture," in *Key engineering materials*, vol. 651, pp. 993–999, Trans Tech Publ, 2015.

[2] T. Yalçinkaya and A. Cocks, "Micromechanical cohesive zone relations for ductile fracture," *Procedia Structural Integrity*, vol. 2, pp. 1716–1723, 2016.

[3] T. Yalçinkaya, I. T. Tandogan, and A. Cocks, "Development of a micromechanics based cohesive zone model and application for ductile fracture," *Procedia Structural Integrity*, vol. 21, pp. 52–60, 2019.

[4] J. Davenport and D. Smith, "A study of superimposed fracture modes i, ii and iii on pmma," *Fatigue & Fracture of Engineering Materials & Structures*, vol. 16, no. 10, pp. 1125–1133, 1993.

[5] J. Boudet, S. Ciliberto, and V. Steinberg, "Dynamics of crack propagation in brittle materials," *Journal de Physique II*, vol. 6, no. 10, pp. 1493–1516, 1996.

[6] C. Tipper, "The fracture of metals," *Metallurgia*, vol. 39, no. 231, pp. 133–137, 1949.

[7] H. Rogers, "The tensile fracture of ductile metals," *Metal. Soc. AIME*, vol. 218, pp. 498–506, 1960.

[8] C. Beachem, "An electron fractographic study of the influence of plastic strain conditions upon ductile rupture processes in metals," *Trans. ASM*, vol. 56, no. 3, 1963.

[9] K. Puttick, "Ductile fracture in metals," *Philosophical magazine*, vol. 4, no. 44, pp. 964–969, 1959.

[10] J. Gurland and J. Plateau, "The mechanism of ductile rupture of metals containing inclusions," tech. rep., Brown Univ., Providence; Institut de Recherches de la Siderugie, St.-Germain, 1963.

[11] W. Garrison Jr and N. Moody, "Ductile fracture," *Journal of Physics and Chemistry of Solids*, vol. 48, no. 11, pp. 1035–1074, 1987.

[12] V. Tvergaard, "Material failure by void growth to coalescence," in *Advances in applied Mechanics*, vol. 27, pp. 83–151, Elsevier, 1989.

[13] A. A. Benzerga and J.-B. Leblond, "Ductile fracture by void growth to coalescence," in *Advances in applied mechanics*, vol. 44, pp. 169–305, Elsevier, 2010.

[14] A. A. Benzerga, J.-B. Leblond, A. Needleman, and V. Tvergaard, "Ductile failure modeling," *International Journal of Fracture*, vol. 201, no. 1, pp. 29–80, 2016.

[15] C. Tekoğlu, J. Hutchinson, and T. Pardoen, "On localization and void coalescence as a precursor to ductile fracture," *Philosophical Transactions of the Royal Society A: Mathematical, Physical and Engineering Sciences*, vol. 373, no. 2038, p. 20140121, 2015.

[16] M. Shakoor, V. M. T. Navas, D. P. Muñoz, M. Bernacki, and P.-O. Bouchard, "Computational methods for ductile fracture modeling at the microscale," *Archives of Computational Methods in Engineering*, vol. 26, no. 4, pp. 1153–1192, 2019.

[17] J. Wulf, T. Steinkopff, and H. Fischmeister, "Fe-simulation of crack paths in the real microstructure of an al (6061)/sic composite," *Acta materialia*, vol. 44, no. 5, pp. 1765–1779, 1996.

[18] P. McHugh and P. Connolly, "Micromechanical modelling of ductile crack growth in the binder phase of wc–co," *Computational materials science*, vol. 27, no. 4, pp. 423–436, 2003.

[19] K. Perzyński, A. Wrożyna, R. Kuziak, A. Legwand, and L. Madej, "Development and validation of multi scale failure model for dual phase steels," *Finite Elements in Analysis and Design*, vol. 124, pp. 7–21, 2017.

[20] J. Mediavilla, R. Peerlings, and M. Geers, "A robust and consistent remeshing-transfer operator for ductile fracture simulations," *Computers & structures*, vol. 84, no. 8-9, pp. 604–623, 2006.

[21] N. Moës, J. Dolbow, and T. Belytschko, “A finite element method for crack growth without remeshing,” *International journal for numerical methods in engineering*, vol. 46, no. 1, pp. 131–150, 1999.

[22] J. M. Melenk and I. Babuška, “The partition of unity finite element method: basic theory and applications,” in *Research Report/Seminar für Angewandte Mathematik*, vol. 1996, Eidgenössische Technische Hochschule, Seminar für Angewandte Mathematik, 1996.

[23] C. A. Duarte, O. Hamzeh, T. Liszka, and W. Tworzydlo, “A generalized finite element method for the simulation of three-dimensional dynamic crack propagation,” *Computer Methods in Applied Mechanics and Engineering*, vol. 190, no. 15-17, pp. 2227–2262, 2001.

[24] N. Sukumar, D. L. Chopp, N. Moës, and T. Belytschko, “Modeling holes and inclusions by level sets in the extended finite-element method,” *Computer methods in applied mechanics and engineering*, vol. 190, no. 46-47, pp. 6183–6200, 2001.

[25] P.-O. Bouchard, F. Bay, Y. Chastel, and I. Tovena, “Crack propagation modelling using an advanced remeshing technique,” *Computer methods in applied mechanics and engineering*, vol. 189, no. 3, pp. 723–742, 2000.

[26] E. Roux, M. Bernacki, and P.-O. Bouchard, “A level-set and anisotropic adaptive remeshing strategy for the modeling of void growth under large plastic strain,” *Computational Materials Science*, vol. 68, pp. 32–46, 2013.

[27] M. Shakoor, M. Bernacki, and P.-O. Bouchard, “A new body-fitted immersed volume method for the modeling of ductile fracture at the microscale: Analysis of void clusters and stress state effects on coalescence,” *Engineering Fracture Mechanics*, vol. 147, pp. 398–417, 2015.

[28] L. Kachanov, “Time of the rupture process under creep conditions, izy akad,” *Nank SSR Otd Tech Nauk*, vol. 8, pp. 26–31, 1958.

[29] J. Lemaitre and J.-L. Chaboche, “Phenomenological approach of damage rupture,” *Journal de Mecanique Appliquee*, vol. 2, no. 3, pp. 317–365, 1978.

[30] A. L. Gurson, "Continuum theory of ductile rupture by void nucleation and growth: Part i—yield criteria and flow rules for porous ductile media," *Journal of engineering materials and technology*, vol. 99, no. 1, pp. 2–15, 1977.

[31] V. Tvergaard and A. Needleman, "Analysis of the cup-cone fracture in a round tensile bar," *Acta metallurgica*, vol. 32, no. 1, pp. 157–169, 1984.

[32] G. Rousselier, "Ductile fracture models and their potential in local approach of fracture," *Nuclear engineering and design*, vol. 105, no. 1, pp. 97–111, 1987.

[33] Z. P. Bažant and M. Jirásek, "Nonlocal integral formulations of plasticity and damage: survey of progress," *Journal of engineering mechanics*, vol. 128, no. 11, pp. 1119–1149, 2002.

[34] J. Jackiewicz and M. Kuna, "Non-local regularization for fe simulation of damage in ductile materials," *Computational materials science*, vol. 28, no. 3-4, pp. 684–695, 2003.

[35] M. Samal, M. Seidenfuss, E. Roos, B. Dutta, and H. Kushwaha, "Finite element formulation of a new nonlocal damage model," *Finite Elements in Analysis and Design*, vol. 44, no. 6-7, pp. 358–371, 2008.

[36] P. Bouchard *et al.*, "An anisotropic mesh adaptation strategy for damage and failure in ductile materials," *Finite Elements in Analysis and Design*, vol. 59, pp. 1–10, 2012.

[37] R. Pourmodheji and M. Mashayekhi, "Improvement of the extended finite element method for ductile crack growth," *Materials Science and Engineering: A*, vol. 551, pp. 255–271, 2012.

[38] P. Broumand and A. Khoei, "X-fem modeling of dynamic ductile fracture problems with a nonlocal damage-viscoplasticity model," *Finite Elements in Analysis and Design*, vol. 99, pp. 49–67, 2015.

[39] T. Massart, R. Peerlings, and M. Geers, "An enhanced multi-scale approach for masonry wall computations with localization of damage," *International journal for numerical methods in engineering*, vol. 69, no. 5, pp. 1022–1059, 2007.

[40] T. Belytschko, S. Loehnert, and J.-H. Song, "Multiscale aggregating discontinuities: a method for circumventing loss of material stability," *International Journal for Numerical Methods in Engineering*, vol. 73, no. 6, pp. 869–894, 2008.

[41] S. Feld-Payet, V. Chiaruttini, J. Besson, and F. Feyel, "A new marching ridges algorithm for crack path tracking in regularized media," *International Journal of Solids and Structures*, vol. 71, pp. 57–69, 2015.

[42] G. A. Francfort and J.-J. Marigo, "Revisiting brittle fracture as an energy minimization problem," *Journal of the Mechanics and Physics of Solids*, vol. 46, no. 8, pp. 1319–1342, 1998.

[43] M. J. Borden, T. J. Hughes, C. M. Landis, A. Anvari, and I. J. Lee, "A phase-field formulation for fracture in ductile materials: Finite deformation balance law derivation, plastic degradation, and stress triaxiality effects," *Computer Methods in Applied Mechanics and Engineering*, vol. 312, pp. 130–166, 2016.

[44] M. Ambati and L. De Lorenzis, "Phase-field modeling of brittle and ductile fracture in shells with isogeometric nurbs-based solid-shell elements," *Computer Methods in Applied Mechanics and Engineering*, vol. 312, pp. 351–373, 2016.

[45] M. Ambati, R. Kruse, and L. De Lorenzis, "A phase-field model for ductile fracture at finite strains and its experimental verification," *Computational Mechanics*, vol. 57, no. 1, pp. 149–167, 2016.

[46] C. Miehe, M. Hofacker, and F. Welschinger, "A phase field model for rate-independent crack propagation: Robust algorithmic implementation based on operator splits," *Computer Methods in Applied Mechanics and Engineering*, vol. 199, no. 45-48, pp. 2765–2778, 2010.

[47] C. McAuliffe and H. Waisman, "A coupled phase field shear band model for ductile–brittle transition in notched plate impacts," *Computer Methods in Applied Mechanics and Engineering*, vol. 305, pp. 173–195, 2016.

[48] N. Moës, C. Stolz, P.-E. Bernard, and N. Chevaugeon, "A level set based model

for damage growth: the thick level set approach," *International Journal for Numerical Methods in Engineering*, vol. 86, no. 3, pp. 358–380, 2011.

[49] G. I. Barenblatt, "The formation of equilibrium cracks during brittle fracture. general ideas and hypotheses. axially-symmetric cracks," *Journal of Applied Mathematics and Mechanics*, vol. 23, no. 3, pp. 622–636, 1959.

[50] D. S. Dugdale, "Yielding of steel sheets containing slits," *Journal of the Mechanics and Physics of Solids*, vol. 8, no. 2, pp. 100–104, 1960.

[51] J. R. Rice, "Mathematical analysis in the mechanics of fracture," *Fracture: an advanced treatise*, vol. 2, pp. 191–311, 1968.

[52] A. Hillerborg, M. Modéer, and P.-E. Petersson, "Analysis of crack formation and crack growth in concrete by means of fracture mechanics and finite elements," *Cement and concrete research*, vol. 6, no. 6, pp. 773–781, 1976.

[53] J. H. Rose, J. Ferrante, and J. R. Smith, "Universal binding energy curves for metals and bimetallic interfaces," *Physical Review Letters*, vol. 47, no. 9, p. 675, 1981.

[54] J. H. Rose, J. R. Smith, and J. Ferrante, "Universal features of bonding in metals," *Physical review B*, vol. 28, no. 4, p. 1835, 1983.

[55] X.-P. Xu and A. Needleman, "Void nucleation by inclusion debonding in a crystal matrix," *Modelling and Simulation in Materials Science and Engineering*, vol. 1, no. 2, p. 111, 1993.

[56] V. Tomar, J. Zhai, and M. Zhou, "Bounds for element size in a variable stiffness cohesive finite element model," *International journal for numerical methods in engineering*, vol. 61, no. 11, pp. 1894–1920, 2004.

[57] E. Lorentz, "A mixed interface finite element for cohesive zone models," *Computer Methods in Applied Mechanics and Engineering*, vol. 198, no. 2, pp. 302–317, 2008.

[58] W. Kyeongsik, W. M. Peterson, and D. S. Cairns, "Selective activation of intrinsic cohesive elements.," *Journal of Applied Mathematics and Physics*, vol. 2, no. 12, pp. 1061–1068, 2014.

[59] G. T. Camacho and M. Ortiz, "Computational modelling of impact damage in brittle materials," *International Journal of solids and structures*, vol. 33, no. 20-22, pp. 2899–2938, 1996.

[60] N. Chandra, H. Li, C. Shet, and H. Ghonem, "Some issues in the application of cohesive zone models for metal–ceramic interfaces," *International Journal of Solids and Structures*, vol. 39, no. 10, pp. 2827–2855, 2002.

[61] A. Turon, C. G. Davila, P. P. Camanho, and J. Costa, "An engineering solution for mesh size effects in the simulation of delamination using cohesive zone models," *Engineering fracture mechanics*, vol. 74, no. 10, pp. 1665–1682, 2007.

[62] A. Turon, P. Camanho, J. Costa, and J. Renart, "Accurate simulation of delamination growth under mixed-mode loading using cohesive elements: definition of interlaminar strengths and elastic stiffness," *Composite structures*, vol. 92, no. 8, pp. 1857–1864, 2010.

[63] S. Li and S. Ghosh, "Debonding in composite microstructures with morphological variations," *International Journal of computational methods*, vol. 1, no. 01, pp. 121–149, 2004.

[64] J. Wolf, P. Longère, J.-M. Cadou, and J.-P. Crété, "Numerical modeling of strain localization in engineering ductile materials combining cohesive models and x-fem," *International Journal of Mechanics and Materials in Design*, vol. 14, no. 2, pp. 177–193, 2018.

[65] O. Nguyen, E. Repetto, M. Ortiz, and R. Radovitzky, "A cohesive model of fatigue crack growth," *International Journal of Fracture*, vol. 110, no. 4, pp. 351–369, 2001.

[66] S. del Busto, C. Betegón, and E. Martínez-Pañeda, "A cohesive zone framework for environmentally assisted fatigue," *Engineering Fracture Mechanics*, vol. 185, pp. 210–226, 2017.

[67] F. Zhou, J.-F. Molinari, and T. Shioya, "A rate-dependent cohesive model for simulating dynamic crack propagation in brittle materials," *Engineering fracture mechanics*, vol. 72, no. 9, pp. 1383–1410, 2005.

[68] N. Valoroso, G. Debruyne, and J. Laverne, "A cohesive zone model with rate-sensitivity for fast crack propagation," *Mechanics Research Communications*, vol. 58, pp. 82–87, 2014.

[69] A. Banerjee and R. Manivasagam, "Triaxiality dependent cohesive zone model," *Engineering Fracture Mechanics*, vol. 76, no. 12, pp. 1761–1770, 2009.

[70] S. Chanda and C. Ru, "Cohesive zone model for temperature dependent fracture analysis of pipeline steel," in *Proceedings of 25th Canadian congress on applied mechanics*, pp. 1–4, 2015.

[71] I. Özdemir, W. Brekelmans, and M. Geers, "A thermo-mechanical cohesive zone model," *Computational Mechanics*, vol. 46, no. 5, pp. 735–745, 2010.

[72] A. Needleman, "A continuum model for void nucleation by inclusion debonding," 1987.

[73] A. Needleman, "An analysis of tensile decohesion along an interface," *Journal of the Mechanics and Physics of Solids*, vol. 38, no. 3, pp. 289–324, 1990.

[74] G. Beltz and J. Rice, "Dislocation nucleation versus cleavage decohesion at crack tips," *Modeling the deformation of Crystalline Solids*, pp. 457–480, 1991.

[75] G. Beltz and J. Rice, "Dislocation nucleation at metal-ceramic interfaces," *Acta metallurgica et materialia*, vol. 40, pp. S321–S331, 1992.

[76] V. Tvergaard, "Effect of fibre debonding in a whisker-reinforced metal," *Materials science and engineering: A*, vol. 125, no. 2, pp. 203–213, 1990.

[77] V. Tvergaard and J. W. Hutchinson, "The influence of plasticity on mixed mode interface toughness," *Journal of the Mechanics and Physics of Solids*, vol. 41, no. 6, pp. 1119–1135, 1993.

[78] K. Park and G. H. Paulino, "Cohesive zone models: a critical review of traction-separation relationships across fracture surfaces," *Applied Mechanics Reviews*, vol. 64, no. 6, p. 060802, 2011.

[79] M. Van den Bosch, P. Schreurs, and M. Geers, "An improved description of the exponential xu and needleman cohesive zone law for mixed-mode decohesion," *Engineering Fracture Mechanics*, vol. 73, no. 9, pp. 1220–1234, 2006.

[80] F. Zhou, J.-F. Molinari, and K. Ramesh, "A cohesive model based fragmentation analysis: effects of strain rate and initial defects distribution," *International Journal of Solids and Structures*, vol. 42, no. 18-19, pp. 5181–5207, 2005.

[81] Z. Zhang, G. H. Paulino, and W. Celes, "Extrinsic cohesive modelling of dynamic fracture and microbranching instability in brittle materials," *International Journal for Numerical Methods in Engineering*, vol. 72, no. 8, pp. 893–923, 2007.

[82] K. Park, G. H. Paulino, and J. R. Roesler, "A unified potential-based cohesive model of mixed-mode fracture," *Journal of the Mechanics and Physics of Solids*, vol. 57, no. 6, pp. 891–908, 2009.

[83] P. B. Woelke, M. Shields, and J. Hutchinson, "Cohesive zone modeling and calibration for mode i tearing of large ductile plates," *Engineering Fracture Mechanics*, vol. 147, pp. 293–305, 2015.

[84] C. Chen, O. Kolednik, I. Scheider, T. Siegmund, A. Tatschl, and F. Fischer, "On the determination of the cohesive zone parameters for the modeling of microductile crack growth in thick specimens," *International journal of fracture*, vol. 120, no. 3, pp. 517–536, 2003.

[85] Y. Xu, X. Li, X. Wang, and L. Liang, "Inverse parameter identification of cohesive zone model for simulating mixed-mode crack propagation," *International Journal of Solids and Structures*, vol. 51, no. 13, pp. 2400–2410, 2014.

[86] I. Scheider and W. Brocks, "The effect of the traction separation law on the results of cohesive zone crack propagation analyses," in *Key Engineering Materials*, vol. 251, pp. 313–318, Trans Tech Publ, 2003.

[87] H. Li and N. Chandra, "Analysis of crack growth and crack-tip plasticity in ductile materials using cohesive zone models," *International Journal of Plasticity*, vol. 19, no. 6, pp. 849–882, 2003.

[88] V. Tvergaard and J. W. Hutchinson, "The relation between crack growth resistance and fracture process parameters in elastic-plastic solids," *Journal of the Mechanics and Physics of Solids*, vol. 40, no. 6, pp. 1377–1397, 1992.

[89] I. Scheider, "Micromechanical based derivation of traction-separation laws for cohesive model simulations," *Procedia Engineering*, vol. 1, no. 1, pp. 17–21, 2009.

[90] R. Andersen, C. Felter, and K. Nielsen, "Micro-mechanics based cohesive zone modeling of full scale ductile plate tearing: From initiation to steady-state," *International Journal of Solids and Structures*, vol. 160, pp. 265–275, 2019.

[91] R. Andersen, C. Tekoğlu, and K. Nielsen, "Cohesive traction–separation relations for tearing of ductile plates with randomly distributed void nucleation sites," *International Journal of Fracture*, vol. 224, no. 2, pp. 187–198, 2020.

[92] S. Firooz, S. Saeb, G. Chatzigeorgiou, F. Meraghni, P. Steinmann, and A. Javili, "Systematic study of homogenization and the utility of circular simplified representative volume element," *Mathematics and Mechanics of Solids*, vol. 24, no. 9, pp. 2961–2985, 2019.

[93] G. H. Hardy, J. E. Littlewood, and P. George, *Inequalities. By G.H. Hardy, J.E. Littlewood, and G. Polya*. Cambridge University Press, 1978.

[94] N. A. Fleck and J. W. Hutchinson, "Void growth in shear," *Proceedings of the Royal Society of London. A. Mathematical and Physical Sciences*, vol. 407, no. 1833, pp. 435–458, 1986.

[95] K. Park and G. H. Paulino, "Computational implementation of the ppr potential-based cohesive model in abaqus: Educational perspective," *Engineering fracture mechanics*, vol. 93, pp. 239–262, 2012.

[96] W. Brocks, A. Cornec, and I. Scheider, "Computational aspects of nonlinear fracture mechanics," *GKSS FORSCHUNGSZENTRUM GEESTHACHT GMBH-PUBLICATIONS-GKSS*, no. 30, 2003.

[97] A. Benallal, R. Billardon, and I. Doghri, "An integration algorithm and the corresponding consistent tangent operator for fully coupled elastoplastic and

damage equations," *Communications in Applied Numerical Methods*, vol. 4, no. 6, pp. 731–740, 1988.

[98] T. Yalcinkaya, W. Brekelmans, and M. Geers, "Non-convex rate dependent strain gradient crystal plasticity and deformation patterning," *International Journal of Solids and Structures*, vol. 49, no. 18, pp. 2625–2636, 2012.

[99] B. Klusemann and T. Yalçinkaya, "Plastic deformation induced microstructure evolution through gradient enhanced crystal plasticity based on a non-convex helmholtz energy," *International Journal of Plasticity*, vol. 48, pp. 168–188, 2013.

[100] B. Klusemann, T. Yalçinkaya, M. G. Geers, and B. Svendsen, "Application of non-convex rate dependent gradient plasticity to the modeling and simulation of inelastic microstructure development and inhomogeneous material behavior," *Computational Materials Science*, vol. 80, pp. 51–60, 2013.

[101] T. Yalçinkaya, I. Tandoğan, and I. Ozdemir, "Void growth based inter-granular ductile fracture in strain gradient polycrystalline plasticity." Manuscript submitted for publication., 2020.

[102] ASTM: E 1820-01, "Standard test method for determining measurement of fracture toughness," standard, 2003.

[103] J. Rice and G. F. Rosengren, "Plane strain deformation near a crack tip in a power-law hardening material," *Journal of the Mechanics and Physics of Solids*, vol. 16, no. 1, pp. 1–12, 1968.

[104] J. Krafft, A. Sullivan, and R. Boyle, "Effect of dimensions on fast fracture instability of notched sheets," in *Proceedings of the crack propagation symposium*, vol. 1, pp. 8–26, College of Aeronautics Cranfield, England, 1961.

[105] R. Ritchie, "Mechanisms of fatigue crack propagation in metals, ceramics and composites: role of crack tip shielding," *Materials Science and Engineering: A*, vol. 103, no. 1, pp. 15–28, 1988.

[106] R. O. Ritchie, "Mechanisms of fatigue-crack propagation in ductile and brittle solids," *International journal of Fracture*, vol. 100, no. 1, pp. 55–83, 1999.

[107] Engineering ToolBox, (2004), "Friction and friction coefficients. [online] available at: https://www.engineeringtoolbox.com/friction-coefficients-d778.html," [accessed 19.09.2020].

[108] C. Tekoglu, "Representative volume element calculations under constant stress triaxiality, lode parameter, and shear ratio," *International Journal of Solids and Structures*, vol. 51, no. 25-26, pp. 4544–4553, 2014.

[109] M. A. Sutton, M. L. Boone, F. Ma, and J. D. Helm, "A combined modeling–experimental study of the crack opening displacement fracture criterion for characterization of stable crack growth under mixed mode i/ii loading in thin sheet materials," *Engineering Fracture Mechanics*, vol. 66, no. 2, pp. 171–185, 2000.

[110] T. Yalçinkaya, İ. Özdemir, A. O. Firat, and İ. T. Tandoğan, "Micromechanical modeling of inter-granular localization, damage and fracture," *Procedia Structural Integrity*, vol. 13, pp. 385–390, 2018.

[111] T. Yalcinkaya, W. Brekelmans, and M. Geers, "Deformation patterning driven by rate dependent non-convex strain gradient plasticity," *Journal of the Mechanics and Physics of Solids*, vol. 59, no. 1, pp. 1–17, 2011.

[112] D. Dumont, A. Deschamps, and Y. Brechet, "On the relationship between microstructure, strength and toughness in aa7050 aluminum alloy," *Materials Science and Engineering: A*, vol. 356, no. 1-2, pp. 326–336, 2003.

[113] P. Unwin, G. Lorimer, and R. Nicholson, "The origin of the grain boundary precipitate free zone," *Acta Metallurgica*, vol. 17, no. 11, pp. 1363–1377, 1969.

[114] T. Pardoen, D. Dumont, A. Deschamps, and Y. Brechet, "Grain boundary versus transgranular ductile failure," *Journal of the Mechanics and Physics of Solids*, vol. 51, no. 4, pp. 637–665, 2003.

[115] A. Cerrone, P. Wawrzynek, A. Nonn, G. H. Paulino, and A. Ingraffea, "Implementation and verification of the park–paulino–roesler cohesive zone model in 3d," *Engineering Fracture Mechanics*, vol. 120, pp. 26–42, 2014.

[116] T. Yalçinkaya, İ. Özdemir, and A. Firat, "Inter-granular cracking through strain gradient crystal plasticity and cohesive zone modeling approaches," *Theoretical and Applied Fracture Mechanics*, vol. 103, p. 102306, 2019.

[117] T. Yalçinkaya, İ. Özdemir, and I. Simonovski, "Micromechanical modeling of intrinsic and specimen size effects in microforming," *International Journal of Material Forming*, vol. 11, no. 5, pp. 729–741, 2018.

[118] T. Yalçinkaya, C. Erdoğan, I. T. Tandoğan, and A. Cocks, "Formulation and implementation of a new porous plasticity model," *Procedia Structural Integrity*, vol. 21, pp. 46–51, 2019.